



TECHNISCHE  
UNIVERSITÄT  
WIEN  
Vienna University of Technology

## **Master Thesis**

Subsurface Backscatter Effects over Croatia

For the purpose of obtaining the academic degree

## **Master of Science**

Under direction of

Professor Dr. Wolfgang Wagner

and

Senior Scientist Dr.techn. MSc Mariette Vreugdenhil

Submitted to the Technical University of Vienna

**Faculty for Mathematics and Geoinformation**

from

**Julia Geiger**

01227829

Am Hutfeld 11

A – 2620 Neunkirchen

# Table of Contents

1. INTRODUCTION .....	3
2. THEORY .....	4
2.1. BACKSCATTER BEHAVIOR OF SOIL .....	7
3. STUDY AREA - CROATIA .....	8
4. DATA .....	10
4.1. 1 KM SURFACE SOIL MOISTURE FROM SENTINEL-1 C-SAR .....	10
4.2. SOIL MOISTURE AND PRECIPITATION DATA FROM THE GLOBAL LAND DATA ASSIMILATION SYSTEM .....	13
4.3. ESA CLIMATE CHANGE INITIATIVE LANDCOVER (CCI – LC) DATASET .....	14
4.3.1. DESCRIPTION OF SIMPLIFIED CCI-LC CLASSES .....	15
4.4. SOIL GRIDS DATASET .....	17
4.5. THE INTERNATIONAL HYDROGEOLOGICAL MAP OF EUROPE .....	20
5. METHODS .....	21
5.1. TEMPORAL ANALYSIS .....	22
5.2. SPATIAL ANALYSIS .....	24
5.3. RELATING SUBSURFACE SCATTERING TO PHYSICAL PROCESSES .....	25
6. RESULTS .....	26
6.1. TEMPORAL ANALYSIS .....	26
6.2. SPATIAL ANALYSIS .....	30
6.2.1. COMPARISON WITH GOOGLE SATELLITE IMAGES .....	33
6.2.2. COMPARISON WITH ESA CCI-LC DATASET .....	35
6.2.3. COMPARISON WITH SOIL GRIDS DATASET .....	38
6.2.4. COMPARISON WITH LITHOLOGY DATASET .....	41
7. DISCUSSION .....	44
7.1. TEMPORAL ANALYSIS .....	44
7.2. SPATIAL ANALYSIS .....	44
8. CONCLUSION – OUTLOOK .....	50
9. BIBLIOGRAPHY .....	51
10. LIST OF FIGURES .....	53
11. LIST OF TABLES .....	56
12. APPENDIX .....	57

## 1. Introduction

The world is changing as a cause of our extensive, relentless, merciless use of its nonrenewable resources. Average global temperatures are rising, climate patterns and trends are changing and the effects are seen everywhere. Remote Sensing has revolutionized the way we perceive our Planet Earth. Through the use of electromagnetic waves in frequencies other than that of visible light to perceive Earth's surface, we are now able to investigate aspects of our planet in temporal and spatial extents that could never have been possible with in situ measurements only. Today, microwave remote sensing data from space is being used to investigate long term changes in climate, changing factors such as vegetation dynamics, ice and snow cover, atmospheric properties and soil moisture. For example, Cleland et al investigated the shifting plant phenology over Eurasia with the help of the satellite MODIS sensor (Cleland et al, 2007). Plants are finely tuned to their environment so changes in phenology are a strong indicator for climate change. On the other hand, Bishop et al describes the use of thermal (LIDAR) and microwave (SAR/InSAR) remote sensing to assist in glacier analysis within the GLIMIS project (Bishop et al, 2004). The remote sensing studies within this project provide vital baseline information on glaciers changes to improve our understanding of the complex interconnection between glacier and climate changes. And Seneviratne et al explored the manifold impact of soil moisture on climate and their relevance for climate change projection using data from both microwave remote sensing sensors and GRACE missions (Sonia I. Seneviratne et al, 2010). Through Seneviratne et al investigation into the detailed study of soil moisture as an indicator for climate change I was led to a map from the European Environment Agency depicted in Figure 1. The entire county of Croatia has experienced a strong negative soil moisture trend in the summer months over the last 60 years, loosing between 2,5 and 8 liters/m<sup>3</sup>/10 years.

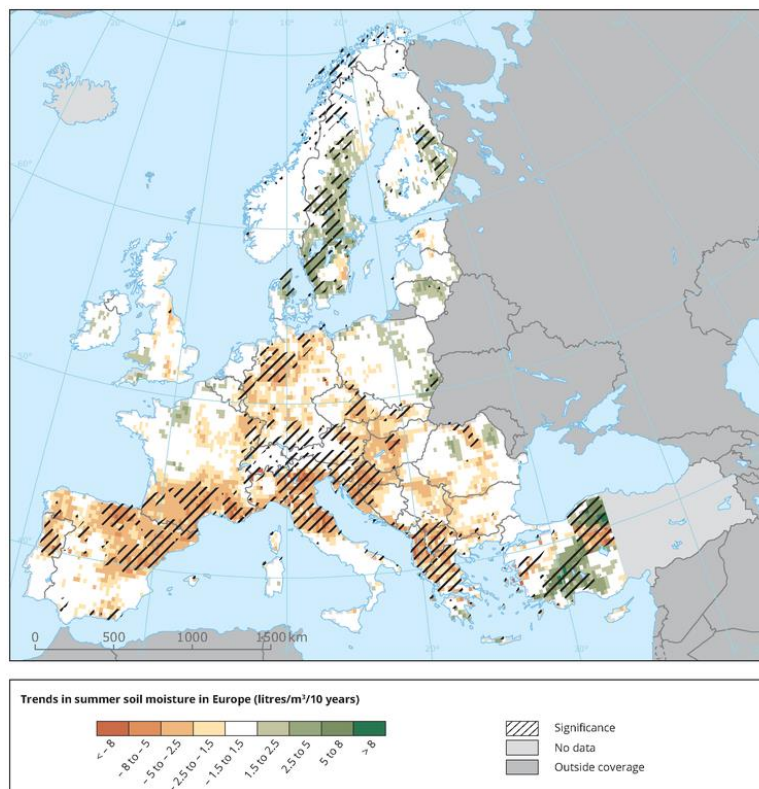


Figure 1: Trends in summer (June to August) soil moisture in Europe between 1951 – 2012. The soil moisture content was modelled using a soil moisture balance model in the upper soil horizons (EEA, 2017).

Model data agrees with this trend map of Europe; however, when perceiving microwave remotely sensed backscatter soil moisture information this extremely dry soil is not witnessed. In the summer months the soil moisture information collected through C-band backscatter data from Metop ASCAT is seen to be much higher than the soil moisture model data which is considered to be the absolute truth. One hypothesis is that this high backscatter during times of extreme low soil moisture can be explained by volume scattering phenomena within the dry soil layer and subsequently backscattering by subsurface discontinuities (Mätzler, 1998 & Wagner et al, 2013). Furthermore, there must be a threshold soil moisture value after which the usual positive correlation between backscatter and soil moisture takes place. When soil moisture drops below this threshold value backscatter will tend to increase as the soil will act as a volume scatterer and subsurface lithological layers will act as the reflecting surface.

The objective of this research is to characterize subsurface scattering effects in C-band backscatter data over Croatia at high resolution using Sentinel-1. After providing a theoretical background on subsurface scattering, this research will address two research questions. 1) What are the spatial and temporal characteristics of subsurface scattering? 2) Which physical processes are driving subsurface scattering in Croatia?

## 2. Theory

Microwave remote sensing is the acquisition of information about the nature and properties of distant objects with electromagnetic waves with a wavelength between 1mm and 1m (frequency range from 0.3 to 300 GHz) in a non-invasive manner. Electromagnetic waves at this wavelength have the important capability to permeate relatively lossless through the atmosphere and partially also clouds and rain. Additionally, microwave remote sensing can be used as an active sensor system which means that it does not need the sun as a source of illumination. Consequently, this data acquisition can collect data successfully regardless of weather, cloud cover and time of day. Active microwave sensors, like the sensors used on the Sentinel – 1 satellite constellation, are also known as radars as they transmit an electromagnetic wave and record the returned signal scattered back from the target surface. The key to microwave remote sensing lies in the ability to correctly interpret this returned backscatter signal, the measured quantity, and translate these into the desired natural parameters. Reference data and a priori knowledge on the target and its surroundings is needed for a correct inversion, and subsequently for a correct investigation.

To be able to turn the measured backscattered radiation signal into target properties such as surface soil moisture, the physical and mathematical properties of electromagnetic waves must be exploited. Because the interaction of electromagnetic waves with materials are being investigated, it is necessary to describe and quantify their electromagnetic properties – properties that are vital for not only understanding but also interpreting the measurements made in microwave remote sensing acquisition.

Electromagnetic properties of any material are characterized with the electric permittivity, magnetic permeability and electric conductivity; however, only this first will be needed in the scope of microwave remote sensing. Generally, electric permittivity ( $\epsilon$ ) is defined as the ratio of the flux density produced by an electric field in a given dielectric to the flux density produced by that field in a vacuum.

Through experiment, the permittivity of free space ( $\epsilon_0$ ) is found to be  $8.8542 \times 10^{-12} \text{C}^2\text{N}^{-1}\text{m}^{-2}$ . The permittivity of a material medium is related to  $\epsilon_0$  through the definition of relative permittivity ( $\epsilon_r$ ), a dimensionless quantity given by:

$$\epsilon_r = \frac{\epsilon}{\epsilon_0}$$

*Equation 1: Relative permittivity of a material medium (Woodhouse, 2006)*

This term, along with all other electromagnetic terms, are complex numbers; however, within the scope of microwave remote sensing, the most restrictive description of matter, namely lossless, homogeneous, isotropic linear materials is used. Therefore, it is assumed that electric permittivity are real, constant numbers throughout the material (Woodhouse, 2006). Most materials encountered in remote sensing are non-conducting. These materials are known as dielectric. The term “dielectric constant”, which is used to describe these materials, can be used interchangeably with this real part of the electric permittivity. An electromagnetic wave will attenuate exponentially as it travels through a dielectric medium, meaning the electromagnetic waves amplitude will decay exponentially as it propagates through the medium. In this case the imaginary part of the complex relative permittivity must be introduced:

$$\epsilon^r = \epsilon_r' - i\epsilon_r''$$

*Equation 2: Complex relative permittivity composed of the real part, the lossless dielectric constant, and imaginary part, which describes the attenuation of energy through the medium (Woodhouse, 2006)*

Furthermore, the penetration depth ( $\delta_p$ ) of an electromagnetic wave through attenuating medium can be described. The distance at which the electromagnetic waves power is reduced by a factor  $e$  depends on how strongly the medium attenuates the impinging wave. The penetration depth is related to the relative permittivity through:

$$\delta_p \approx \frac{\lambda \sqrt{\epsilon_r'}}{2\pi \epsilon_r''}$$

*Equation 3: penetration depth of an electromagnetic wave depends on its wavelength, which is also reduced in a dielectric medium, and both the real and imaginary part of the complex relative permittivity of the attenuating medium (Woodhouse, 2006)*

The presence of water dramatically reduces a mediums penetration depth as a result of its high dielectric constant from its oriental polarization feature. Generally, the penetration depth of microwaves, for example at C-band, is only about 2mm into pure water surfaces. The salinity of water, ocean water, reduces this depth even further (Woodhouse, 2006). The volume of water contained in soil, the medium of interest during this investigation, therefore defines the soils dielectric constant and determines the microwaves penetration depth.

The term soil refers to the end product of the combined influence of climate, topography, organisms such as flora, fauna and human, on parent materials, the soils original rocks and minerals (FAO). Soil is a composite of lose grains, air and water. Water in the soil can either be free or bound. Bound water molecules are absorbed by the surface of the soil particles and are therefore not free to rotate under excitation. Bound water causes the dielectric constant to increase slowly. When soil is completely saturated, the dielectric constant approaches that of liquid water. Hereafter, the imaginary part of the complex relative permittivity also increases with increasing moisture fraction; however, at a slower

rate. The proportion of free water to bound water in soil depends on properties such as surface area of the soil. Across wavelengths of the microwave region, we can expect the dielectric constant to have values of 1 for air, ~4 for soil and ~80 for water; therefore, it is clear that the liquid water content has the largest influence (Woodhouse, 2006). Additionally, signal penetration depth decreases as the soil moisture increases.

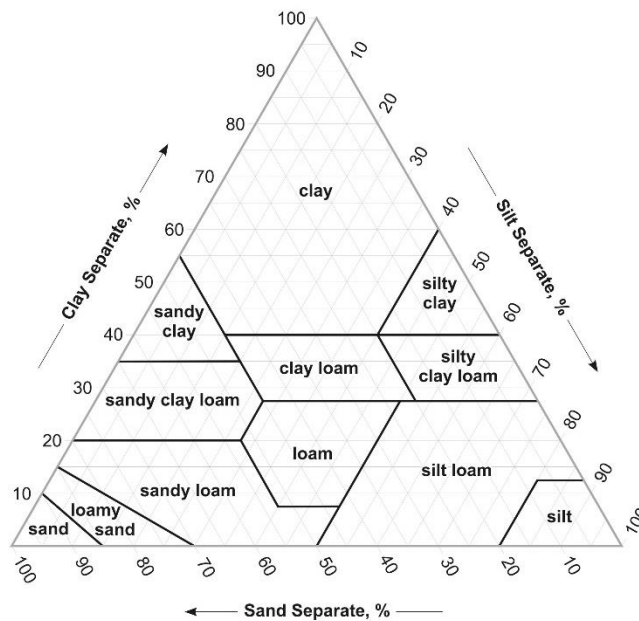


Figure 2: Soil Texture Triangle ([www.nrcs.usda.gov](http://www.nrcs.usda.gov))

Surface area of soil depends on the amount, shape and size of the soil particles. These characteristics are defined by the soil texture, which refers to the size range of grains in the soil. Figure 2 shows the soil texture array through which soils are defined. Through this array, a soil is placed into a class according to its weight percentage of sand, silt and clay. Table 1 shows the defining grain sizes according to the USDA as well as a depiction of possible grain size distribution. Through this grain size distribution, it becomes clear that the pore space between the grains similarly grow or shrink in accordance to the size of the grains.

Soil Type	Grain Size ( $\mu\text{m}$ )
Sand	50 – 2000
Silt	2 – 50
Clay	< 2

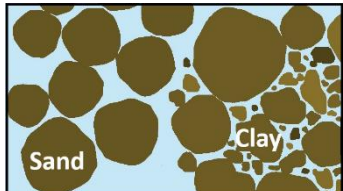


Table 1: Grain sizes for each soil texture, defined by the USDA

Sand has the largest grain size; therefore, also the largest pore size. These large pores can hold a large volume of free water; however, this water also percolates quickest through the soil. Saturated sand has a high dielectric constant for a relatively short period of time. Through the quick percolation of the free water, soil with a high sand content also dry quickly. Clay soils, on the other hand, have a much smaller grain size; therefore, also much smaller pores. Because of these small pores, water is bound much more strongly and can only percolate slowly. Through this slow percolation, puddles quickly form and cover the surface acting as a water body, drastically reducing the penetration depth and falsifying electromagnetic backscatter measurements.

When soil temperature drops below 0°C, water freezes. As each water molecule becomes cemented in its current position, oriental-polarization is no longer possible and the dielectric constant decreases abruptly. In this case, frozen soil has the same dielectric characteristics as dry soil (see Figure 3).

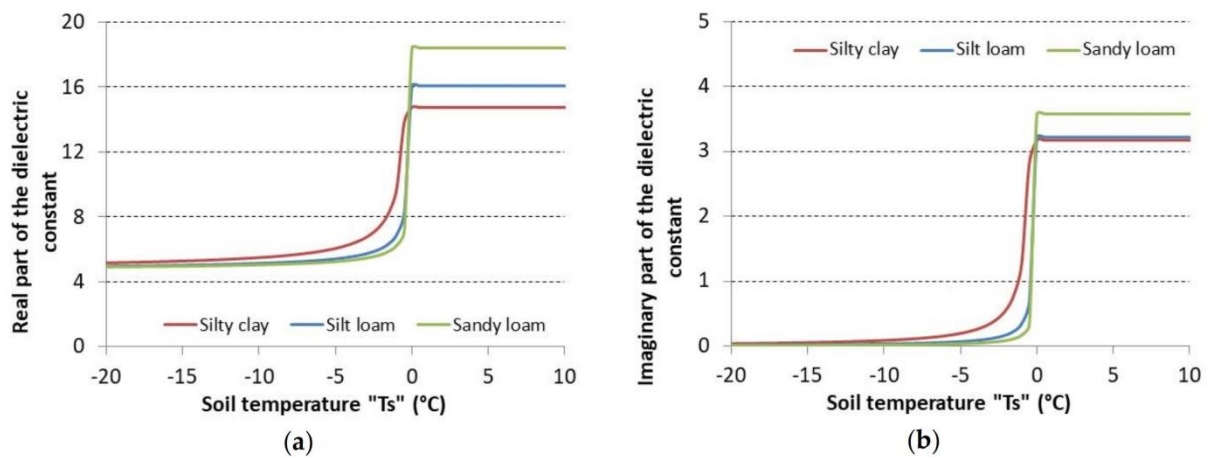


Figure 3: The real (a) and imaginary (b) part of the dielectric constant of a frozen soil-water mixture with 30% vol soil moisture content according to the soil temperature for three soil types (N.Baghdadi, 2018)

Altogether, the textural composition of the soil determines the specific surface area of the soil particles which defines soil moisture and subsequently decides penetration depth values of the soil.

### 2.1. Backscatter behavior of soil

In general, a vegetation canopy forms a heterogeneous volume with structural components of varying sizes and densities. The scattering elements are leaves, branches and trunks with diverse shapes and a large range of diameters. However, the volume scattering phenomena isn't bound to a vegetation layer in nature. In this investigation, high Sentinel-1 soil moisture backscatter values in dry summer months in Croatia are also explained with the soil layer turning from a surface scatterer into a volume scatterer due to extreme dryness and the subsurface matter turning into the surface scatterer from which the microwaves reflect.

Natural media such as the vegetation layer or a layer of extremely dry soil is inhomogeneous and gives rise to volume scattering. While the scattering strength of a surface scatterer is proportional to the difference in the complex dielectric constants above and below the surface, the scattering strength of a volume scatterer is proportional to the dielectric discontinuities inside the medium and the density of the embedded inhomogeneities. Similarly, as the angular pattern of a surface scatterer is determined by the surface roughness, the angular pattern of a volume scatterer is defined by the average dielectric constant of the medium and the geometric size of the inhomogeneities relative to the wavelength of the incident microwave radiation (Woodhouse, 2018); Furthermore, there must exist as soil moisture threshold value where a soil layer turns from a surface scatterer to a volume scatterer. This will not be covered during this investigation.

Emission by a dry soil layer is more complex than that of saturated soil. Contributions to the emission of this surface consists of subsurface-emitted radiation as well as soil-emitted radiation. The received radiation is expressed as a sum of the volume-, surface-, and volume-surface-contribution as illustrated in Figure 4, the so-called Cloud-Model adapted to dry soil.

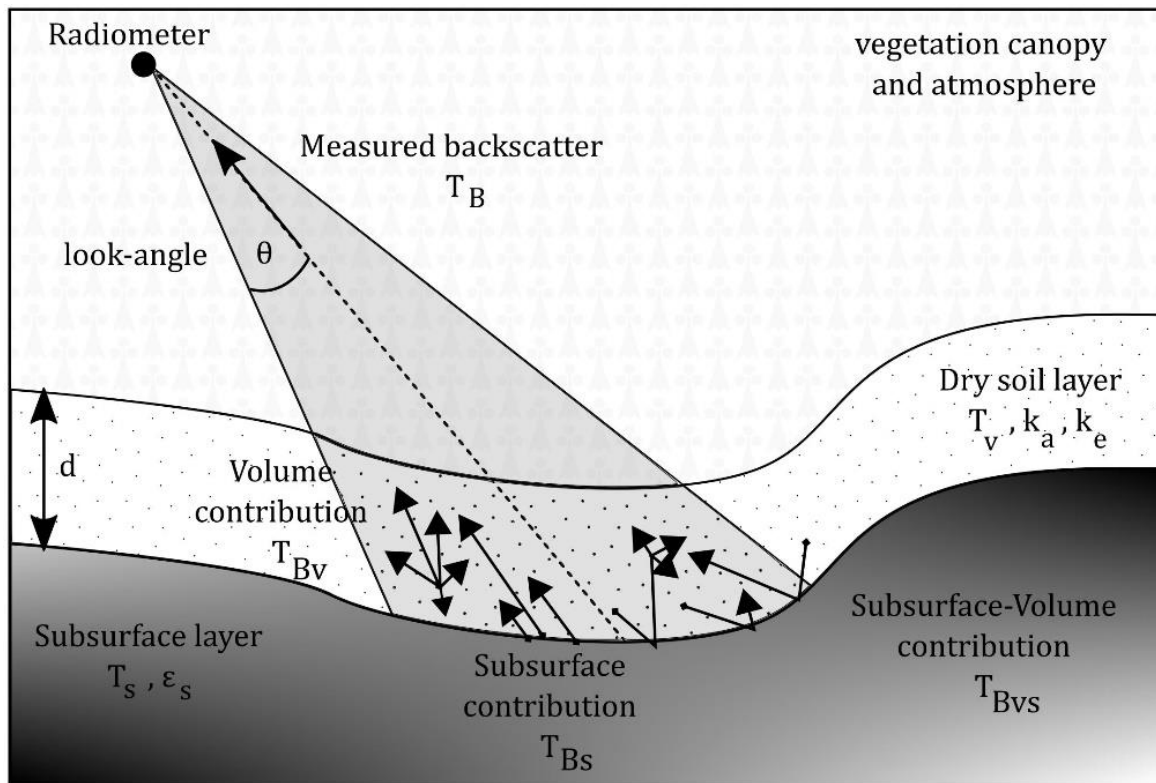


Figure 4: The Cloud-Model shown through a SAR radiation surface and volume scattering through a dry soil layer

Analogously, Equation 4 formulates the total backscatter coefficient as the sum of the volume-, surface-, and volume-surface and surface-volume interaction contributions. These interaction contributions include all multiple scattering effects that occur within the dry soil layer.

$$\sigma_{dry\ soil}^0 = \sigma_{volume}^0 + \sigma_{surface}^0 + \sigma_{interaction}^0$$

Equation 4: Total backscattering coefficient of volume scatterer [ $m^2/m^2$ ]

This Cloud-Model adaptation simplifies the volumetric backscattering behavior from a dry soil surface as it treats this layer as a homogeneous medium (air) with identical scatterers fixed randomly with a uniform distribution (water droplets) throughout the volume.

The term subsurface refers to layers of material with different physical properties to the adjoining layers above. In this investigation a subsurface layer with a higher dielectric constant could be the reason for high backscatter signals, or a general change in scattering mechanism, at times when the surface soil layer experiences extreme dryness, increasing signal penetration depth. This subsurface layer could be the bedrock or underlying lithology with a large grain size, larger rocks, or even a higher base saturation.

### 3. Study area - Croatia

The Republic of Croatia is a country in central-southeast Europe on the Adriatic Sea, sharing a maritime border with Italy. It lies mostly between 42°-47° latitude and 13°-20° longitude. Croatia has an area of 56,594 km<sup>2</sup> including over one thousand islands and islets and 128 km<sup>2</sup> of water. As seen in Figure 5, there are four biogeographical regions in Croatia. Mediterranean along Croatia's coast, alpine in the mountainous regions, pannonian along major rivers such as the Danube and the Drave in the north east and continental.



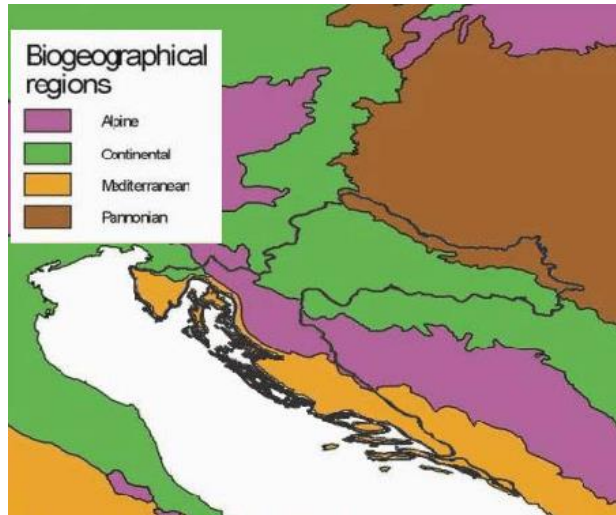
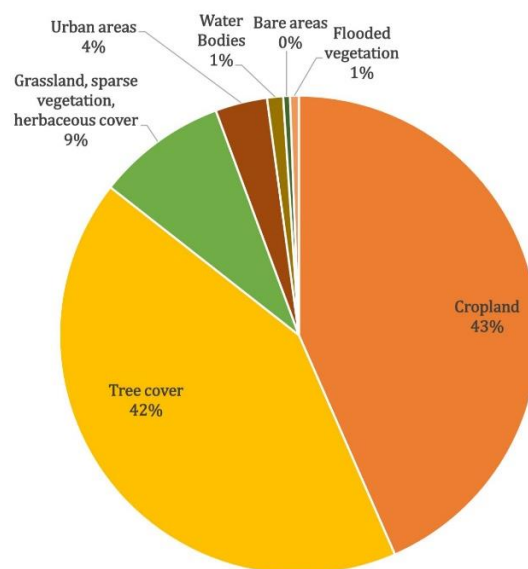


Figure 5: Biogeographical regions of Croatia (Lovrić, 2013)

Over the Mediterranean biogeographical region of Croatia, the climate can be classified as Csa (Mediterranean hot summer) climate according to the Köppen-Geiger classification. The Csa climate class refers to climates that usually occur on the western side of continents between latitudes of 30° and 45°. In the winter, these climates have moderate temperatures and changeable, rainy weather. In the summer, the climate is hot and dry due to the domination of subtropical high-pressure systems. An exception here is in the immediate coastal areas, where summers are milder due to the nearby presence of cold ocean currents that may bring fog but prevent rain (McKnight, 2000).

The Alpine biogeographical band across Croatia is marked with a harsh Csa climate and rugged terrain and separates the Csa climate along the coast and Cfa climate in the north and northeast of Croatia. Unlike Csa climates, Cfa (humid subtropical) climates have a warm and wet flow that creates warm and moist conditions in the summer months. Croatia retains two different climate zones with contrasting summer/winter precipitation volumes making it perfect for a spatial and temporal soil moisture investigation.



**The distribution of landcover in Croatia**

Figure 6: simplified ESA Climate Change Initiative Landcover distribution in Croatia

As seen in Figure 6, the main landcover types of Croatia are Cropland, Tree cover and Grassland. Figure 6 shows that only 6% of the land in Croatia is not usable for the following soil moisture investigation as they hold either no soil, urban and bar areas, or they are completely saturated, water bodies and flooded vegetation.

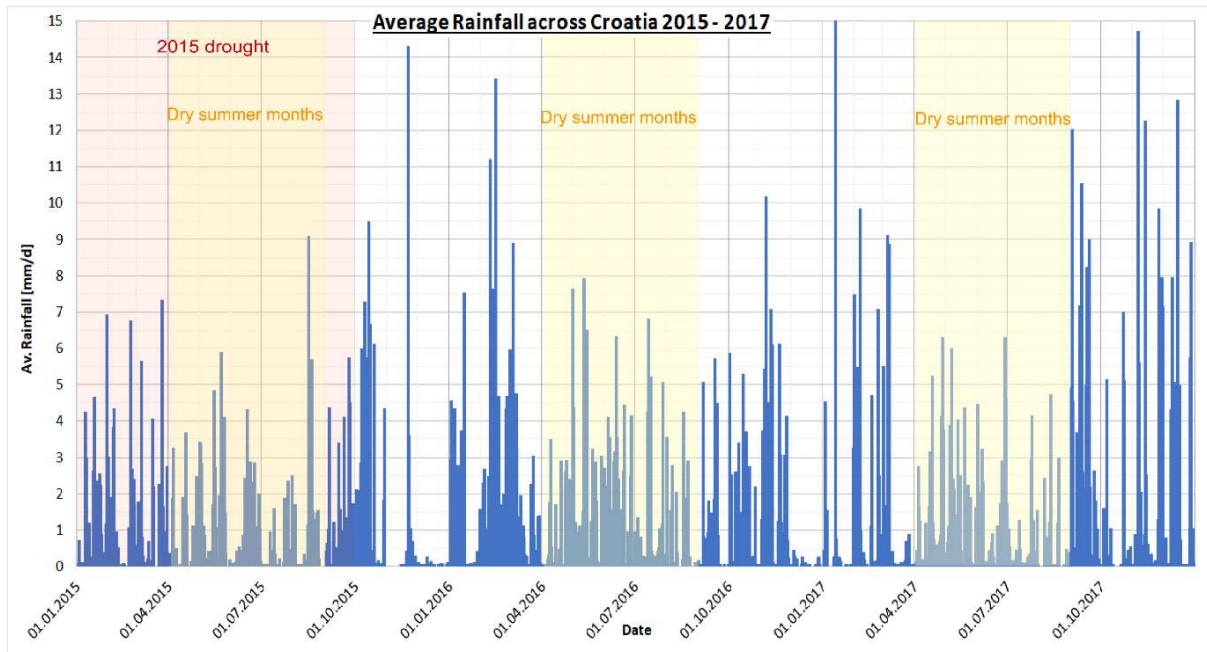


Figure 7: GLDAS model average rainfall over all of Croatia from 01.01.2015 to 31.12.2017. Summer months, from June to October are highlighted with a yellow background.

An insight into the average rainfall across the whole of Croatia is shown in Figure 7. Annual wet and dry periods can be seen – the driest time being during the summer months, between June and October. Through Figure 7 it also becomes clear that 2015 was an exceptionally dry year in Croatia. According to Copernicus’ Global Drought Observatory, 2015 was a year of drought not only in Croatia but also across Europe, see appendix Figure 46 (EDO Drought News, 2015 & Drought Impact Report, n.d).

#### 4. Data

##### 4.1. 1 km Surface Soil Moisture from Sentinel-1 C-SAR

The Sentinel-1 (hereafter, S-1) satellite constellation consists of two identical satellites, the Sentinel-1A and the Sentinel-1B, sharing the same orbital plane (Table 2). It is the first of five missions of the Copernicus program of the ESA. Both satellites’ SAR systems operate in the C-Band whose Frequency ranges from 4.20 to 5.75 GHz (which corresponds to a Wavelength of 5.22 cm to 7.14 cm) and are capable of dual polarization acquisition. Due to the dual satellite constellation, a temporal resolution of 1.5 - 4 days is governed over Europe. As seen in Figure 8, the S-1 dual satellite observation scenario results in areas of high observation frequency next to areas of low observation frequency; therefore, the temporal signal quality of this dataset varies strongly.

<b>Launch dates</b>	Sentinel-1A	03 April 2014
	Sentinel-1B	25 April 2016
	Operational lifespan:	7 years
<b>Payload:</b>	C-SAR	
<b>Resolution + Swath Width:</b>		
<b>Mode</b>	<b>Swath</b>	<b>Spatial Resolution</b>
Strip Map Mode:	80 km	5 x 5 m
Interferometric Wide Swath:	250 km	5 x 20 m
Extra-Wide Swath Mode:	400 km	25 x 100 m
Wave-Mode:	20 km x 20 km	5 x 20 m
<b>Mission Orbit:</b>		
	Orbit Type:	Sun-synchronous near-polar circular
	Orbit Height:	693 km
	Inclination:	98.18°
	Repeat Cycle:	175 orbits/12 days

Table 2: S-1 mission details (Sentinel-1: Mission Details, 2018)

The S-1 data used for this investigation is the 1km Surface Soil Moisture (SSM) data, which describes the water content of the soil's topmost layer (about 5cm) in degree saturation. Additionally, the backscatter data itself, acquired in the interferometric wide swath modes, is also used. The pixel spacing in the IW mode corresponds to a potential resolution of 1km. Furthermore, although the S-1 CSAR system acquires in both VV and VH polarizations when observing in the IW mode, only the VV polarization is used for the SM applications as this polarization is more highly sensitive to soil moisture than cross-polarized observations.

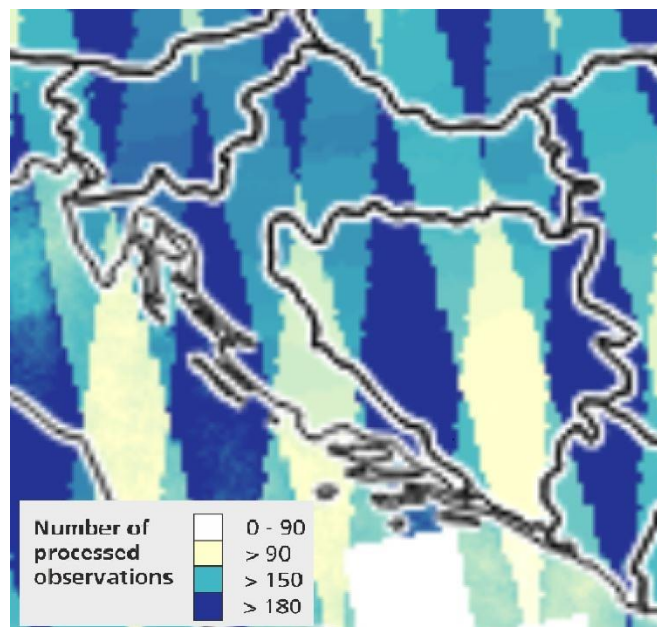


Figure 8: Sentinel-1 dual satellite temporal coverage over Croatia (TU Wien Department of Geodesy and Geoinformation, 2017)

To derive SM directly from backscatter observations the S-1 SM retrieval algorithm was used. This algorithm is an adaptation of the TU Wien Change Detection Model, where changes in backscatter are interpreted as changes in soil moisture while other surface properties such as surface roughness and

geometry and average vegetation are considered as static parameters. As shown in Equation 5 the backscatter value itself ( $\sigma^\circ(\theta, t)$  with  $\theta$  and  $t$  being the incidence angle and the time respectively) is normalized to the local incidence angle of  $40^\circ$  with the use of the slope model parameter ( $\beta$ ), which describes the backscatters' dependency to the local incidence angle. Furthermore, the backscatter value is then linearly scaled between the maximum dry- and wet- reference values, resulting in degree of saturation values (TU Wien Department of Geodesy and Geoinformation, 2017).

$$\sigma_{40}^\circ = \sigma^\circ(\theta, t) - \beta \cdot (\theta - 40^\circ)$$

*Equation 5: locally normalized backscatter (TU Wien Department of Geodesy and Geoinformation, 2017)*

Before further processing is done, backscatter values above -5dB (very high backscatter values originate from man-made objects that act as corner reflectors) and below -20dB (very low backscatter values originate from standing water surfaces) are masked out and discarded as they are highly unlikely to carry any soil moisture signal. Variable vegetation features are water content, crop row orientation, size, density and wind bending. Variable features concerning soil are roughness, tillage and moisture. Although the SAR backscatter field scale lies at 10 m, the data is resampled to 500 m to further reduce the impact of these highly variable vegetation and soil features. Through this resampling the soil moisture signal holds while these underlying small-scale signals sum up incoherently and can be assumed to be eliminated. This resampling also reduces the SM noise level, which is estimated by error propagation from the S-1 backscatter observations through the retrieval model (TU Wien Department of Geodesy and Geoinformation, 2017).

Because the S-1 SM algorithm does not produce reliable results for every surface, three masks are implemented to remove all misleading values from the SM dataset. The water mask classifies each pixel with a value lower than -17dB as water and automatically sets these pixels to 'no-data'. The low radar sensitivity mask classifies pixels with low sensitivity. The normalized sensitivity  $S_{40}$  is defined in Equation 6 as:

$$S_{40} = \sigma_{wet(40)}^\circ - \sigma_{dry(40)}^\circ$$

*Equation 6: The normalized sensitivity defined as the difference between the normalized historically driest and wettest backscatter value of that particular grid point. (TU Wien Department of Geodesy and Geoinformation, 2017).*

As this sensitivity is a measure for accuracy and reliability of the algorithm, it is important to mask out pixels with a low value. A threshold of 1.2 dB is used resulting in a mask which mainly covers urban areas (TU Wien Department of Geodesy and Geoinformation, 2017). Finally, a slope mask is implemented to mask out signals from steep terrain. The terrain correction pre-processing step does not completely remove errors from topography; therefore, all pixels which lie on a slope (derived from the SRTM digital elevation model) higher than 30% are masked out.

The processing- and output grid reference of the S-1 dataset is the Equi7Grid. Designed to efficiently handle the archiving, processing and display of high-resolution raster data over land, the Equi7Grid is a spatial reference system defined for the entire Earth and consists of seven planar sub grids for each continent, referenced to the ellipsoidal WGS84 datum. (TU Wien Department of Geodesy and Geoinformation, 2017).

Example SM Datafile is named:

M20141003\_164759--\_SSM-----\_S1AIWGRDH1VVA\_148\_C1003\_EU500M\_E048N006T6

- Master branch processing software code
- From 2014-10-03, at 16:47:59
- Derived from the S-A1 IWGRDH image = IW mode in VV polarization in the ground range detection high resolution format. This is SAR intensity data that has already been focused, multi-looked and projected to ground range, yielding images in ellipsoidal coordinates at optimal sampling of 10m.
- In the VV polarization
- from the ascending (A) orbit with the no. 148
- processor version C1003 which includes all three pre-processing masks (for permanent water, low radar sensitivity and steep terrain)
- projected into the European Equi7 grid in 500m spacing and over the EO48N006T6 tile

#### 4.2. Soil Moisture and Precipitation data from the Global Land Data Assimilation System

The Global Land Data Assimilation System (hereafter, GLDAS) generates optimal fields of land surface states and fluxes through the use of advanced land surface modeling and data assimilation techniques. GLDAS integrates a huge quantity of satellite- and ground- based observational data products and executes a global assimilation at high resolutions (2.5° to 1 km).

The second version of the NASA GLDAS products has two components. In this investigation component 2.1, simulated by the Noah land surface model, was used. The main objective of the GLDAS 2.1 dataset is to provide up-to-date global land surface model outputs, using observation-based forcing, while preserving consistency of the long-term climatology to the extent possible. Component 2.1 is forced with a combination of model and observation based forcing datasets. This dataset extends from 2000 to present. The used simulation was forced with NOAA (National Oceanic and Atmospheric Administration)/ GLDAS (Global Data Assimilation System) atmospheric analysis fields, the disaggregated GPCP (Global Precipitation Climatology Project) precipitation fields and the AGRMET (Air Force weather agency's AGRicultural METeorological modeling system) radiation fields (Beaudoin, H. and M. Rodell, NASA/GSFC/HSL, 2015). The following GLDAS parameters were used for this investigation:

Soil-Moi\_10cm\_inst :

- Parameter= Soil Moisture [kg/m<sup>2</sup>]
- Resolution= 0.25°
- An instantaneous variable
- Depth/Height interval= 0 – 10 cm

Rainf\_tavg

- Parameter= Rainfall precipitation rate [kg/m<sup>2</sup>/s]
- Resolution=0.25°
- Variable averaged over the past three hours

### 4.3. ESA Climate Change Initiative Landcover (CCI – LC) Dataset

Within the United Nations Framework Convention on Climate Change, Essential Climate Variables databases were required. The European Space Agency's has achieved a significant contribution to this database with its Climate Change Initiative (CCI) program. Within the CCI program, the Landcover (LC) project was established to define specifications of a global landcover product that is to meet the requirements for a spectrum of modeling communities and approaches. Furthermore, this project is intended to develop the most efficient method to discriminate various data types and map landcover globally in a temporal and spatial consistent manner. For this investigation the landcover map from the epoch 2010 was used. Because the epoch stretches from 2008 – 2012, this landcover dataset has a temporal resolution of 5-years. Through the use of the MERIS FR sensor a spatial resolution of 300 m was achieved. Based on all MERIS FR and RR data from 2003 – 2012, a 10-year global landcover map was generated and served as a baseline to derive the landcover map used in this investigation. The SPOT-VGT (SPOT Vegetation) time series was then implemented to update this baseline map.

The landcover classes were defined using the United Nations Landcover Classification System (UN-LCCS), a hierarchical classification. In this investigation both the "level 1" and "level 2" legend was used and simplified to allow for visual interpretation during this investigation. Figure 9 shows how the classes have been reduced.

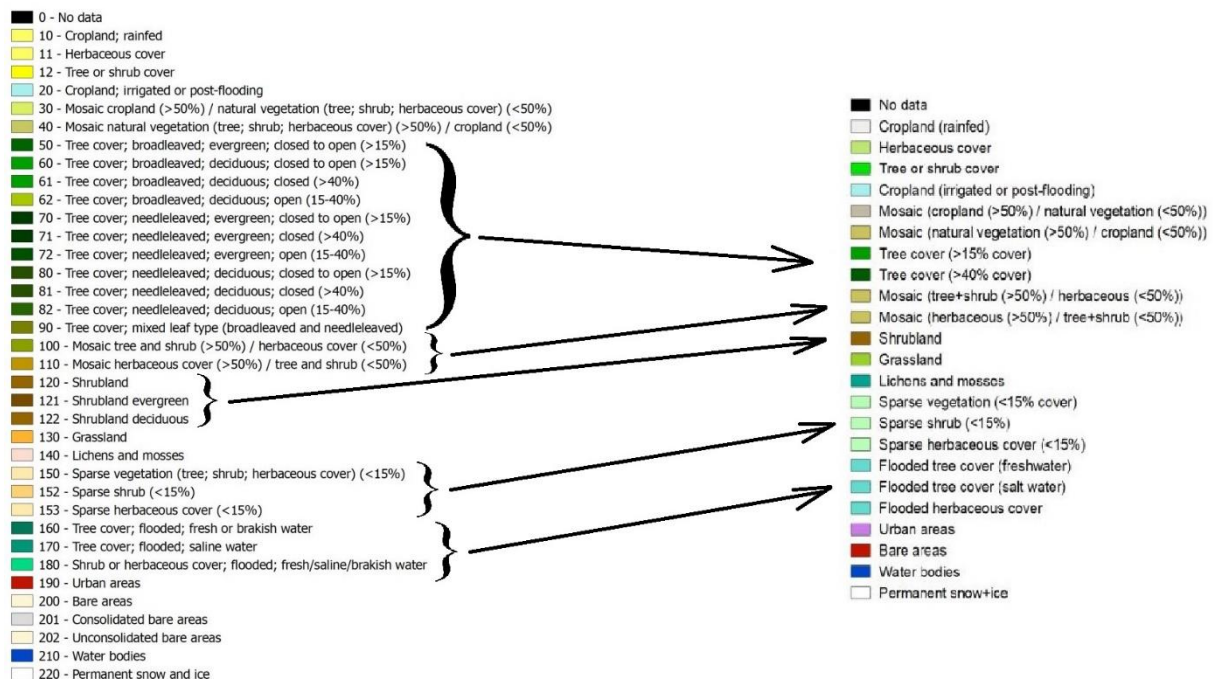


Figure 9: CCI – LC Class simplification.

After simplifying the classes and color scheme of the CCI-LC map, Figure 10 can now be used to compare results from the spatial analysis of both soil moisture datasets with Croatia's landcover.

## ESA CCI Land Cover Map

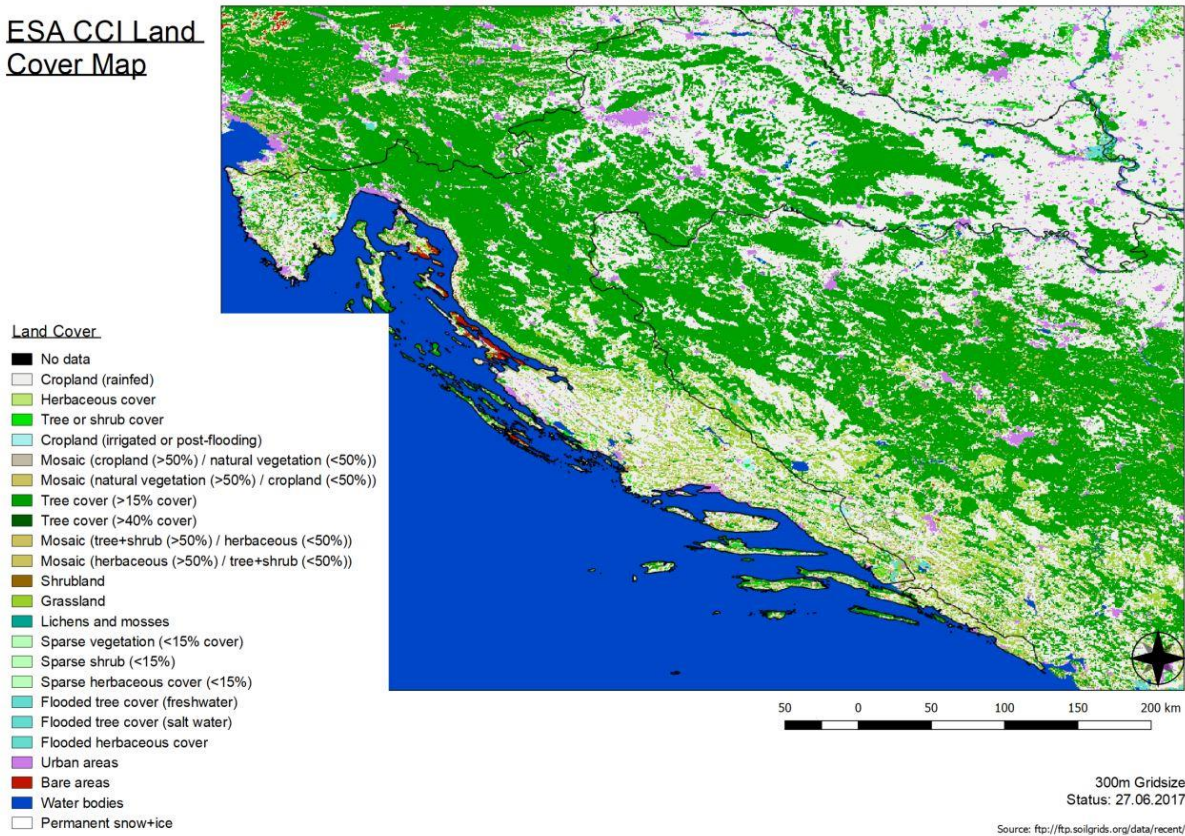


Figure 10: ESA CCI landcover map used for investigation

### 4.3.1. Description of Simplified CCI-LC Classes

According to the Food and Agriculture Organization of the United Nations (FAO), landcover is always assessed at fullest development. Following is a description of the CCI – LC classes simplified for this investigation:

#### a) Cropland (rainfed)



Figure 11: Arable parcels separated by stone walls (Malta). Photo: B. Kosztr & Small-parcel arable land (near Vienna, Austria). Photo: Gy. Büttner

This simplified CCI-LC class (Figure 11) is defined by rainfed plots of land under agricultural use for harvesting non-permanent crops annually. Usually, due to a crop rotation system, fallow land parcels are often included. This class not only includes regular annual crop along with the stubble of harvested crops and the fallow plots under crop rotation but also vegetation, dirt roads, stone walls and

hedgerows between the arable crop parcels. Patches of other cultivation types such as plantations or pastures are also included in this class, given the patch is less than 25 ha and more than 75% of this land is under a rotation system. (Kosztra, 2017)

b) Tree cover (>15% cover)



Figure 12: Clearcut pine forest (Hungary) Photo: B-. Kosztra & Transition from grasslands to forest by natural succession (due to lack of grazing) in the Carpathians (Romania). Photo: Gy. Büttner

This simplified CLC class (Figure 12) defines a forest landcover with more than 15% cover by trees. The simplification combines all four original tree cover class types - needleleaved evergreen and needleleaved deciduous, as well as broadleaved evergreen and broadleaved deciduous trees. It also integrates both closed to open (tree cover between 15% – 100%) and open (tree cover between 15% – 40%) tree cover. Trees are defined with a minimum height of 3 meters and can reach greater than 30m (according to FAO).

c) Tree cover (>40% cover)



Figure 13: Mixed forest made up of deciduous forest intermixed with small (<25 ha) stands of coniferous trees (Austria). Photo: Gy. Büttner & Semi-natural coniferous forest in the Carpathian Mountains (Romania) Photo: B. Kosztra

Like the class “tree cover (>15%)”, this class (Figure 13) defines a forest landcover; however, here with more than 40% surface cover by trees (closed tree cover). This simplification combines all four original tree cover class types - needleleaved evergreen and needleleaved deciduous, as well as broadleaved evergreen and broadleaved deciduous trees. Trees are defined with a minimum height of 3 meters and can reach greater than 30m (according to FAO).



#### d) Grassland



Figure 14: Low-productivity grassland on karstic surface with scattered shrubs (Hungary). Photo: B. Kosztra & Species-rich natural grassland in nature conservation area (Hungary). Photo: B. Kosztra

This CLC class (Figure 14) is particularly defined for areas under no or moderate (maintenance mowing and shrub clearance for prevention of woody overgrowth is tolerated) human influence. Here, rough, rocky areas with patches of other (semi-) natural vegetation, uneven ground including slopes are expected. Nevertheless, at least 50% of the surface must still be covered by herbaceous vegetation. This class is still applicable for large areas wherein trees and shrubs grow, as long as trees occupy less than 30%, and shrubs cover less than 50%, of the considered surface. The grassland class can be found on either humid or dry growing conditions and can also include saline grasslands grown on temporary wet areas of saline soils. An irregular shape of large extent, usually further away from any larger settlements are some typical visible characteristics of this CCI-LC class.

#### 4.4. Soil Grids Dataset

The SoilGrids project, powered by the International Soil Reference and Information Center (ISRIC), is an independent, science-based foundation founded in 1966, has a mission to serve the international community with information about the world's soil resources to help set focus on global issues such as the effects of global warming or deforestation. ISRIC illustrates soil type classifications in accordance to the World Reference Base (WRB) and the USDA classification systems. For this investigation only the WRB classification system with a spatial resolution of 250m was used (SoilGrids, 2019).

## TAXNWRB Soil Grid Data in Croatia

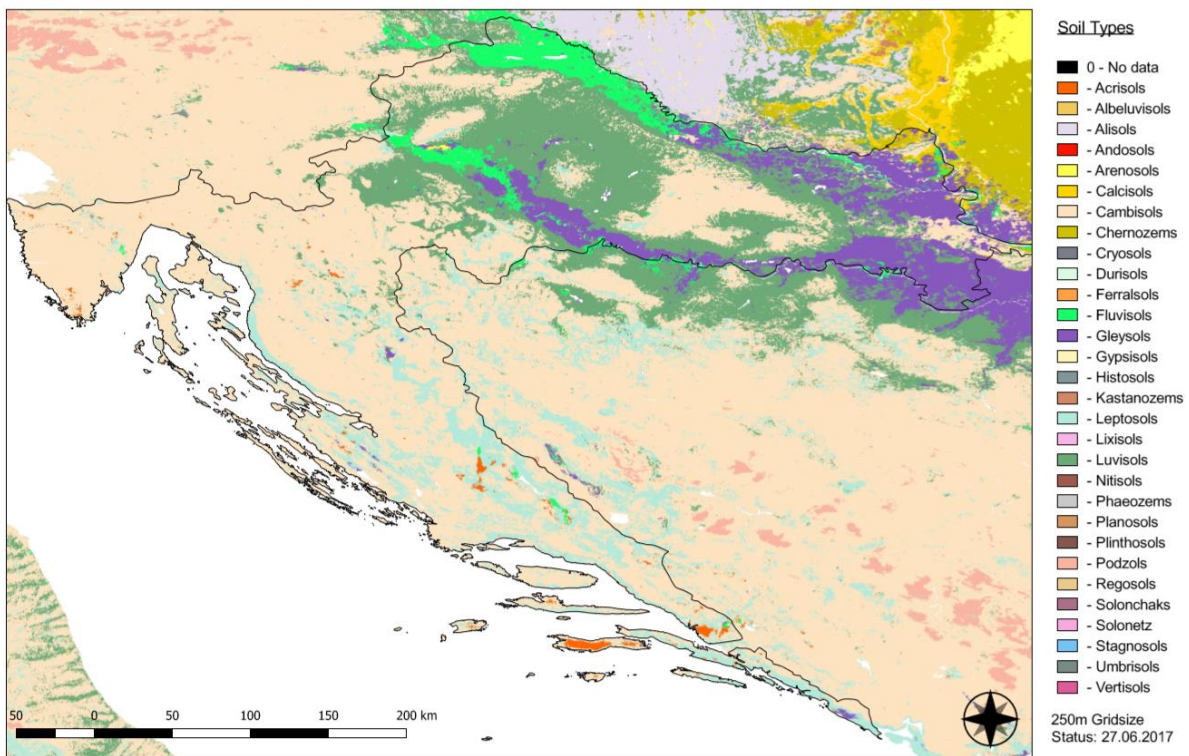


Figure 15: TAXNWRB Soil Grid Data in Croatia

Majority of soil covering Croatia are Cambisols. Cambisols are the most common soil type on continental land. These soils do not explain the uncommon surface soil moisture phenomena we see in Croatia during dry spells because they occur in all environments and under all kinds of vegetation; therefore, it can be assumed that the changes seen arise from the landcover differences rather than the soil type.

As seen in Figure 15, the occurrence of the Cambisol soils in the north-east region of Croatia is much less than in the coastal region of the country. Here, Luvisols, Fluvisols and Gleysols are more dominant. Most of the soils in Croatia make good agricultural land and are intensively used. In temperate climates, Cambisols are among the most productive soils on earth. Luvisols are widely used for agriculture. Soil with a clay enriched subsoil, a clay horizon, have a high cation exchange capacity and a high base saturation. The presence of Fluvisol soil is an indicator for saturated land and a close approximation to rivers and lakes. This soil type is found on alluvial plains, river fans, valleys and tidal marshes. Gleysol soils is a wetland soil that is often saturated with groundwater. They are found in depression areas and low landscape positions with shallow groundwater. Gleysols are naturally covered with swamp vegetation and isn't used in its virgin state as it is too highly saturated. Only when it is artificially drained can this soil be used for agricultural purposes. Gleysols develop where drainage is poor, either because the water table is high or because precipitation inputs at the surface are not able to drain freely. More detailed descriptions of the four most common soil types in Croatia are listed in Table 3.

Soil Type	Description
<b>Cambisols</b>	<p>Cambisols have a fragic horizon, the soil has a structure and a porosity pattern such that roots and percolating water penetrate the soil only along interped (Peds= aggregates of soil particles formed as a result of pedogenic processes. A natural organization of particles separated by pores or voids) faces and streaks. Other horizons much deeper from the soil surface are more strongly cemented and have high contents of Iron oxides but the top layer soil is relatively porous.</p> <p>Cambisols combine soils with at least an incipient subsurface soil formation. Transformation of parent material is evident from structure formation and mostly brownish discoloration, increasing clay percentage, and/or carbonate removal. They are characterized by slight or moderate weathering of parent material and by absence of appreciable quantities of illuvial clay and organic matter.</p> <p>Parent material: medium and fine textured materials derived from a wide range of rocks.</p>
<b>Fluvisols</b>	<p>Fluvisols are soils that have fluvic material (fluviatile/ river, marine/ ocean or lacustrine /lakes origin). These soils are typically able to hold more water than Cambisols. This soil is found in river plains and fans, valleys, lake depressions and tidal marshes on all continents and in all climate zones. Although many Fluvisols are flooded periodically under natural conditions, no groundwater and no high salt contents are present in the topsoil.</p> <p>Parent material: mainly genetically recent, fluvial, lacustrine and marine deposits.</p>
<b>Luvisols</b>	<p>As a result of clay migration, Luvisols are soils which have an argic horizon starting at less than 100cm from the soils surface (Argic = a soil horizon which has a distinctly higher clay content than the overlying horizon). Around this horizon, Luvisols have a high base saturation. This soil is most commonly found in flat or gently sloping landscapes in cool temperate and warm regions with distinct dry and wet seasons.</p> <p>Parent material: a wide variety of unconsolidated materials including glacial till, and aeolian (deposited by wind), alluvial (deposited by lakes) and colluvial (deposited by mass movement) deposits.</p>
<b>Gleysols</b>	<p>Gleysols are soils having clear signs of groundwater influences and evidence of reduction processes. This soil type is mainly found in low-lying landscapes with a high groundwater table, tidal areas, shallow lakes and sea shores.</p> <p>Parent material: a wide range of unconsolidated materials, mainly fluvial, marine and lacustrine sediments.</p>

Table 3: Detailed description of most common soil types in Croatia (IUSS Working Group WRB, 2015).

The sediment size of clays is so small and well sorted, that the pores and voids between the sediments along with the large surface area of the sediment, allow water to percolate only very slowly. Clay has a high water-holding capacity. The higher the clay content of the soil, the more water the soil can hold

and the longer it takes for the soil to dry out to the extent where the high soil moisture response during extreme dryness could be detected. Simply through the SoilGrids soil type map it should theoretically be possible to show the spatial pattern expected of the regions of Croatia where surface soil moisture differs from the expected GLDAS dataset.

#### 4.5. The International Hydrogeological Map of Europe

The twenty-five map sheets of the International Hydrogeological Map of Europe at the scale 1 : 1,500,000 (IHME 1500) were digitized by the Federal Institute for Geosciences and Natural Resources in Germany (Bundesanstalt für Geowissenschaften und Rohstoffe, BGR) with expert contributions under the auspices of the International Association of Hydrogeologists (IAH) and support by the Commission for the Geological Map of the World (CGMW).

The IHME 1500 was based on the International Geological Map of Europe 1 : 1,500,000 (IGK1500); therefore, they share the same scale, topography and projection. Delineations and lithological attributions of the aquifers were also partly derived from the geological information mapped in the IGK 1500.

The IHME 1500 consists of Lithological classifications of defined aquifers at five aggregation levels. As seen in Figure 16, the aggregation levels 3 and 5 were used for this investigation. Through this dataset a distinction between hard rock, gravel, sand and clay surfaces are made. Mixed classes such as “marlstones and sands” and “sandstones and clays” were not taken into consideration.

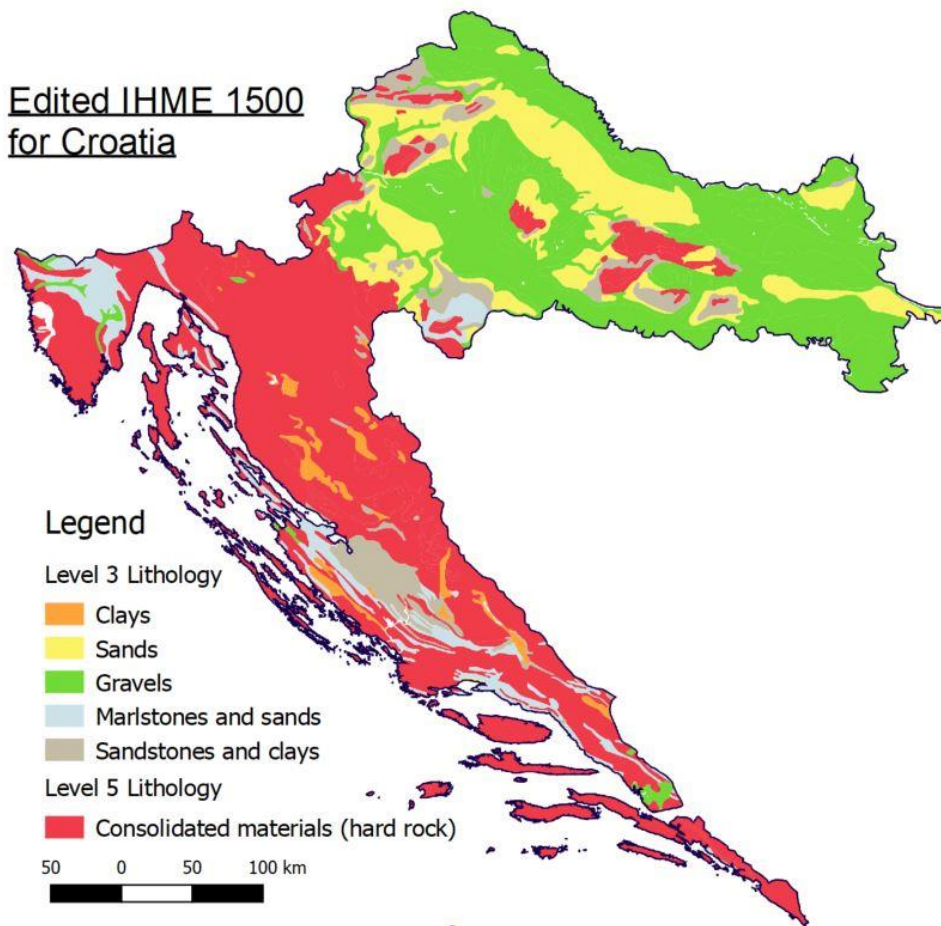


Figure 16: IHME 1500 aggregation level 3 and level 5 lithology information for Croatia.

Additionally, the IHME 1500 dataset seen in Figure 17 provides information about soil which has becomes saturated with seawater. As salt drastically alters the backscatter behavior of the reflecting microwaves; however, investigating these regions through the S-1 Satellite constellation is not possible as their proximity to the ocean falsifies backscatter results.



Figure 17: IHME 1500 Seawater intrusion in Croatia.

## 5. Methods

In Croatia's dry summer months, the surface soil layer of the land becomes extremely dry, soil moisture levels are extremely low - GLDAS SM model data shows exactly this behavior. The SM data calculated through the S-1 backscatter measurements, however, show high SM levels during this same time. It is hypothesized that the soil becomes so dry that the signal penetrates deeper, revealing more reflective subsurface layers below and leading to volume scattering. With the following methods, an investigation as to when and under which circumstances S-1 SM data deviate from the GLDAS SM model data. Through a temporal analysis both datasets can be compared with precipitation data over a span of time to show exactly when S-1 SM ceases to correlate with the GLDAS SM model. A spatial illustration of the correlation between the model data and satellite information over different time epochs is made. Through this correlation coefficient map a spatial comparison with landcover, soil type and lithology data of Croatia is made to deduce under which conditions C-band microwaves are able to travel through the dry soil layer and reflect off of subsurface layers – to understand where this hypothesized phenomenon occurs.

In order make the two datasets comparable with each other in any way the GLDAS SM data with the S-1 SM data the datasets must first be both temporally and spatially matched. S-1 data comes in equi7grids while GLDAS has a spatial resolution of 0.25°; therefore, spatial matching had to be done before comparisons between the datasets could begin. The acquisition of both datasets also happens at different times; therefore, a temporal matching must also be made to fit the two datasets to one another and make them comparable. This matching which is done through the pytesmo python package temporal matching module. This package uses the index of the reference time-stamp to find

the nearest time index for the comparison data-set to match observations to their closest temporal neighbor. Furthermore, because S-1 data is known to react to frozen soil as if it were a dry soil, a filter was used remove data during times when the soil temperature model is under 0°C. After this initial editing the temporal and spatial analysis can be executed.

During this investigation all data processing steps where completed in Spyder, an open source software used to script the programming language Python.

### 5.1. Temporal Analysis

The goal of this temporal analysis is to understand during which time of year and for which timespan S-1 SM falsely begins to rise in the absence of precipitation. After the initial pre-processing, time series plots were made at five different points (Figure 18) across Croatia to examine how the soil moisture values of the GLDAS and Sentinel-1 datasets change over time. Although the entire Sentinel-1 SM and backscatter data of Croatia was provided for the years 2015, 2016 and 2017, for this investigation the entire dataset is not always considered. The abbreviations defined in Table 4 are used to differentiate between time epochs dealt with separately during the temporal analysis of the S-1 and GLDAS soil moisture data.

<b>Short:</b>	01.06.2015 - 31.08.2015
<b>Summer:</b>	June - September for years 2015 - 2017
<b>Year:</b>	01.01.2017 - 01.01.2018
<b>Total:</b>	Entire time series from 2015 - 2017

*Table 4: Used abbreviations for time epochs*

The ‘Short’ time epoch defines the temporal analysis of just one summer. The summer of 2015 was chosen because of the exceptional dry and hot conditions witnessed in the GLDAS dataset in this time (also see Figure 7). The ‘Summer’ time epoch is defined to analyze the sum of all summer data. Adding the data of the summers of 2016 and 2017 to the analysis facilitates a climate examination rather than a concentrated insight into exceptional weather circumstances of one single year. The ‘Year’ time epoch is defined to evaluate an entire year. The year of 2017 was chosen again because of the exceptional dry conditions witnessed in the GLDAS dataset.

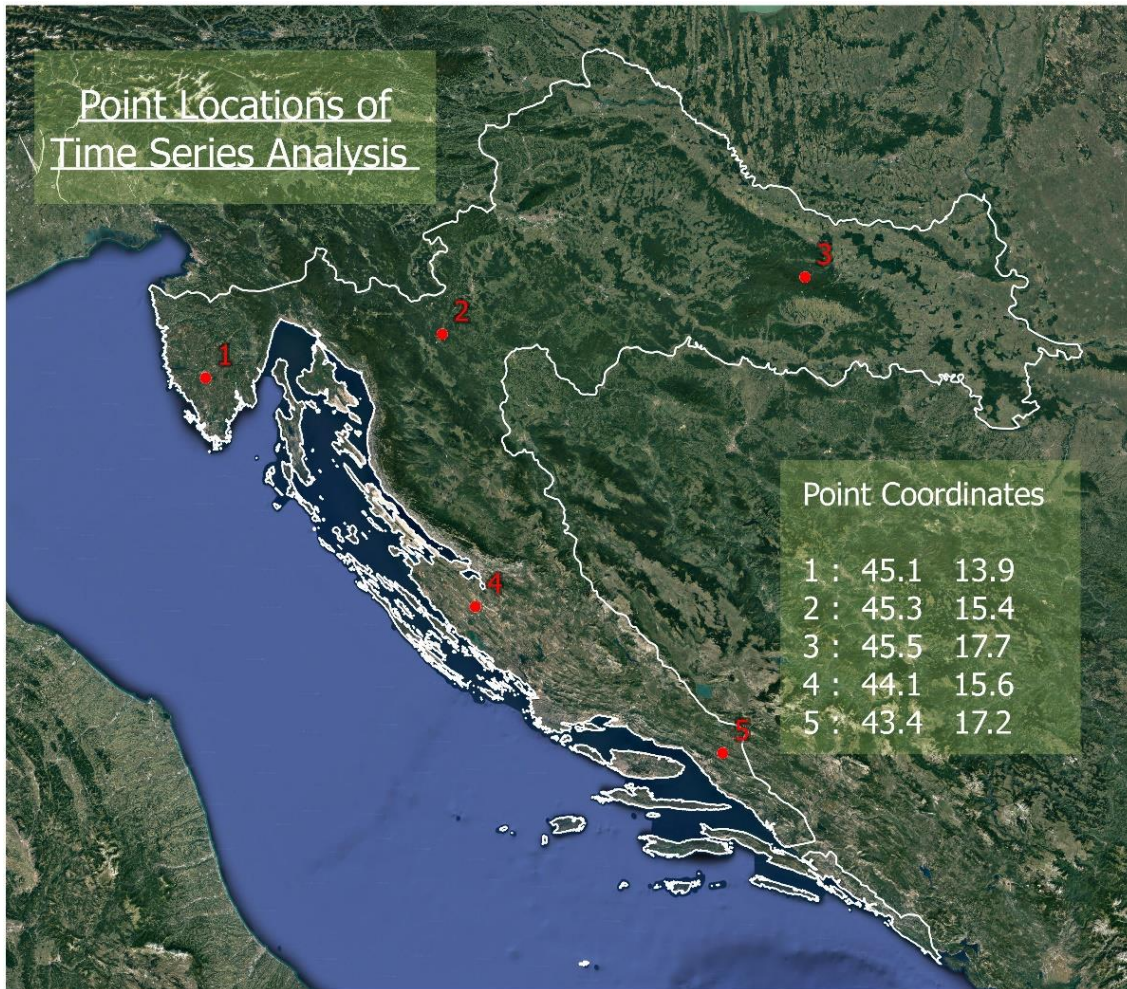


Figure 18: Point locations of temporal analysis - time series plots

The five points in Croatia depicted in Figure 18 and described in Table 5, over which the time series analysis is done was chosen to cover both inland and coastal regions as well as the northern, wetter, region and the south, which sees very little rain during the summers. For each of the five points, the S-1 and GLDAS soil moisture values as well as the recorded precipitation was plotted for each of the four epochs defined in Table 4.

Point of interest	Av. annual Rainfall (see also appendix Table 8)	Biogeographical region	Landcover type	Soil type	Lithology
1	482 mm	Mediterranean	Cropland	Cambisols	Consolidated materials
2	358 mm	Continental	Tree cover	Cambisols	Consolidated materials
3	329 mm	Continental	Tree cover	Cambisols	Consolidated materials
4	387 mm	Mediterranean	Cropland	Leptosols	Partly consolidated materials
5	425 mm	Mediterranean	Grassland	Leptosols	Consolidated materials

Table 5: Description overview of temporal analysis points of interest. See appendix Table 8 for further average annual rainfall data calculated from the GLDAS rainfall dataset.

## 5.2. Spatial Analysis

The goal of this spatial analysis is to uncover and geographical patterns and trends of the subsurface scattering during times of low surface soil moisture levels and deduce under which circumstances such subsurface scattering arises. A spatial illustration of the correlation between the model data and satellite information over different time epochs is made. Through this correlation coefficient map a spatial comparison with landcover, soil type and lithology data of Croatia is made to deduce under which conditions C-band microwaves are able to travel through the dry soil layer and reflect off of subsurface layers – to understand where this hypothesized phenomenon occurs.

The deviation of the datasets seen in the temporal analysis can be numerically described, and furthermore be spatially visualized, through Spearman's rank correlation coefficient. When calculating the Spearman correlation coefficients between the GLDAS soil moisture and the S-1 SM data, the time epochs defined in Table 4 were used. The spatial analysis was done for the entire area of interest.

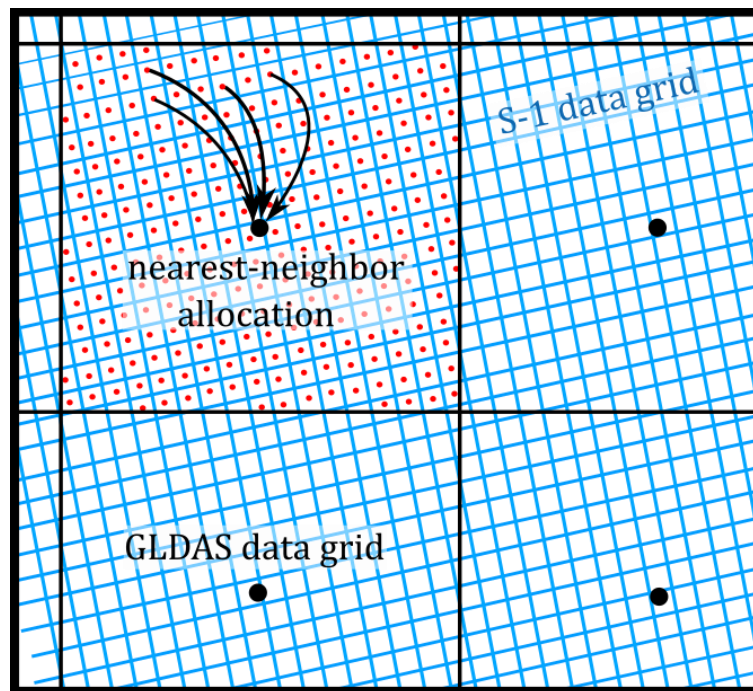


Figure 19: Nearest neighbor GLDAS data for S-1 raster information to allow the calculation of correlation coefficients between two datasets with varying spatial resolutions.

As shown in Figure 19, to create a spatial raster of correlation coefficients from two datasets with different spatial resolutions, each Sentinel-1 raster point is given a nearest neighbor GLDAS point with which the correlation coefficient was then calculated from. Therefore, the spatial analysis inherits the raster geometry of the S-1 dataset. As a result, raster files are created, in which the correlation coefficients have been calculated for each S-1 data point, for all four epochs defined in Table 4.



Through the open source program QGIS, the color scale for the correlation coefficient results is stretched to a uniform scale.

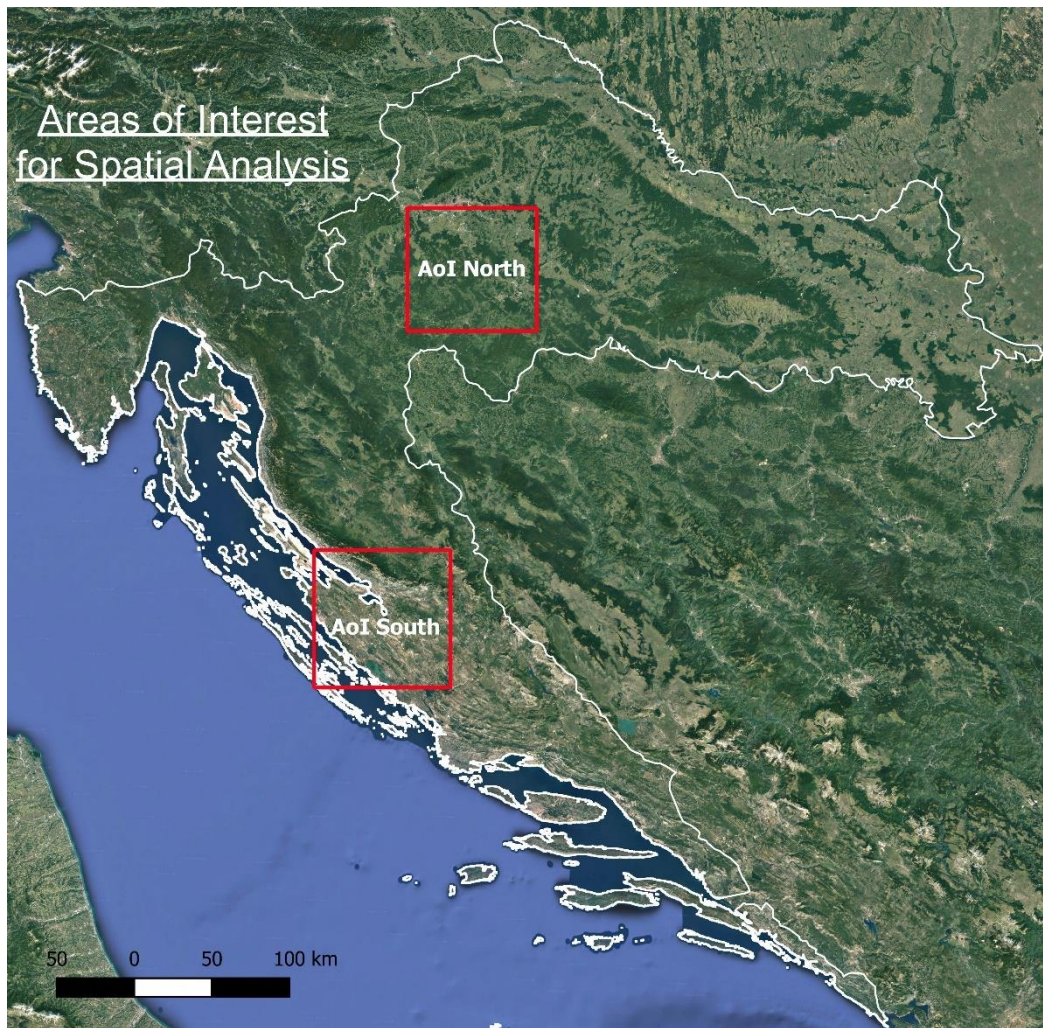


Figure 20: Spatial distribution of northern and southern area of interest for spatial analysis.

Figure 20 depicts the two areas of interest used in this investigation to closely examine spatial differences between a continental region in the north and a coastal region in the south of Croatia.

### 5.3. Relating subsurface scattering to physical processes

It became possible to compare the correlation coefficients between S-1 SM data and the GLDAS SM model data for different time epochs over Croatia with other spatial data of Croatia by mapping the results with the method described above. All correlation coefficient maps in this investigation were given a standardized color scale depicted below in Figure 21.

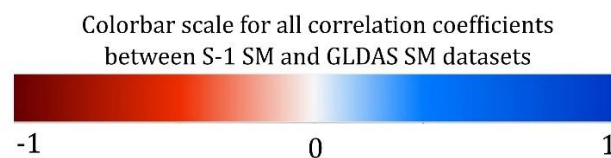


Figure 21: Colorbar scale used for all correlation coefficients maps during this investigation

A simple visual comparison is made by loading both the correlation coefficient maps and google satellite images as well as lithology class information into the open source software QGIS. After reducing the opacity of the correlation coefficient layer, a study of correlation patterns coinciding visually with landscape patterns in the satellite imagery and lithological patterns was performed.

To concretize the relationships between landcover type and S-1 to GLDAS correlation coefficients, like with the google satellite images, the correlation coefficient spatial distribution map was also superimposed with ESA's CCI-LC dataset in QGIS. Furthermore, the QGIS raster calculator was used to create separate correlation coefficient raster datafile for each major simplified landcover and soil type. For example, the code shown below in Equation 7 was used to create a raster datafile to depict the correlation coefficients compiled over the 'short' epoch only for the cropland landcover type, designated with the code number 10.

```
((("ESACCI-LC-Map" = 10) * "Croatia_correlation_short@1") + (("ESACCI-LC-Map"! = 10) + ("Croatia_correlation_short@1" + 100))
```

*Equation 7: Code used in QGIS raster calculator to show correlation coefficient over 'short' epoch only for the cropland landcover type*

With python matplotlib a simple statistical analysis of these raster images was then carried out. Minimum, maximum, mean and variance as well as a histogram of the correlation coefficient distribution for each landcover and soil type were calculated to investigate the backscatter behavior of Croatia's land surfaces and examine with which surface the sub-surface backscatter phenomenon can be identified.

## 6. Results

### 6.1. Temporal Analysis

Through the initial data visualization in Figure 22, it is seen that although these coordinate points are spread throughout the whole of Croatia (as seen in Figure 18), their soil moisture data follow the same trend. Between the years 2015 and 2017 all five coordinate points in Croatia demonstrate time series plots which show both Sentinel-1 SM and GLDAS SM data coherently rising and falling with the rainfall recorded; however, in some epochs during this two-year time series plot, the two datasets seem to deviate strongly from one another. Taking a closer look at Figure 23 it becomes clear that the S-1 and the GLDAS dataset lose their correlation to another when no rainfall is recorded for a longer period of time. These dry spells tend to happen during the summer months in Croatia.

While the percent soil moisture scale is on the left y-axis, the precipitation rate, given in mm/h, is plotted on the right y-axis. Depending on the length of the epoch plotted, the time scale axis changes accordingly. Additionally, a spearman's rank correlation coefficient between the two soil moisture datasets, over the given epoch, was also calculated to numerically express the temporal correlation seen in the time series plots.

According to the rainfall data from GLDAS, point of interest number 3 is the driest point with an average annual rainfall of 329 mm (Table 5); nevertheless, GLDAS SM data only drops under 25% once over the entire 3 year observation period seen in Figure 22. During this time, between June and October of 2015, GLDAS SM drops from around 30% to 18%. During this time S-1 records SM values between 30-35%. This clear divergence between mid-March and end-October 2015 is seen in all 5 Points. Using the time periods defined in Table 4, the given temporal analysis of the five points of

interest seen in Figure 18 are additionally plotted over the ‘year’, ‘short’ and ‘summer’ epochs ( Figure 23(a) – (c)). Like the time series seen in Figure 23(a), both GLDAS SM data and S-1 SM data cohere with one another relatively well for the rest of the observed time period at point 3 – the overall spearman’s rank correlation coefficient is -0.147. At point 2 the GLDAS dataset frequently measures rainfall between 2015 and 2017; however, most of this recorded rainfall merely amounts to around 1.5mm/h.

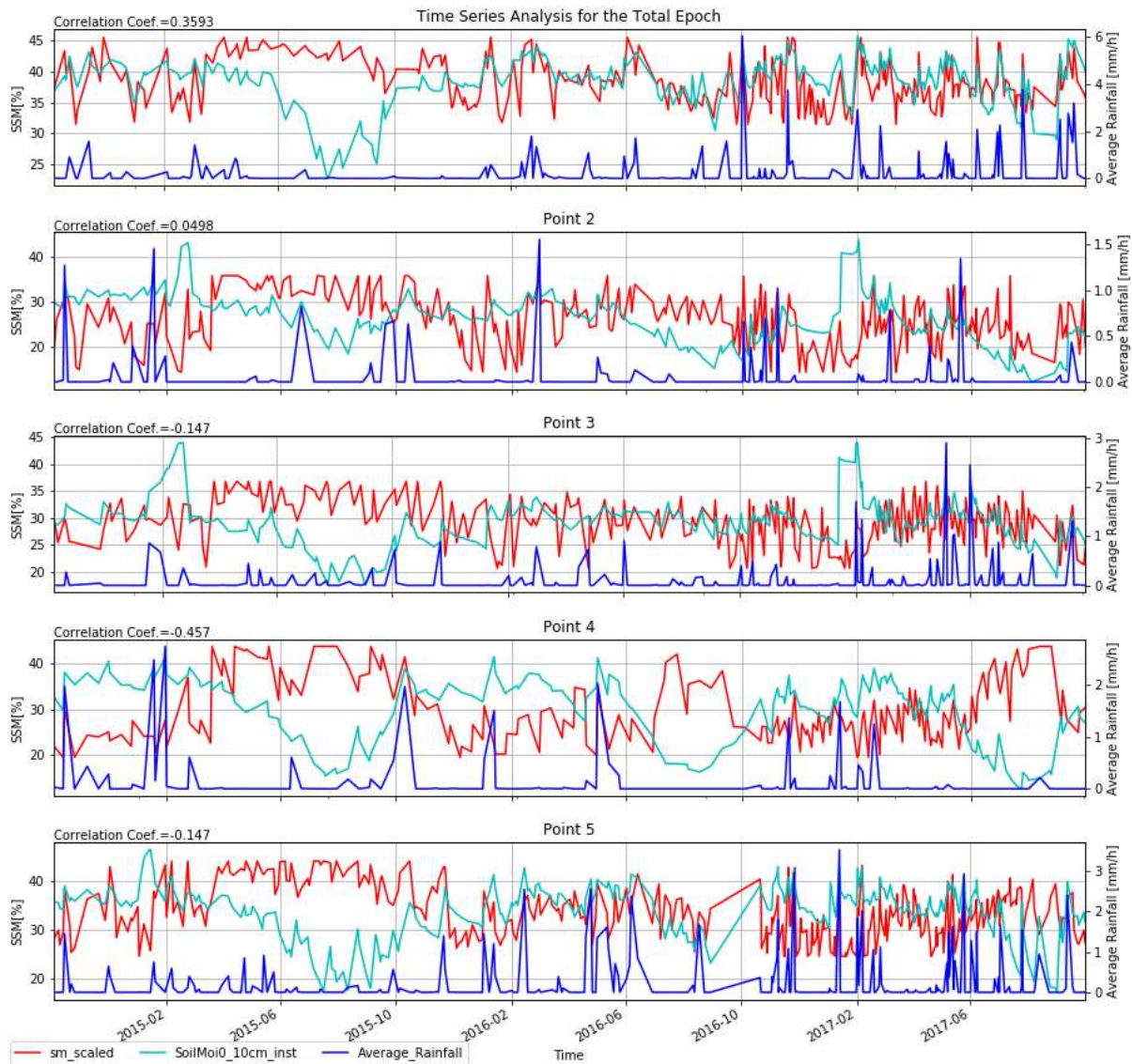


Figure 22: ‘Total’ time epoch of the 5 points to show temporal trends over the entire 3 years (2015-2017)

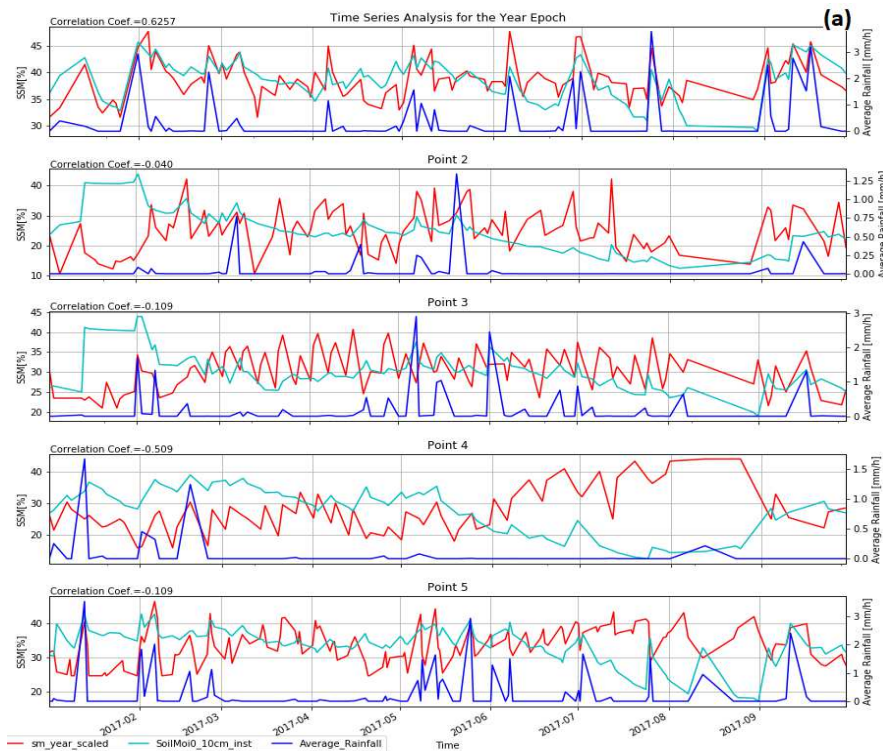
According to the rainfall data from GLDAS, on average it rains 358 mm (Table 5) annually at point of interest 2, only a little more than at the driest point 3. At point 2, a clear divergence between the soil moisture datasets is seen from June 2016 to October 2016 at point 2, which can also be seen very clearly in the time series of point 4. Here, during the time in which it does not rain whatsoever, the GLDAS SM steadily drops to 17% while S-1 SM rises to more than 35%. Point 4, which is seen to have an average annual rainfall of 387 mm (Table 5) displays this same pattern once more between June and September 2017, again a time in which no rain fell. Especially the time series analysis of 2017 (seen in Figure 23(a)) at point 4 displays a strong negative correlation between the two soil moisture datasets between June and September 2017, during which time no rain was recorded. The spearman’s rank

correlation coefficient at this point over the year 2017 is -0.51, also representing the divergence during these months.

As seen in Table 5, point of interest number 5 has an average annual rainfall of 425 mm. This is the southernmost point of interest, and the only point on which grassland covers the surface. Again, in Figure 22, the SM dataset divergence in the summer of 2015 is witnessed. During this time, it does not rain substantially but still S-1 records SM levels between 40 – 45%. Between July and October 2017, it rained with a measured downpour of more than 1mm/h on four occasions. Through Figure 23(a) a inverse correlation between rainfall and S-1 SM data at point 5 crystalizes. While it is expected that SM levels rise during rain occurrences, S-1 SM levels drop sharply by about 10% during all four downpours.

Figure 22, Point 1, shows correlating S-1 SM and GLDAS SM data until mid-March 2015. This point of interest receives the most average annual rainfall of 482 mm (Table 5). Once again, at this point the two datasets diverge. As GLDAS SM steadily drops to below 25% in August 2015, S-1 SM rises up to and maintains 45%. During this time, it only rains once, with about 1.5 mm/h rainfall. At the end of September 2015, it begins to rain more frequently and stronger. At this time both datasets converge again and for the rest of the time period, until end of the year 2017.

Figure 23(a), Point 1 shows the highest correlation coefficient of 0.623 in the year 2017. The GLDAS rainfall dataset also shows rain amounts between about 0.5 mm/h and 3.5 mm/h at least once a month. In Figure 23(b) and (c) an even closer look is taken into only the summer months, June to September. Again, the time series of all points show periods where the S-1 SM is up to 15% higher than that of the GLDAS soil moisture values. At all points, with one exception at point 1 in the summer of 2017, the recorded GLDAS rainfall remains below 2 mm/h.



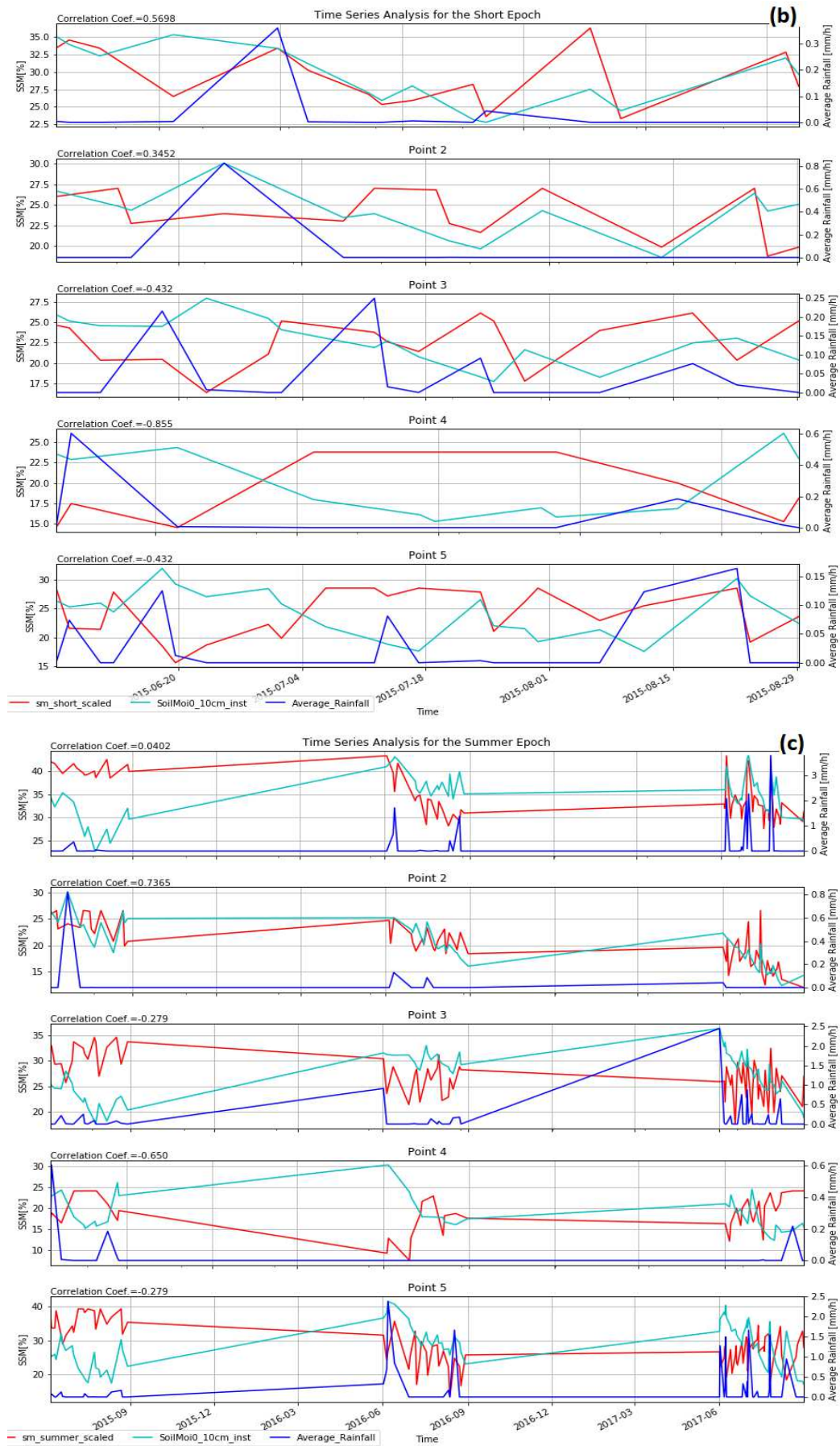


Figure 23: 'Year', 'Short' and 'Summer' time epoch of the 5 points to show temporal trends over the year 2017 and the summer of 2015

## 6.2. Spatial Analysis

Through calculating the Spearman's rank correlation coefficient between the GLDAS SM dataset and the S-1 SM dataset over different epochs it is possible to spatially illustrate the discrepancies seen in the time series plots between the datasets over the investigated time period. Figure 24 compares the spatial patterns in the correlation coefficients of Croatia over the epochs 'Total', 'Year' and 'Short'.

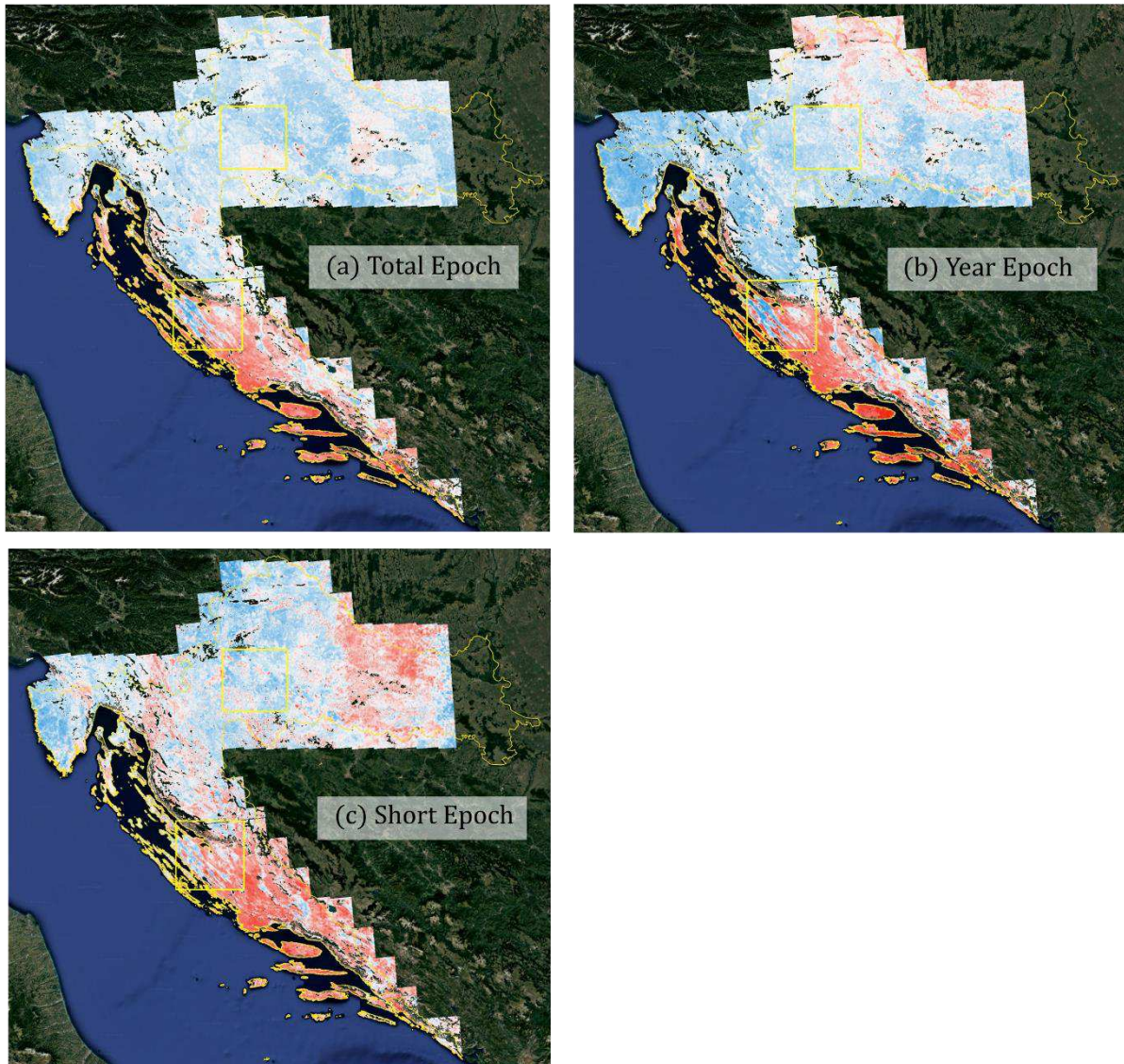


Figure 24: Spatial distribution of correlation coefficients between GLDAS SM and S-1 SM datasets over three different temporal epochs.

The correlation coefficient distribution map over the summer of 2015, seen in Figure 24 (c), shows the highest negative correlation patterns with the most negative values and the least amount of positive correlated areas. The mean correlation coefficient of the 'short' epoch over Croatia is -0.005 (see Appendix Table 7). As the observed length of time, and therefore also the amount of information, increases, the less extreme the correlation values become. Due to the summation of all correlation coefficients of the entire dataset provided, the correlation coefficient distribution map of the total time period, Figure 24 (a), shows the mildest negative correlations. The mean correlation coefficient of the 'total' epoch over Croatia is 0.032 (see Appendix Table 7). Because the average correlation

coefficient for each point over the given dataset is used, the positive correlation values seen in the wetter periods of the year, where S-1 SM and GLDAS SM correspond to one another, are seen to 'cancel out' the negative correlation values seen in the dry summer months. The goal of this spatial analysis is to identify where subsurface scattering occurs, which is hypothesized to be characterized by a negative correlation between the recorded S-1 SM data and the calculated GLDAS model data; therefore, only periods with low soil moisture will be considered.

The spatial patterns of the correlation coefficients over the entire year of 2015, Figure 24 (b), differentiates from both the 'short' and the 'total' epoch. The small-scale spatial correlation coefficient patterns of Figure 24 show not only similarities but also differences between the three different epochs. A strong negatively correlated south along with a more positive correlated north crystallizes regardless of epoch length. While the negatively correlated south remains relatively constant at this scale throughout all three epochs, the northern region of Croatia encounters different correlation coefficients depending on the epoch used. When using all data provided for this investigation (Figure 24 (a)), the north proves to be relatively homogeneous, whereas when only using data from the summer 2015 (Figure 24 (c)) a large part of the eastern region of the north also display negative correlations between the S-1 and the GLDAS datasets. A reason for this inconsistency could be because according to the Global Drought Observatory (GDO) the drought of 2015 hit this region strongest (see appendix Figure 46). Furthermore, point of interest number 3, which is defined for the temporal analysis in Figure 18, lies in this eastern region of Croatia and reveals that it rained about 80mm less in this region than in the rest of Croatia in 2015. When data from the 'year' epoch is used (Figure 24 (b)), negative correlation patterns arise in the uttermost northern region of Croatia – a region that shows positive correlation values in both the 'total' and the 'short' epoch. In 2017, the GDO recorded drought risk most frequently in this northern most area of Croatia (see appendix Figure 47). When plotting the median GLDAS SM values for all three defined epochs, Figure 25, both the northern and eastern regions consistently hold the lowest SM values of all of Croatia.

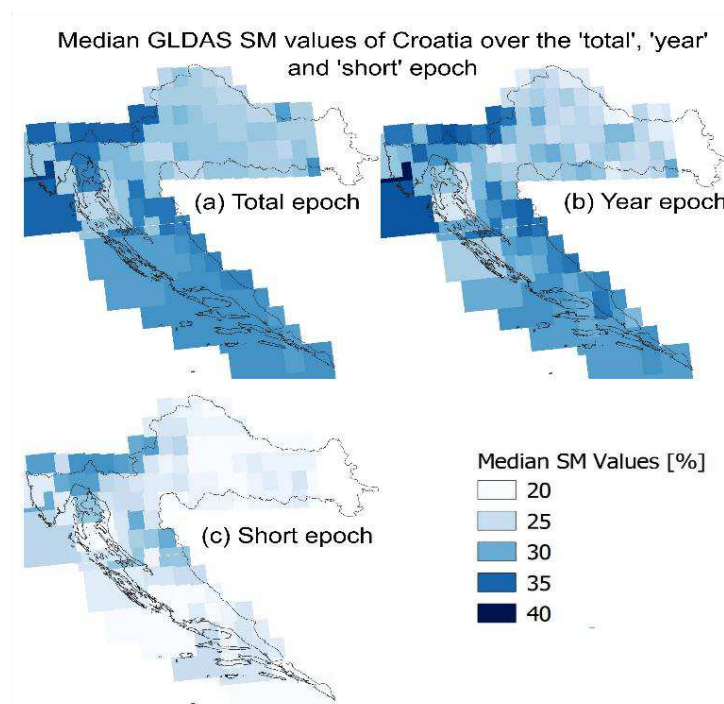


Figure 25: Median GLDAS SM values of Croatia over the (a) total, (b) year, and (c) short epoch.

For further investigation, only the ‘short’ epoch and the ‘total’ epoch, as seen in Figure 26, was used.

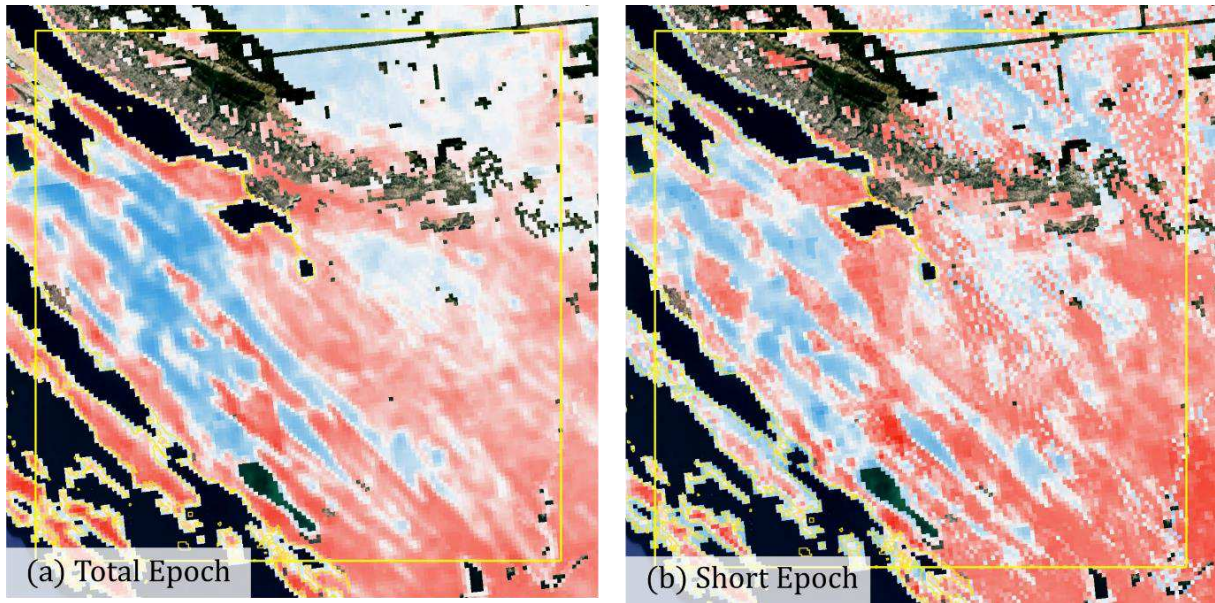


Figure 26: Southern area of interest, as seen in Figure 20, spatial distribution of correlation coefficients between GLDAS SM and S-1 SM datasets over two different temporal epochs.

Because the spatial map seen in Figure 26 (a) includes a much larger amount of data in the Spearman Rank correlation calculation, the result can be considered ‘smoother’; however, this dataset includes data from winter months, in which time the phenomena investigated in this paper is not expected. Nevertheless, Figure 26 (a) and Figure 26 (b) both show the same spatial pattern. At a larger resolution, seen in Figure 26, the spatial pattern of the correlation coefficients between S-1 SM and GLDAS SM data fluctuate between values of about 0.4 and -0.4 (for exact values see Appendix Table 7) in an evident spatial pattern regardless of the epoch.

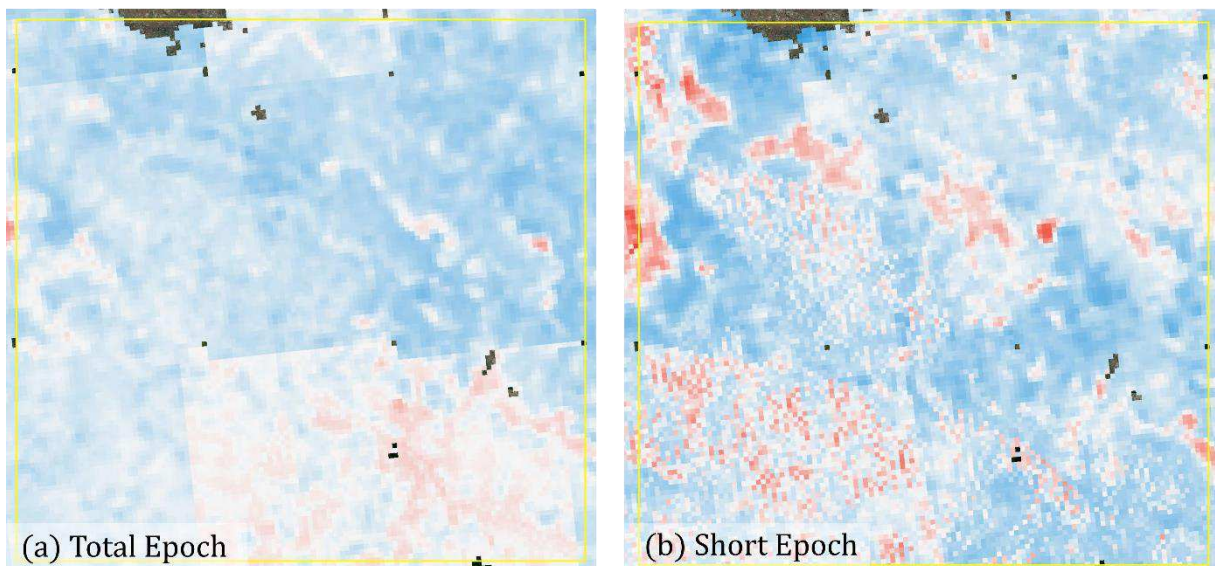


Figure 27: Northern area of interest, as seen in Figure 20, spatial distribution of correlation coefficients between GLDAS SM and S-1 SM datasets over two different temporal epochs.

As seen in Figure 27, a larger scale of the northern area of interest reveals a more varying spatial pattern between the ‘total’ and the ‘short’ epoch; however, both epochs show an overall positive correlation trend. The mean correlation coefficient value for the ‘total’ and ‘short’ epoch is 0.08 and



0.09 respectively (Appendix Table 7). Again, the ‘total’ epoch, seen in Figure 27 (a), has a smoother appearance. Contrary to the southern area of interest depicted in Figure 26, the northern area of interest shown in Figure 27 does not show the same large-scale correlation coefficient spatial patterns between both epochs. The correlation coefficients calculated only from data from the summer months of 2015, Figure 27 (b), reveal an area of positive correlation (max. value = 0.42) along with structures with a negative correlation coefficient with a max. value of -0.32. These spatial structures are not seen in Figure 27 (a), ‘total’ epoch. Additionally, the range of correlation coefficients in the ‘total’ epoch is only half of the range in the ‘short’ epoch (see Appendix Table 7).

Through a spatial analysis of the correlation between the S-1 SM dataset and the GLDAS SM dataset distinct patterns are seen. While the S-1 SM information agrees with the GLDAS model data in some areas, others don’t agree at all. To investigate the origin of these patterns, the spatial distribution maps of the spearman’s rank correlation coefficient between both soil moisture datasets are compared with visual imagery data, landcover data and soil and lithology data.

#### 6.2.1. Comparison with Google Satellite images

In Figure 28 below Spearman’s rank correlation coefficients of the ‘short’ epoch were plotted over the Google maps satellite imagery (see Appendix Figure 48 for ‘total’ epoch). The positive/negative pattern structures seen in the correlation coefficient plots can now be assigned and compared to visible landcover changes.

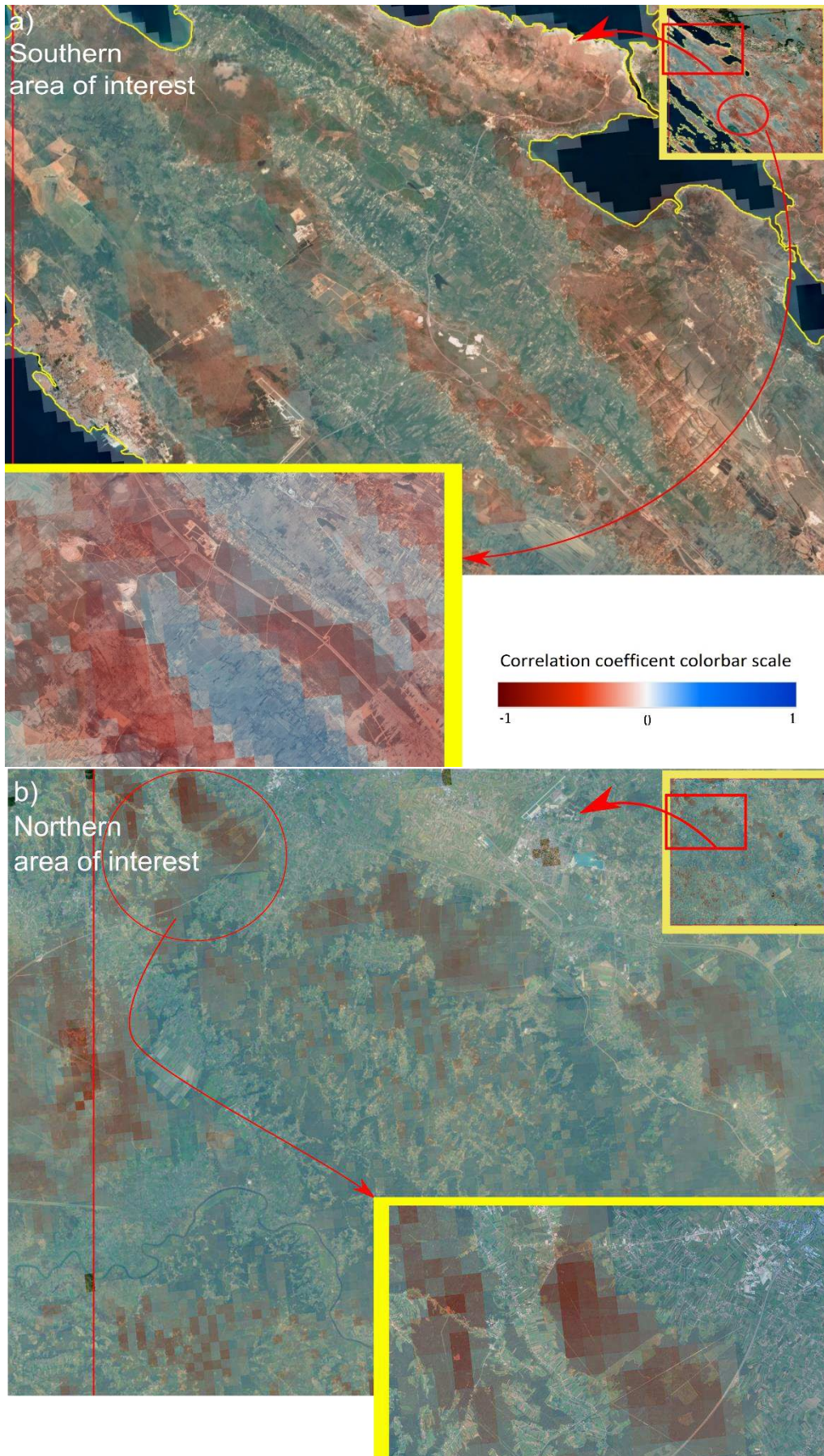


Figure 28: Spatial distribution of correlation coefficients between S-1 and GLDAS SM data for the 'short' epoch superimposed with Google satellite imagery.

In Figure 28 (a) the patterns seen in the spatial distribution map of the correlation coefficients over the summer months of 2015 is reflected in the satellite imagery. The correlation closely follows the visible changes in landcover seen through the satellite imagery. Negative values are seen to be over areas covered with shrub and forest vegetation while cropland landcover yields S-1 SM data like the GLDAS SM model data. Through the satellite imagery it is seen that tree/forest vegetation yield high S-1 SM data in the summer of 2015 while GLDAS reported much lower surface soil moisture values in both the north and south of Croatia. Also, through Figure 28 (a) and (b) cropland maintains a positive correlation coefficient. Figure 28 (a) additionally reveals negative correlation coefficients in the presence of sparse vegetation. In the north, negatively correlated data is only found when tree/forest vegetation is most dense.

### 6.2.2. Comparison with ESA CCI-LC Dataset

To concretize the relationships between landcover type and S-1 to GLDAS correlation coefficients, the correlation coefficient spatial distribution map was also superimposed with ESA's CCI-LC dataset. Figure 29, Figure 30, and Figure 31 show the correlation coefficient patterns for the cropland (rainfed), grassland and tree cover (both >15% and >40% cover) simplified landcover classes described in Figure 9.

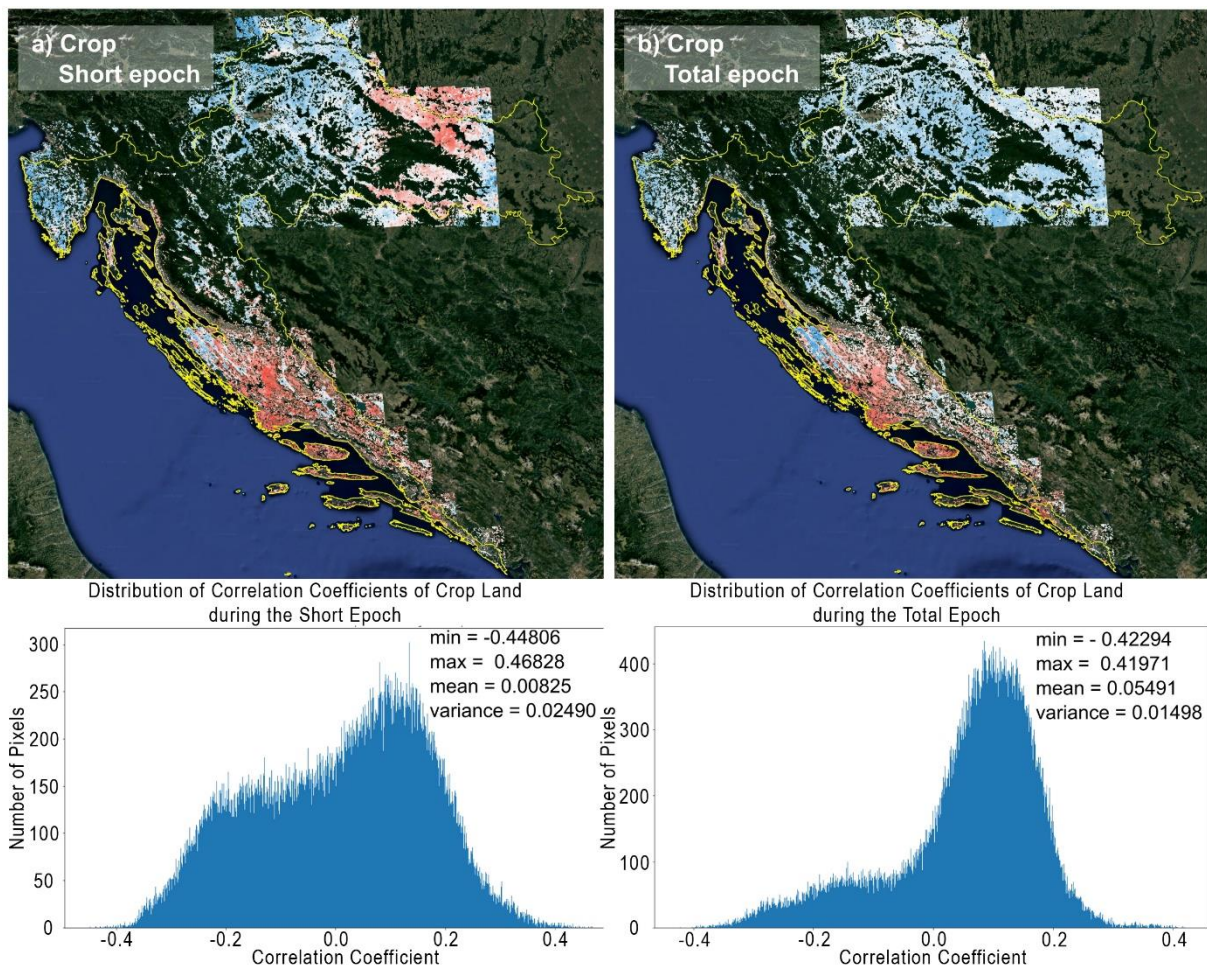


Figure 29: Spearman's rank correlation coefficient for the simplified Cropland (rainfed) CCI-LC class during the (a) short and (b) total epoch. Histogram of coefficient distribution and basic statistics of the dataset.

Spearman's Rank correlation coefficient between S-1 SM and GLDAS SM data is depicted only for the Crop CCI-LC class in Figure 29 above. Through the spatial analysis it is seen that Cropland shows strong positive and negative correlations in both time series. Correlation distributions seen in the respective histograms vary. The short epoch yields a variance of 0.025 while the variance of the total epoch is only 0.015. For the total time series, Figure 29 (b), the histogram shows a clear positive skewed distribution, which is also seen in the violin plots of Cropland in Figure 32. The majority of correlation coefficients here are positive. For the short time series, Figure 29 (a), the histogram's major peak is also positive; however, only half as large as the peak during the total epoch. Both the histogram in Figure 30(a) and the violin plot in Figure 32 show that the data spread during the short epoch is much more homogeneous.

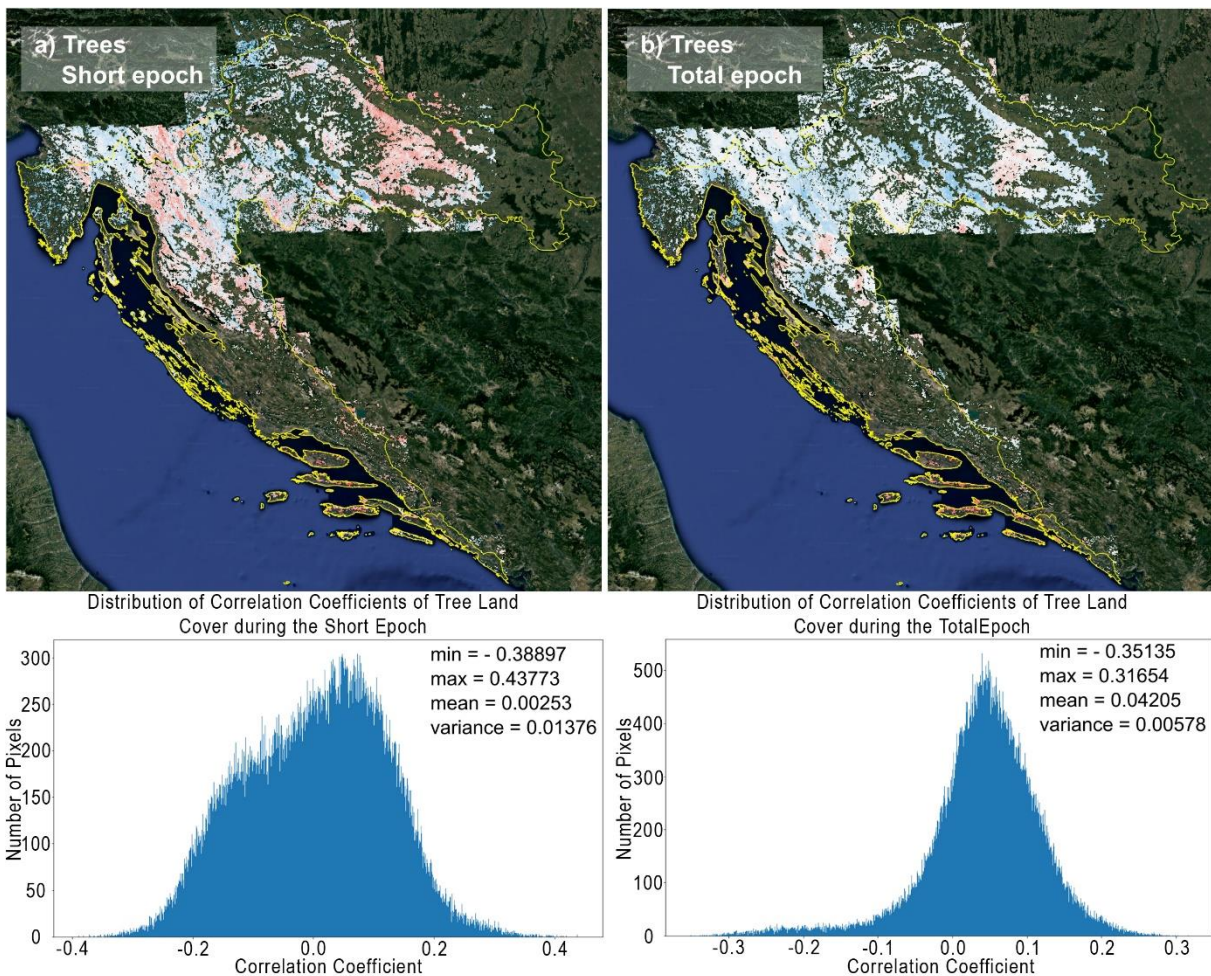


Figure 30: Spearman's rank correlation coefficient for the simplified Trees (>15% and >40% cover) CCI-LC class during the (a) short and (b) total epoch. Histogram of coefficient distribution and basic statistics of the dataset.

Spearman's Rank correlation coefficient between S-1 SM and GLDAS SM data is depicted only for the Trees CCI-LC class in Figure 30. The majority of tree landcover is in the north of Croatia. A positive skewness in the correlation distribution histogram in Figure 30 (b) as well as the violin plot in Figure 32 is seen. Also, the mean correlation coefficient over the total time series is 0.04 while that of the short epoch is only 0.0025. Even through the short epoch the mean correlation is not negative; therefore, tree landcover is not affected by the phenomena described in this investigation. Again, a much larger variance and a more indefinite peak is seen in the short epoch. The same region which yields negative

crop landcover correlation coefficients (Figure 29 (a)) also shows negative correlation coefficients over tree landcover (Figure 30 (b)).

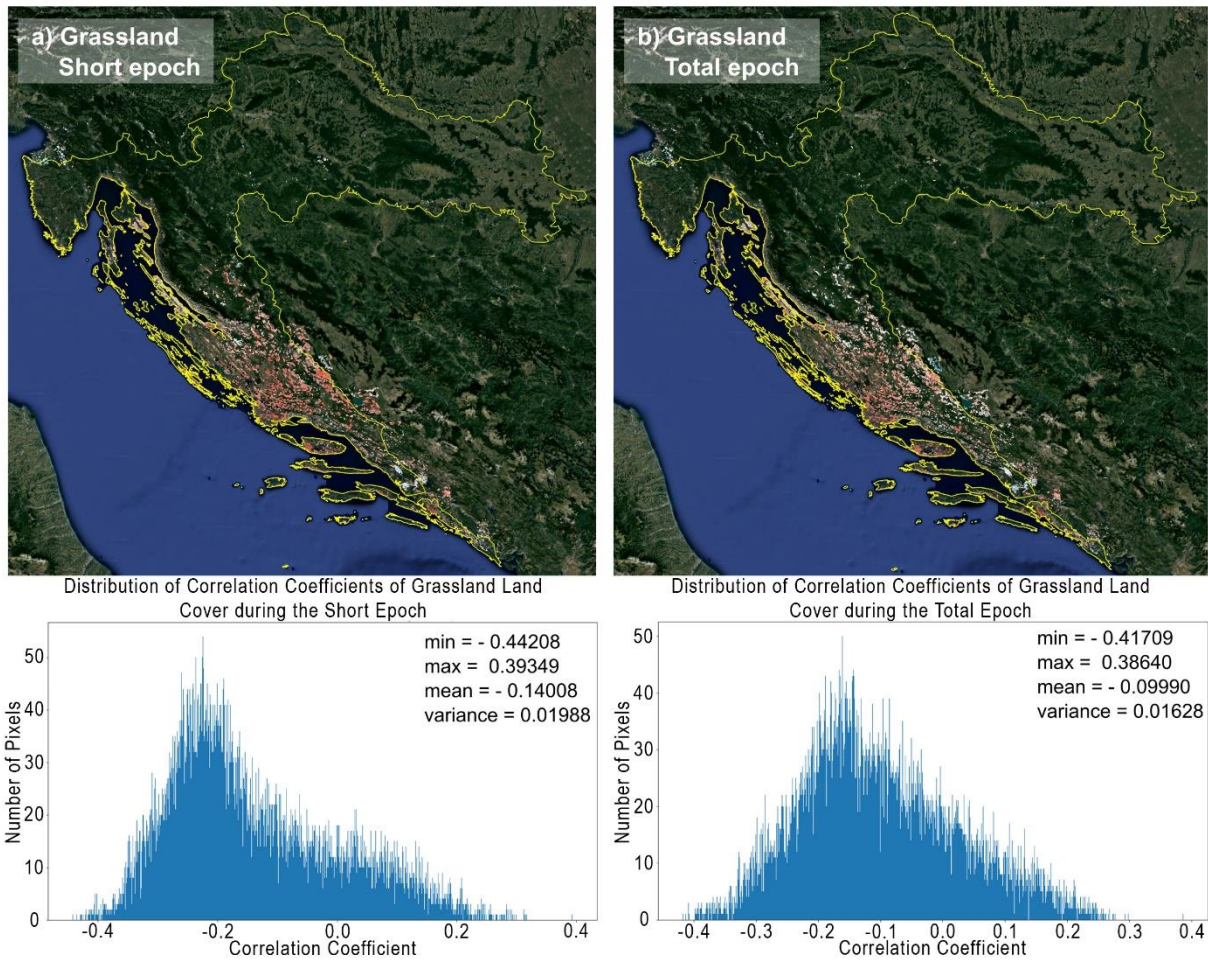


Figure 31: Spearman's rank correlation coefficient for the simplified Grassland CCI-LC class during the (a) short and (b) total epoch. Histogram of coefficient distribution and basic statistics of the dataset.

Spearman's Rank correlation coefficient between S-1 SM and GLDAS SM data is depicted only for the Grassland CCI-LC class in Figure 31. The majority of grassland landcover is found in the south of Croatia. Through Figure 31 and the corresponding violin plots in Figure 32 it is seen that, unlike the other landcover types, both epochs yield a negative skewed correlation distribution. This landcover experiences the least difference between the correlation of a short or long period of time. Both epochs have the same data spread, both correlation distributions have a variance of 0.02, and similar negative mean values. Through Figure 31 it is clear that grassland landcover is affected by the phenomena described in this investigation.

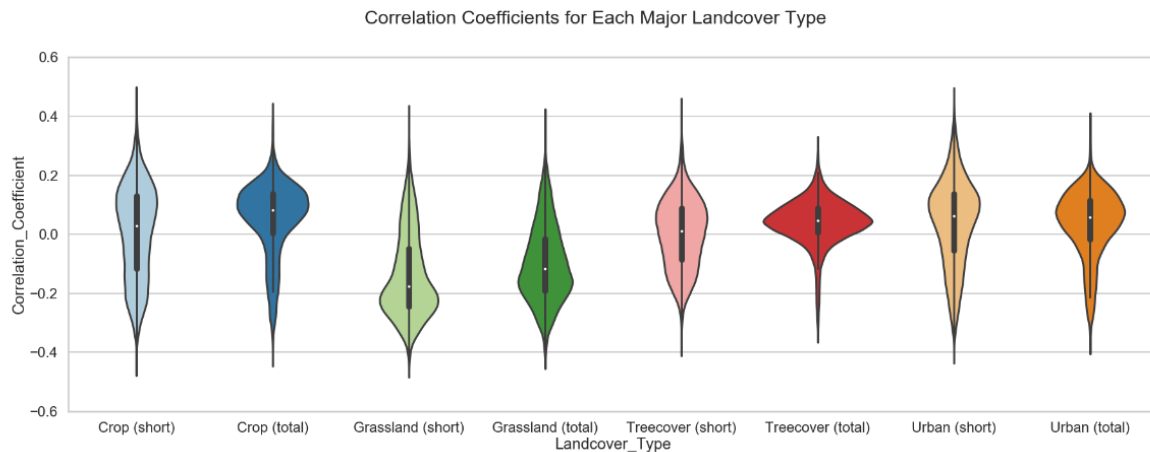


Figure 32: Violin plots of the S-1 SM to GLDAS SM correlation coefficients of the cropland, grassland, tree cover and urban ESA CCI landcover for the 'short' and 'total' epoch.

While the trees and grassland landcover reveal clear trends for the respective landcover type, land covered with cropland yields both strong positive and negative correlation coefficients. In Figure 29 it is seen that although only one landcover type is investigated, the spatial positive – negative correlation pattern is still clearly seen in the southern region of Croatia. Therefore, this the reason for this pattern in the correlation coefficients is not the type vegetation covering the surface. In this case the human visual interpretation of the photogrammetric dataset may be a better tool to determine the coincidence between the correlation coefficient data and the landcover type. Additionally, a look at other factors affecting the backscatter characteristics of a surface such as the type of soil or lithology of the surface may result more clarity.

### 6.2.3. Comparison with Soil Grids Dataset

Croatia's land surface becomes very dry when it does not rain for an extended period of time. This dryness arises from the landcover types and soil types of which Croatia's land is comprised of. To examine if soil type truly has an effect on the high perceived soil moisture satellite response witnessed during extremely dry weather epochs, the spatial correlations between the GLDAS soil moisture information and the S-1 SM was layered over the TAXNWRB Soil Grids data set for Croatia.

In Figure 33, spearman's rank correlation coefficient between S-1 SM and GLDAS SM data is depicted only for the Cambisols TAXNWRB soil type class. The majority of Croatia's soil is Cambisol soil. Through Figure 33 it seen that both epochs yield a neutral correlation distribution histogram over Cambisol soil type. This soil type experiences the least difference between the correlation of a short or long period of time. The correlation coefficients between the S-1 SM and GLDAS SM data do not show a dependency on this soil type.

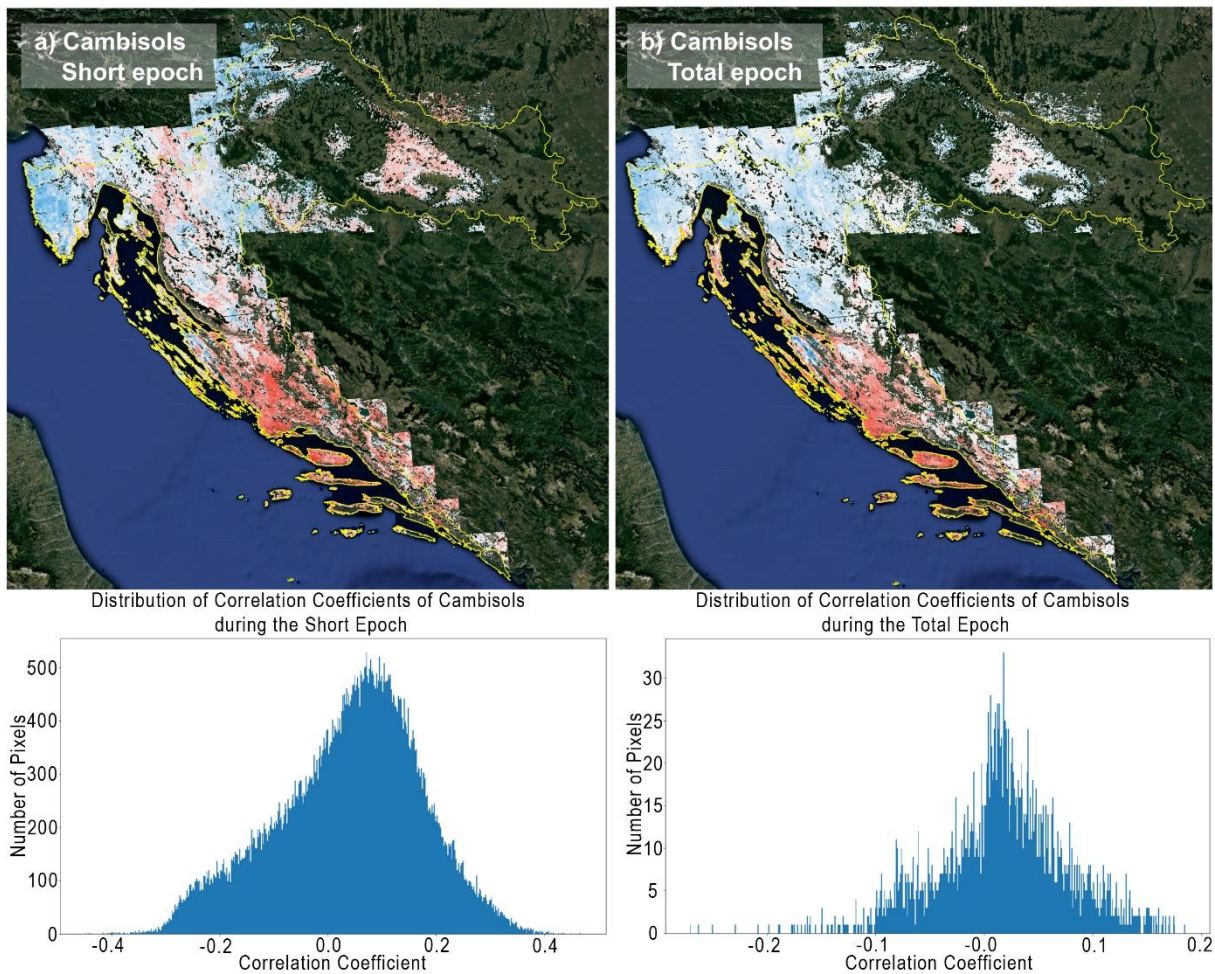


Figure 33: Spearman's rank correlation coefficient for the Cambisols TAXNWRB soil type class during the (a) short and (b) total epoch. Histogram of coefficient distribution.

Unlike the Cambisol soil type seen in Figure 33, the correlation coefficients show a strong dependency on Luvisols, found in the continental north of Croatia, as seen in Figure 34. When depicting Spearman's rank correlation coefficient between S-1 SM and GLDAS SM data only for the Luvisols TAXNWRB soil type class a positive correlation tendency is shown. This positive dependency is also clearly depicted in the violin plots for Luvisols soils in Figure 35. Through Figure 34 (a) and the violin plots in Figure 35 it is seen that in the dry summer months of 2015 an area of Luvisol soil experiences negative correlation coefficients; however, when perceiving correlation over the total epoch, Figure 34 (b), a clear positive correlation crystallizes.

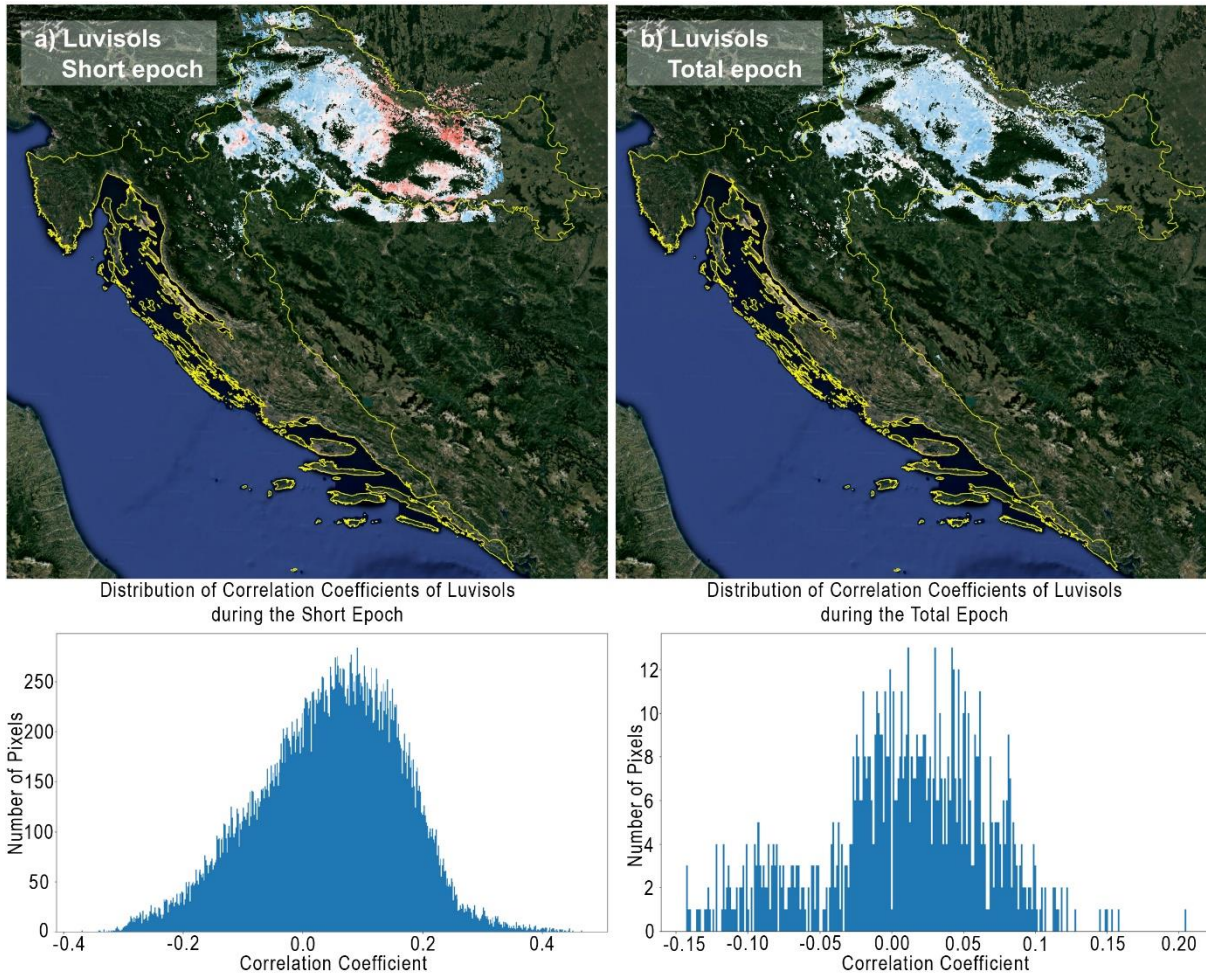


Figure 34: Spearman's rank correlation coefficient for the Luvisols TAXNWRB soil type class during the (a) short and (b) total epoch. Histogram of coefficient distribution.

Through the violin plots in Figure 35 it is possible to easily compare the correlation coefficient trends of all investigated soil types. Fluvisols, Gleysols and Luvisols are all soil types that are associated with water. Fluvisols typically hold water well and are found in regions of water bodies (Table 3). Gleysols are mainly found over high groundwater tables and Luvisols have a very shallow loamy horizon around which there is a high base saturation (Table 3). These three soil types also show clear positive correlation coefficient tendencies with almost no negative correlation values during the total epoch in Figure 35. On the other hand, Acrisols and Leptosols also share similar violin plot forms. Acrisols have a low base saturation while Leptosols are shallow soils over hard rock or highly calcareous material (see appendix Table 6). Cambisols are the most common soil type in Croatia, and also has the most ambiguous description. The S-1 SM to GLDAS SM correlation coefficients calculated over this soil type relies on other surface characteristics than soil type. A look at the near surface lithology of Croatia may explain the backscatter characteristics seen through the correlation coefficients more precisely.



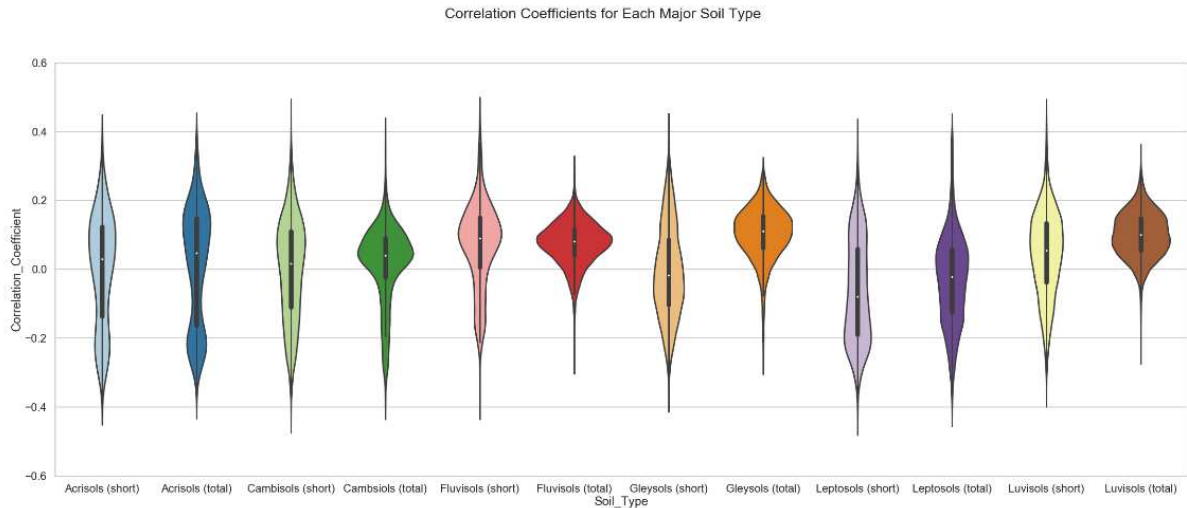


Figure 35: Violin plots of the S-1 SM to GLDAS SM correlation coefficients of the Acrisols, Cambisols, Fluvisols, Gleysols, Leptosols and Luvisols SoilGrids soil types for the 'short' and 'total' epoch.

#### 6.2.4. Comparison with Lithology Dataset

The lithology of an area plays a large role in its backscatter characteristics. Lithological properties define important surface and near subsurface attributes. For example, unconsolidated materials such as gravels and sands have large pores which can be filled with much water; however, this water quickly percolates through the top layers. On the other hand, consolidated materials don't allow any water to pass. Figure 36 shows the S-1 SM to GLDAS SM correlation coefficient trends in the short and total epoch for all consolidated, partly consolidated and unconsolidated surfaces in Croatia. Because the consolidated material more or less only shows positive correlations during the total epoch this surface material seems not to be as affected by the subsurface scattering phenomenon during low soil moisture levels. Nevertheless, when studying the spatial distribution of the correlations, Figure 37, of these lithologies the north/south correlation difference seems to again supersede the spatial lithological patterns seen.

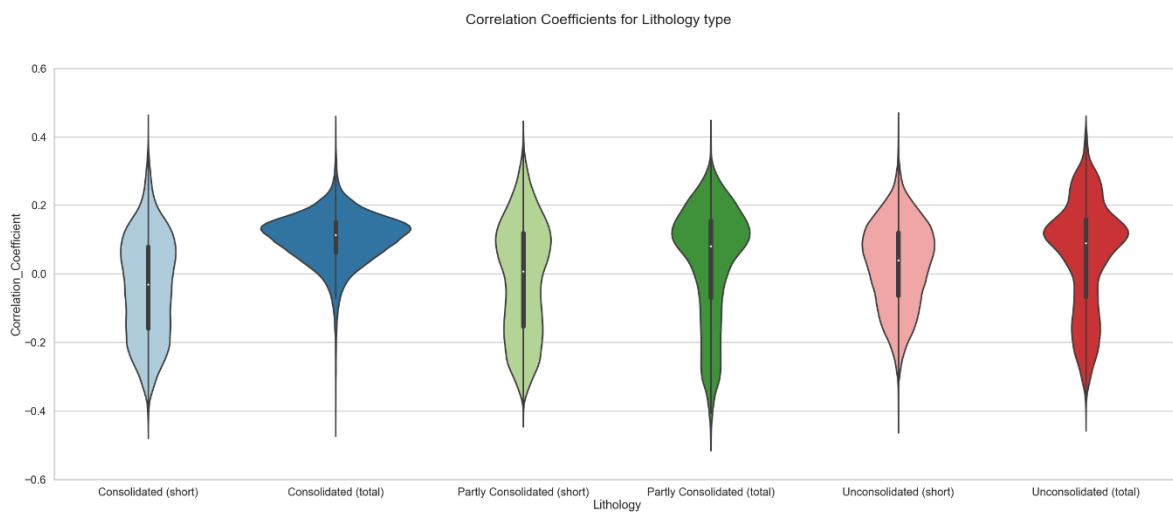


Figure 36: Violin plots of the S-1 SM to GLDAS SM correlation coefficients of the consolidated, partly consolidated and unconsolidated lithology types for the 'short' and 'total' epoch.

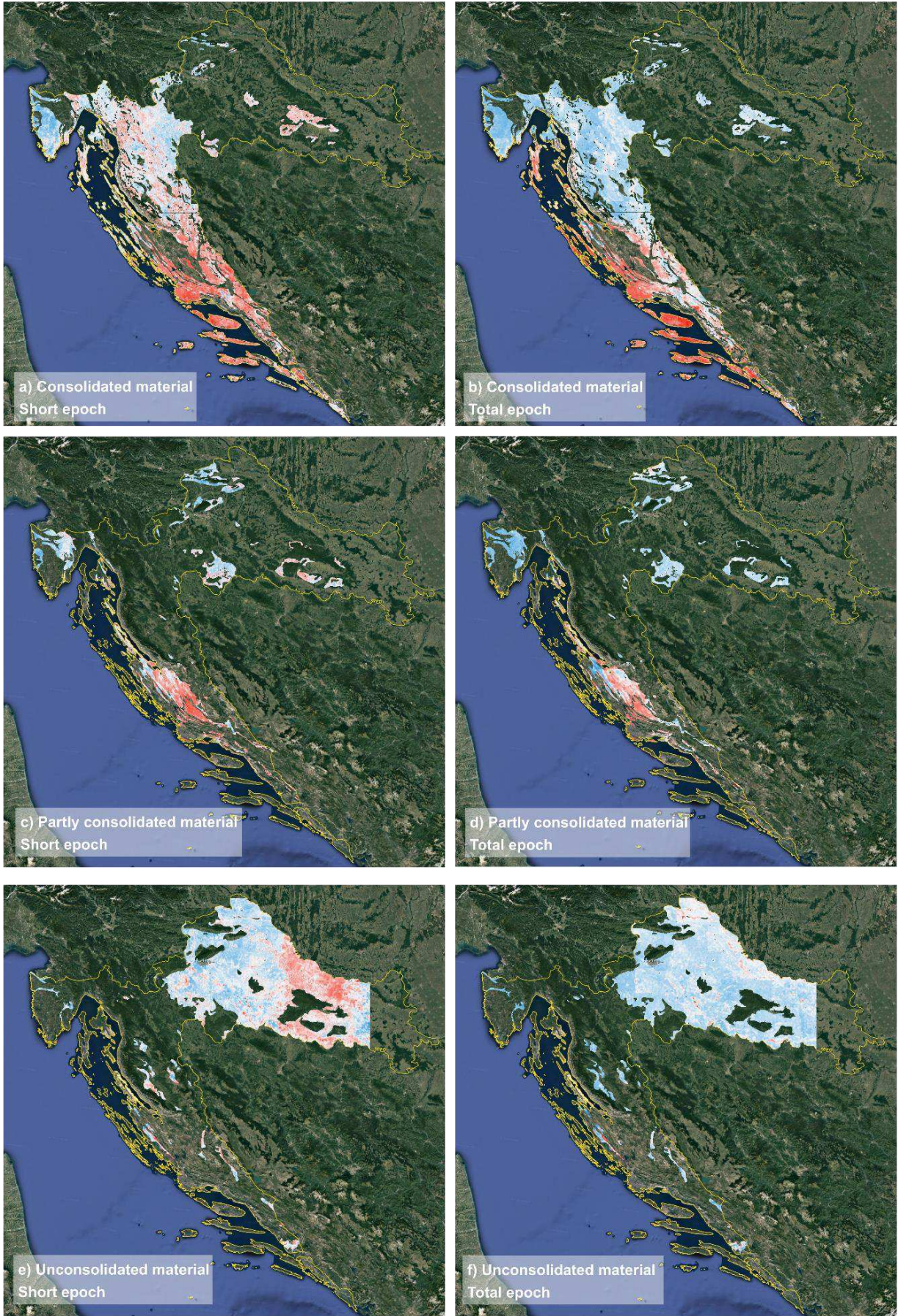


Figure 37: Spearman's rank correlation coefficient for consolidated ((a),(b)), partly consolidated ((c), (d)) and unconsolidated (e), (f)) IHME 1500 lithology during the short and total epoch respectively.

Through Figure 37 it becomes clear that consolidated materials are found along Croatia’s coast while unconsolidated materials are found in the north east of the Country. When taking a closer look at the north east of Croatia, Figure 38, a pattern within the correlation coefficients of the unconsolidated material during the short epoch arises.

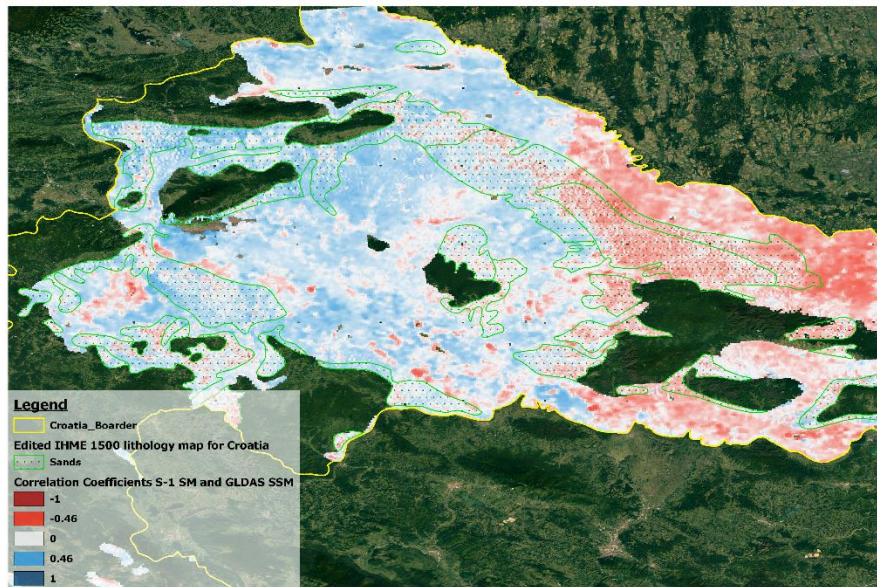


Figure 38: Spatial distribution of the spearman's rank correlation coefficients of unconsolidated IHME 1500 lithology during the 'short' epoch compared to the spatial distribution of sands according to the IHME 1500 lithology map.

Figure 38 reveals the affect sands have on the correlation coefficient – an increase in a ‘speckling’ of the correlation data. On the other hand, Figure 39 shows that the lithological distribution of sandstones and clays versus marlstones and sands in the coastal area of Croatia trace a clear spatial pattern in the correlation coefficients. Nevertheless, it becomes clear that one single land surface characteristic does not determine the cause of the sub surface scattering phenomenon during low SM phases.

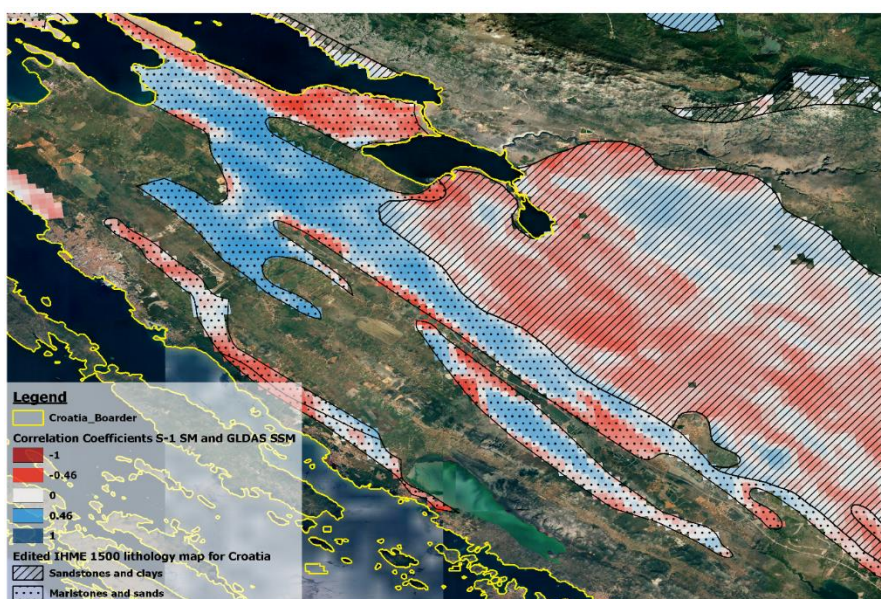


Figure 39: Spatial distribution of the spearman's rank correlation coefficients of partly consolidated IHME 1500 lithology during the 'total' epoch compared to the spatial distribution of sandstones and clays as well as marlstones and sands according to the IHME 1500 lithology map.

## 7. Discussion

### 7.1. Temporal Analysis

The results of the temporal analysis clearly show subsurface backscattering during dry spells in summer months in Croatia. For example, in Figure 22, point 1, the Total epoch temporal analysis shows a clear divergence between the two soil moisture datasets from mid-March 2015 to the end of September 2015. In this time, it only rained once; however, only a negligibly small amount of 0.35 mm/h precipitation was recorded. At the start of October 2015, when it begins to rain more often, both soil moisture datasets meet and match. Nevertheless, the total correlation coefficient at this point is positive. As seen in Figure 18, point 1 lies in the north-west of Croatia, relatively close to the coast. Here, the CLC dataset reports rainfed cropland landcover and through the soil grids dataset it is seen that haplic Cambisol soils prevail at this point. Cambisols are the most common soil type on continental land. These soils do not explain the uncommon surface soil moisture phenomena we see in Croatia during dry spells because they occur in all environments and under all kinds of vegetation; therefore, it can be assumed that the changes seen arise from the landcover differences rather than the soil type. Cropland landcover especially in the southern region of Croatia, on the other hand, is very susceptible to this volume scattering phenomena in summer months. During the summer, most cropped land is already bare as farmers harvest most crops in the late spring/early summer. The soil from the bare cropland is exposed and can dry out more quickly than land covered by vegetation, favoring the volume scattering phenomena to take place.

As seen in Figure 18, point 4 lies in the south west of Croatia, close to the coast. As seen in Figure 22 and Figure 23, this region of Croatia is very dry, the highest amount of rainfall between 2015 and 2017 is less than 4 mm/h and each summer is marked with a long dry spell where no rain whatsoever is recorded. Here the two soil moisture datasets don't only diverge in the summer of 2015, like point 1, but also show a strong negative correlation between the months of July and October 2016 as well as June and September 2017. While GLDAS SM levels drop to below 20% in the summer of 2016, Sentinel-1 data a record surface soil moisture of up to 43%. In the summer of 2017, GLDAS and Sentinel-1 soil moisture differ up to 35% from one another.

### 7.2. Spatial Analysis

Through a spatial analysis and comparison of the Spearman's rank correlation coefficients between the S-1 SM and the GLDAS SM datasets in Croatia with the landcover, soil type and lithology of the country some analogies can be drawn. The most dominant, large scale, spatial pattern observed throughout all datasets is the north – south divide. Precipitation volume, landcover and lithology are all interconnected with one other.

In the north, forest and cropland are the dominant landcover types. Gravel and sand lithology as well as Gleysol, Fluvisol and Luvisol soils are unique to the eastern inland region of the north in Croatia. These soils are characterized for having a higher base saturation, shallow groundwater tables and usually occur in riverbeds floodplains. These land surface characteristics are seen only in this region of the county. That being said, it is no surprise that the negative correlation coefficient phenomenon isn't seen extensively here. In the north, an exception is seen over crop landcover growing on Luvisol soil depicted in Figure 40. Here, negative correlation coefficients arose in the summer months of 2015. Through crop landcover the Luvisol soil is more exposed to drying processes. If the Luvisol soil becomes

dry enough, the C-band microwaves may travel through this layer of soil and reflect off of the underlying gravel. As seen in Figure 25, GLDAS SM levels neither in the north east (Figure 38) nor in the central coastal region (Figure 39) exceeded 25% during the summer of 2015; therefore, perhaps SM values must reach below a threshold of 25% before negative correlations can take place.

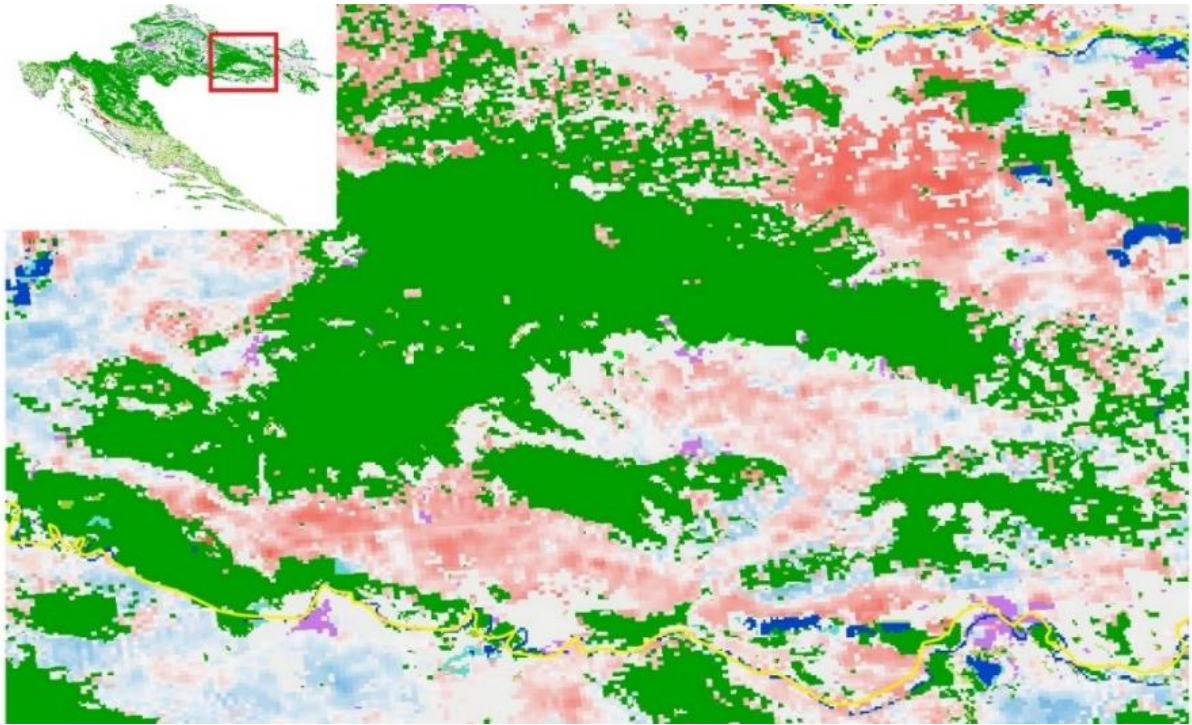


Figure 40: correlation coefficient between S-1 SM and GLDAS SM dataset for Luvisol soil during the short epoch compared to CLC data to show negative correlations over cropland grown on Luvisol soil.

Higher, denser vegetation such as tree landcover doesn't allow for the phenomena investigated in this paper to arise. Due to a layer of denser vegetation shielding the soil from direct sunlight and wind, the soil is not as exposed to loss of moisture. Additionally, a higher volume of organic material such as roots in the soil hold soil moisture in place. One exception is depicted in Figure 41 which shows a negative correlation coefficient trend over tree landcover grown on Cambisol soil with a consolidated lithology. Fluvisols, Gleysols and Luvisols typically hold more water than Cambisols. The combination of Cambisol soil over consolidated lithology may be the cause for the negative correlation between S-1 SM and GLDAS SM data.

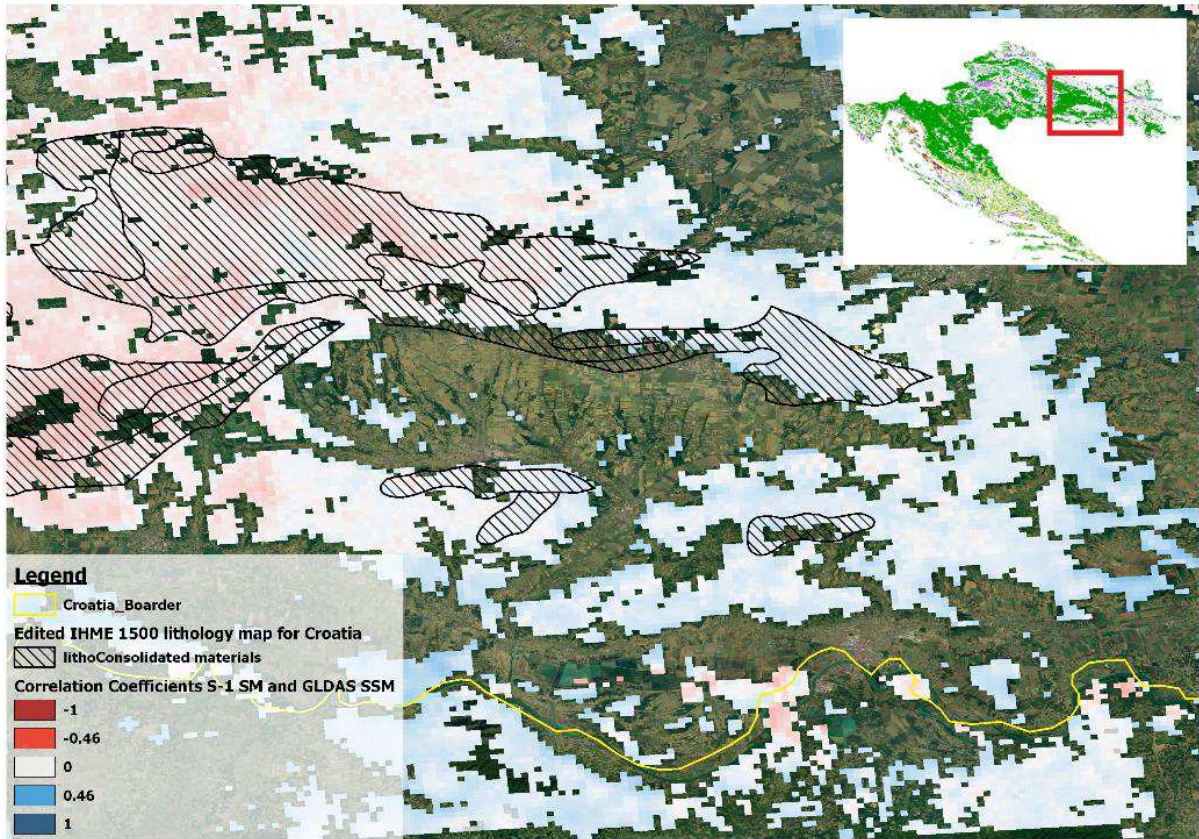


Figure 41: Correlation coefficient between S-1 SM and GLDAS SM dataset for tree landcover grown on Cambisol soil during the total epoch compared to lithology data to show negative correlations over tree landcover when grown on consolidated materials.

In the rest of Croatia, as shown in Figure 42, cropland and grassland are the dominant landcover types. The earth's surface is comprised of Cambisol soils over underlying consolidated lithology. That being said, it is no surprise that the negative correlation coefficient phenomena is seen here. In Figure 41 the negative correlation coefficient patterns during this constellation of Cambisol soil and consolidated material lithology in the wetter northern region of the county has already been seen. Through the drier climate in the south, this pattern can also be seen (Figure 42); however, through other factors such as bedrock depth or surface topography, which have not investigated within this study, the pattern is more ambiguous. This ambiguity is also seen in Figure 33.

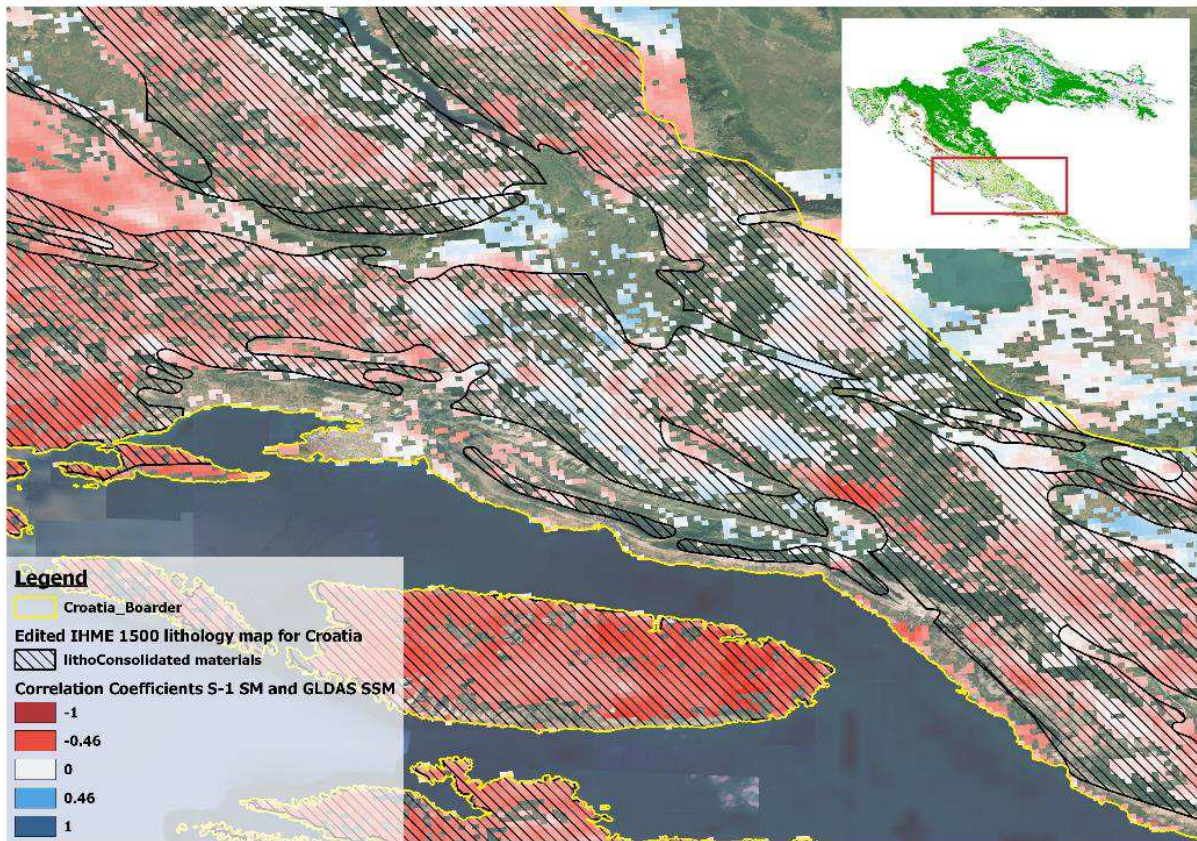


Figure 42: Correlation coefficient between S-1 SM and GLDAS SM dataset for Cambisol soil during the total epoch compared to lithology data to show varying correlation patterns of Cambisol soil on consolidated materials

Grassland is predominantly seen in the south of Croatia. Here, the land surface is very exposed due to the sparse vegetation. Additionally, the vegetation present is also very subject to aridity (Figure 14), making the susceptibility to drought in this region very clear.

During this investigation it has become clear is that there must be a threshold soil moisture value (depicted in Figure 43) after which the usual positive correlation between backscatter and soil moisture takes place. When soil moisture drops below this threshold value backscatter will tend to increase as the soil will act as a volume scatterer and subsurface lithological layers will act as the reflecting surface.

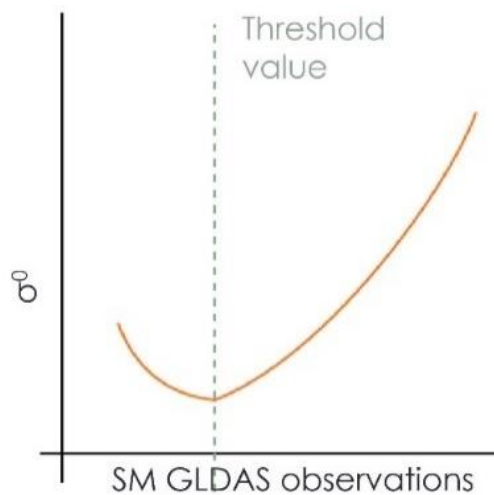


Figure 43: Theoretical threshold soil moisture value at which C-band backscatter and GLDAS SM observations reach familiar positive correlation.

In an effort to reconstruct the theoretical plot in Figure 43 scatter plots of the correlation coefficients between Sentinel-1 SM and GLDAS SM of the ESA CCI landcover, SoilGrids soil types and lithology data against median GLDAS SM values over both the 'short' and the 'total' epoch (all plots found in Appendix Figure 49 – Figure 51). In Figure 44 it is seen that especially the correlation coefficients of grassland landcover roughly follow this theoretical pattern. The highest negative correlations are seen during GLDAS SM values between 22.5% and 25%. Lower SM values witness fewer negative correlations – sub-surface scattering takes place. GLDAS SM values of more than 25% witness increasing correlation coefficients.

**Short epoch: Scatter plot of the correlation coefficients between Sentinel-1 SM and GLDAS SM of ESA CCI landcover types against median GLDAS SM values**

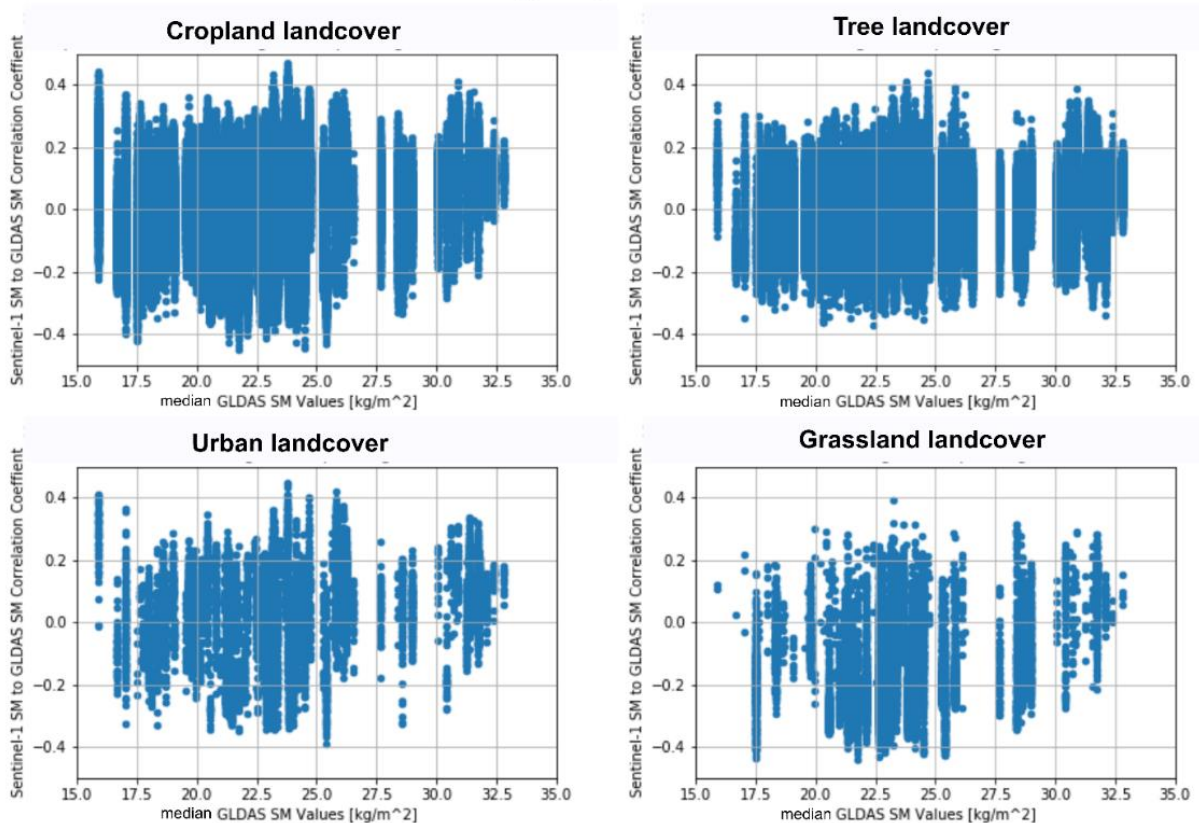


Figure 44: Scatterplot of correlation coefficients between Sentinel-1 SM and GLDAS SM of Cropland, Tree cover, Urban and Grassland ESA CCI landcover against median GLDAS SM values over the 'short' epoch (see 'total' epoch in Appendix Figure 49)

When plotting the correlation coefficient values of the five major soil types in Croatia over median GLDAS SM values over the summer of 2015 Cambisols and Gleysols allude to a threshold SM value. Over Cambisol soils, most negative correlations are seen between 22 – 25% median GLDAS SM. On the other hand, Gleysols show this minimum correlation value already at 17.5 – 20% median GLDAS SM. This difference in threshold values could explain why, for example, both positive and negative correlation coefficient values are seen over grassland landcover. Grassland could witness sub-surface backscatter below SM values of 22.5%; however, depending on which soil type the grassland lays this threshold value will shift.



**Short epoch:  
Scatter plot of the correlation  
coefficients between Sentinel-1  
SM and GLDAS SM of  
Soil Grids soil types against  
median GLDAS SM values**

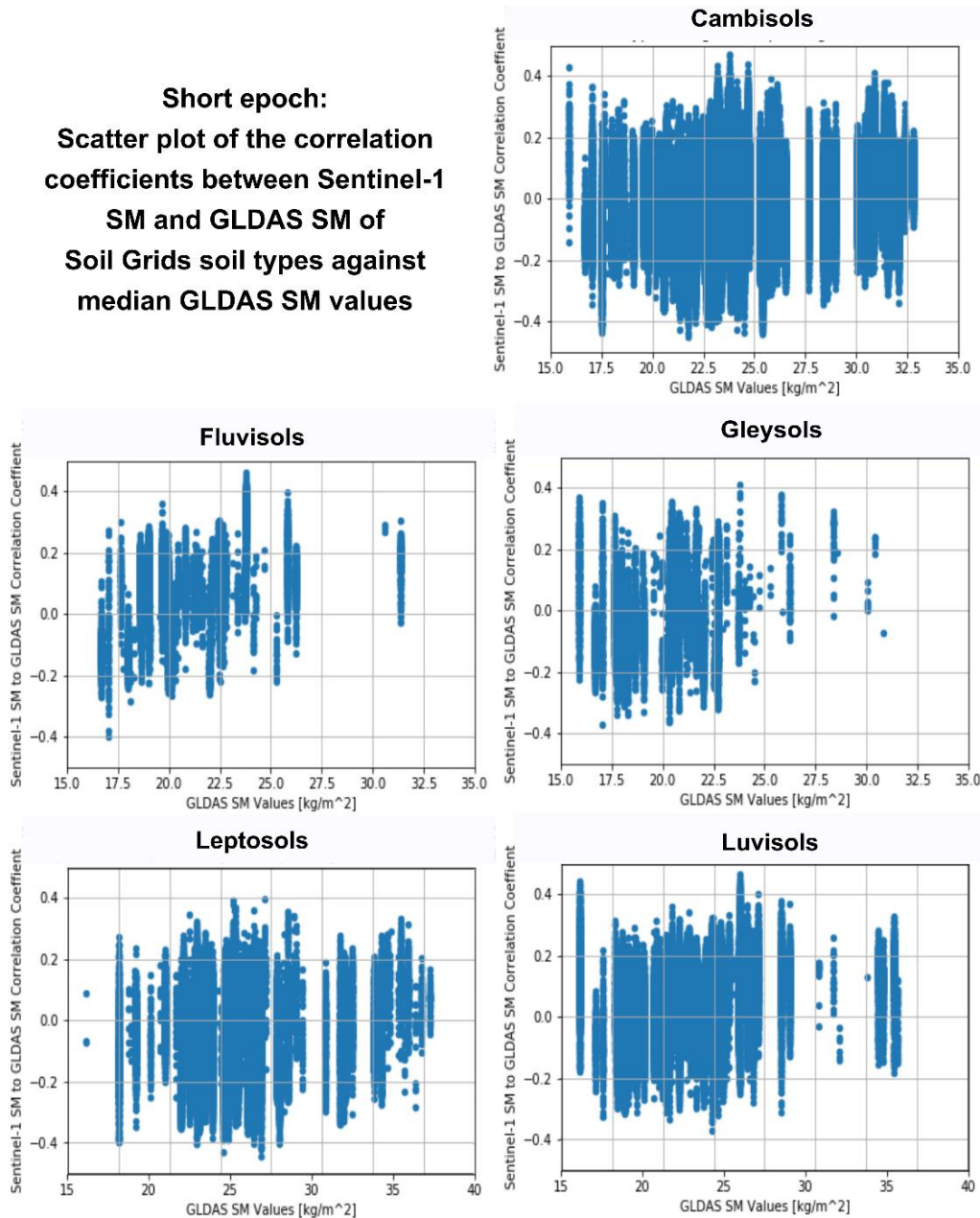


Figure 45: Scatterplot of correlation coefficients between Sentinel-1 SM and GLDAS SM of Cambisols, Fluvisols, Gleysols, Leptosols and Luvisols against median GLDAS SM values over the 'short' epoch (see 'total' epoch in Appendix Figure 50).

Both Figure 41 and Figure 42 show that the spatial distribution of consolidated lithology somewhat follows the spatial patterns seen in the correlation coefficients; however, they are seen to vary between either positive or negative correlation coefficient values. These lithologies show clear ambiguous responses which again must be explained through a complex combination of surface factors not explored within this investigation. Terrain relief, for example, is a land surface factor which greatly affects soil moisture. In this investigation soil moisture information on steep terrain was merely exempt from the dataset due to its large error estimation; however, all other data, regardless of terrain relief, was handled uniformly. Valleys and ridges lead to changes in soil composition. For example, at ridges or slopes soil cover is usually much thinner due to geomorphic processes such as downhill creep exposing the underlying bedrock more quickly. Additionally, the soil on slopes and ridges will not hold water as long as soil in a basin or valley due to the natural downward flow of water. All of these factors can falsely return high C-band backscatter signals.

## 8. Conclusion – Outlook

The objective of this research was to characterize subsurface scattering effects in C-band backscatter data over Croatia. After providing a theoretical background on subsurface scattering, this research addressed two research questions. 1) What are the spatial and temporal characteristics of subsurface scattering? 2) Which physical processes are driving subsurface scattering in Croatia?

This study has provided insight into Sentinel-1 surface soil moisture and GLDAS soil moisture discrepancies during dry months in Croatia. During a time when model soil moisture levels are at their lowest, especially the central and southern coastal region of Croatia exhibits high Sentinel-1 SM data values. This divergence between model data and remotely sensed data was presented with spearman's rank correlation coefficient values for every Sentinel-1 pixel. A temporal and spatial analysis established both when and where this phenomenon occurs in the study area of Croatia. Through spatial comparisons of the correlation coefficient values with ESA's CCI landcover dataset, SoilGrids soil type data and the International Hydrogeological Map of Europe lithology information it has become clear that not one single surface characteristic is accountable for its soil moisture or rather its backscatter characteristics. What has become clear is that there must be a threshold soil moisture value (depicted in Figure 43) after which the usual positive correlation between backscatter and soil moisture takes place. When soil moisture drops below this threshold value backscatter will tend to increase as the soil will act as a volume scatterer and subsurface lithological layers will act as the reflecting surface. Where this soil moisture threshold value lays requires further investigation.

To further investigate the discrepancy witnessed between S-1 SM and GLDAS SM data in Croatia, especially in the summer months, it would be necessary to take in situ measurements. Perhaps a small region in Croatia can be investigated more extensively through the use of other geodetic methods such as electromagnetic subsurface profile measurements. Soil core samples should also be taken to verify soil type and lithology data. Once the reference data has been verified and adjusted with in situ measurements, perhaps a more unambiguous correlation between S-1 SM phenomena and surface properties can be made.

As a result of the recognition of this discrepancy between S-1 SM and GLDAS SM data in some regions of the world, and the underlying cause of this discrepancy new evidence of a changing climate can be brought to light. Through the examination of a larger time series into the past, yearly spatial correlation coefficient maps can be created to possibly illustrate phenomena such as the progression of the desertification of Europe. Extrapolating the data, a diagnosis of future Europe can be made if industry, economy and politics do not change.

## 9. Bibliography

Beaudoin, H. and M. Rodell, NASA/GSFC/HSL, 2015. "GLDAS Noah Land Surface Model L4 3 hourly 0.25 x 0.25 degree V2.0". Greenbelt, Maryland, USA, Goddard Earth Sciences Data and Information Services Center (GES DISC). Accessed: 13.04.2019, 10.5067/342OHQM9AK6Q

Cleland, Elsa E, et al. "Shifting Plant Phenology in Response to Global Change". *Trends in Ecology & Evolution*, vol. 22, no. 7, July 2007, pp. 357–365., doi:10.1016/j.tree.2007.04.003

"Drought Impact Report" Global Drought Observatory - JRC European Commission [WWW Document], n.d. URL

<https://edo.jrc.ec.europa.eu/gdo/php/index.php?id=2022&ndx=RDrl&scope=famine&lon=17.10967&lat=46.08572&refDate=2015-08-11> (accessed 11.2.19).

EEA, 2017. "Trends in summer soil moisture in Europe". European Environment Agency, European Environment Information and Observation Network (Eionet), 26 July 2017, <https://www.eea.europa.eu/data-and-maps/figures/changes-in-summer-soil-moisture>.

EDO, 2015. "Drought News August 2015". European Drought Observatory (EDO). August 2015. URL <http://edo.jrc.ec.europa.eu>

Hengl T, Mendes de Jesus J, Heuvelink GBM, Ruiperez Gonzalez M, Kilibarda M, Blagotić A, et al., 2017. "SoilGrids250m: Global gridded soil information based on machine learning". *PLoS ONE* 12(2): e0169748. <https://doi.org/10.1371/journal.pone.0169748>

Kosztra, B. et al, 2017. "Updated CLC Illustrated Nomenclature Guidelines". Copernicus, 2017, [land.copernicus.eu/user-corner/technical-library/corine-land-cover-nomenclature-guidelines/html/](http://land.copernicus.eu/user-corner/technical-library/corine-land-cover-nomenclature-guidelines/html/).

Lovrić, M., Lovrić, N, 2013. "Integration of Nature Protection in Forest Policy in Croatia".

Mätzler, C., 1998. "Microwave permittivity of dry sand". *IEEE Transactions on Geoscience and Remote Sensing*. 36 (1), 317–319. <https://doi.org/10.1109/36.655342>

McKnight, Tom L., Hess, Darrel, 2000. "Climate Zones and Types". *Physical Geography: A Landscape Appreciation*. Upper Saddle River, NJ: Prentice Hall. ISBN 978-0-13-020263-5.

Bishop, M.P., Olsenholler, J.A., Shroder, J.F., Barry, R.G., Raup, B.H., Bush, A.B.G., Copland, L., Dwyer, J.L., Fountain, A.G., Haeberli, W., Käähb, A., Paul, F., Hall, D.K., Kargel, J.S., Molnia, B.F., Trabandt, D.C., Wessels, R., 2004. "Global Land Ice Measurements from Space (GLIMS): Remote Sensing and GIS Investigations of the Earth's Cryosphere". *Geocarto International* 19, 57–84. <https://doi.org/10.1080/10106040408542307>

N. Baghdadi, H. Bazzi, M. El Hajj, M. Zribi, 2018. "Detection of frozen soil using Sentinel-1 SAR data." *Remote Sensing, MDPI*, 10 (8), pp.1182. 10.3390/rs10081182. hal-01899082

IUSS Working Group WRB. 2015. "World Reference Base for Soil Resources 2014, update 2015". International soil classification system for naming soils and creating legends for soil maps. World Soil Resources Reports No. 106. FAO, Rome

Sonia I. Seneviratne et al., 2010. "Investigating Soil Moisture–Climate Interactions in a Changing Climate: A Review". *Elsevier*, vol. 99, no. 3-4, May 2010, pp. 125–161., doi:10.1016/j.earscirev.2010.02.004.

"Sentinel-1: Mission Details". Sentinel-1 - ESA EO Missions - Earth Online - ESA [WWW Document], 2019. URL <https://earth.esa.int/web/guest/missions/esa-operational-eo-missions/sentinel-1> (accessed 11.17.19).

SoilGrids, 2019, ISRIC - World Soil Information [WWW Document]. URL <http://soilgrids.org> (accessed 11.17.19).

TU Wien Department of Geodesy and Geoinformation, 2017. "1 Km Surface Soil Moisture from Sentinel-1". vol. 02, 25 Oct. 2017, Product Documentation: Internal dissemination

Wagner, W., S. Hahn, M. Vreugdenhil et al., 2017. „Sub-Surface Scattering Effects observed by C-Band Radars“. Department of Geodesy and Geoinformation, TU Wien. Lecture Powerpoint Presentation.

Wagner, W., Hahn, S., Kidd, R., Melzer, T., Bartalis, Z., Hasenauer, S., Figa-Saldaña, J., de Rosnay, P., Jann, A., Schneider, S., Komma, J., Kubu, G., Brugger, K., Aubrecht, C., Züger, J., Gangkofner, U., Kienberger, S., Brocca, L., Wang, Y., Blöschl, G., Eitzinger, J., Steinnocher, K., 2013. „The ASCAT Soil Moisture Product: A Review of its Specifications, Validation Results, and Emerging Applications“. Meteorologische Zeitschrift, pp. 5–33. 10.1127/0941-2948/2013/0399.

Woodhouse, Iain H., 2005. Introduction to Microwave Remote Sensing. CRC Press.

## 10. List of Figures

Figure 1: Trends in summer (June to August) soil moisture in Europe between 1951 – 2012. The soil moisture content was modelled using a soil moisture balance model in the upper soil horizons (EEA, 2017).....	3
Figure 2: Soil Texture Triangle (www.nrcs.usda.gov) .....	6
Figure 3: The real (a) and imaginary (b) part of the dielectric constant of a frozen soil-water mixture with 30% vol soil moisture content according to the soil temperature for three soil types (N.Baghdadi, 2018).....	7
Figure 4: The Cloud-Model shown through a SAR radiation surface and volume scattering through a dry soil layer.....	8
Figure 5: Biogeographical regions of Croatia (Lovrić, 2013) .....	9
Figure 6: simplified ESA Climate Change Initiative Landcover distribution in Croatia .....	9
Figure 7: GLDAS model average rainfall over all of Croatia from 01.01.2015 to 31.12.2017. Summer months, from June to October are highlighted with a yellow background. ....	10
Figure 8: Sentinel-1 dual satellite temporal coverage over Croatia (TU Wien Department of Geodesy and Geoinformation, 2017).....	11
Figure 9: CCI – LC Class simplification .....	14
Figure 10: ESA CCI landcover map used for investigation.....	15
Figure 11: Arable parcels separated by stone walls (Malta). Photo: B. Kosztra & Small-parcel arable land (near Vienna, Austria). Photo: Gy. Büttner.....	15
Figure 12: Clearcut pine forest (Hungary) Photo: B. Kosztra & Transition from grasslands to forest by natural succession (due to lack of grazing) in the Carpathians (Romania). Photo: Gy. Büttner .....	16
Figure 13: Mixed forest made up of deciduous forest intermixed with small (<25 ha) stands of coniferous trees (Austria). Photo: Gy. Büttner & Semi-natural coniferous forest in the Carpathian Mountains (Romania) Photo: B. Kosztra.....	16
Figure 14: Low-productivity grassland on karstic surface with scattered shrubs (Hungary). Photo: B. Kosztra & Species-rich natural grassland in nature conservation area (Hungary). Photo: B. Kosztra ..	17
Figure 15: TAXNWRB Soil Grid Data in Croatia .....	18
Figure 16: IHME 1500 aggregation level 3 and level 5 lithology information for Croatia. ....	20
Figure 17: IHME 1500 Seawater intrusion in Croatia. ....	21
Figure 18: Point locations of temporal analysis - time series plots .....	23
Figure 19: Nearest neighbor GLDAS data for S-1 raster information to allow the calculation of correlation coefficients between two datasets with varying spatial resolutions.....	24
Figure 20: Spatial distribution of northern and southern area of interest for spatial analysis.....	25
Figure 21: Colorbar scale used for all correlation coefficients maps during this investigation .....	25
Figure 22: ‘Total’ time epoch of the 5 points to show temporal trends over the entire 3 years (2015-2017) .....	27

Figure 23: ‘Year’, ‘Short’ and ‘Summer’ time epoch of the 5 points to show temporal trends over the year 2017 and the summer of 2015..... 29

Figure 24: Spatial distribution of correlation coefficients between GLDAS SM and S-1 SM datasets over three different temporal epochs. .... 30

Figure 25: Median GLDAS SM values of Croatia over the (a) total, (b) year, and (c) short epoch. .... 31

Figure 26: Southern area of interest, as seen in Figure 20, spatial distribution of correlation coefficients between GLDAS SM and S-1 SM datasets over two different temporal epochs. .... 32

Figure 27: Northern area of interest, as seen in Figure 20, spatial distribution of correlation coefficients between GLDAS SM and S - 1 SM datasets over two different temporal epochs. .... 32

Figure 28: Spatial distribution of correlation coefficients between S-1 and GLDAS SM data for the 'short' epoch superimposed with Google satellite imagery..... 34

Figure 29: Spearman's rank correlation coefficient for the simplified Cropland (rainfed) CCI-LC class during the (a) short and (b) total epoch. Histogram of coefficient distribution and basic statistics of the dataset..... 35

Figure 30: Spearman's rank correlation coefficient for the simplified Trees (>15% and >40% cover) CCI-LC class during the (a) short and (b) total epoch. Histogram of coefficient distribution and basic statistics of the dataset. .... 36

Figure 31: Spearman's rank correlation coefficient for the simplified Grassland CCI-LC class during the (a) short and (b) total epoch. Histogram of coefficient distribution and basic statistics of the dataset. .... 37

Figure 32: Violin plots of the S-1 SM to GLDAS SM correlation coefficients of the cropland, grassland, tree cover and urban ESA CCI landcover for the 'short' and 'total' epoch. .... 38

Figure 33: Spearman's rank correlation coefficient for the Cambisols TAXNWRB soil type class during the (a) short and (b) total epoch. Histogram of coefficient distribution. .... 39

Figure 34: Spearman's rank correlation coefficient for the Luvisols TAXNWRB soil type class during the (a) short and (b) total epoch. Histogram of coefficient distribution. .... 40

Figure 35: Violin plots of the S-1 SM to GLDAS SM correlation coefficients of the Acrisols, Cambisols, Fluvisols, Gleysols, Leptosols and Luvisols SoilGrids soil types for the 'short' and 'total' epoch. .... 41

Figure 36: Violin plots of the S-1 SM to GLDAS SM correlation coefficients of the consolidated, partly consolidated and unconsolidated lithology types for the 'short' and 'total' epoch..... 41

Figure 37: Spearman's rank correlation coefficient for consolidated ((a),(b)), partly consolidated ((c), (d)) and unconsolidated (e), (f)) IHME 1500 lithology during the short and total epoch respectively. .... 42

Figure 38: Spatial distribution of the spearman's rank correlation coefficients of unconsolidated IHME 1500 lithology during the 'short' epoch compared to the spatial distribution of sands according to the IHME 1500 lithology map..... 43

Figure 39: Spatial distribution of the spearman's rank correlation coefficients of partly consolidated IHME 1500 lithology during the ‘total’ epoch compared to the spatial distribution of sandstones and clays as well as marlstones and sands according to the IHME 1500 lithology map. .... 43

Figure 40: correlation coefficient between S-1 SM and GLDAS SM dataset for Luvisol soil during the short epoch compared to CLC data to show negative correlations over cropland grown on Luvisol soil. .... 45

Figure 41: Correlation coefficient between S-1 SM and GLDAS SM dataset for tree landcover grown on Cambisol soil during the total epoch compared to lithology data to show negative correlations over tree landcover when grown on consolidated materials. ....	46
Figure 42: Correlation coefficient between S-1 SM and GLDAS SM dataset for Cambisol soil during the total epoch compared to lithology data to show varying correlation patterns of Cambisol soil on consolidated materials .....	47
Figure 43: Theoretical threshold soil moisture value at which C-band backscatter and GLDAS SM observations reach familiar positive correlation.....	47
Figure 44: Scatterplot of correlation coefficients between Sentinel-1 SM and GLDAS SM of Cropland, Tree cover, Urban and Grassland ESA CCI landcover against median GLDAS SM values over the 'short' epoch (see 'total' epoch in Appendix Figure 49) .....	48
Figure 45: Scatterplot of correlation coefficients between Sentinel-1 SM and GLDAS SM of Cambisols, Fluvisols, Gleysols, Leptosols and Luvisols against median GLDAS SM values over the 'short' epoch (see 'total' epoch in Appendix Figure 50). .....	49
Figure 46: GDO 10-day period maps of risk of drought impact for agriculture in Croatia in the summer of 2015 (Drought Impact Report, n.d) .....	57
Figure 47: GDO 10-day period maps of risk of drought impact for agriculture in Croatia in 2017 (Drought Impact Report, n.d).....	58
Figure 48: Spatial distribution of correlation coefficients between S-1 and GLDAS SM data for the 'total' epoch superimposed with Google satellite imagery.....	62
Figure 49: Scatter plots of the correlation coefficients between S-1 SM and GLDAS SM of the ESA CCI landcover types against the median GLDAS SM values of the 'short' and 'total' epoch respectively ..	63
Figure 50: Scatter plots of the correlation coefficients between S-1 SM and GLDAS SM of the SoilGrids soil types against the median GLDAS SM values of the 'short' and 'total' epoch respectively .....	64
Figure 51: Scatter plots of the correlation coefficients between S-1 SM and GLDAS SM of the lithology types against the median GLDAS SM values of the 'short' and 'total' epoch respectively .....	65
Figure 52: Spearman's rank correlation coefficient for the Gleysols TAXNWRB soil type class during the (a) short and (b) total epoch. Histogram of coefficient distribution and basic statistics of the dataset. ....	66
Figure 53: Spearman's rank correlation coefficient for the Acrisols TAXNWRB soil type class during the (a) short and (b) total epoch. Histogram of coefficient distribution and basic statistics of the dataset. ....	66
Figure 54: Spearman's rank correlation coefficient for the Fluvisols TAXNWRB soil type class during the (a) short and (b) total epoch. Histogram of coefficient distribution and basic statistics of the dataset. ....	67
Figure 55: Spearman's rank correlation coefficient for the Leptosols TAXNWRB soil type class during the (a) short and (b) total epoch. Histogram of coefficient distribution. ....	67

## 11. List of Tables

Table 1: Grain sizes for each soil texture, defined by the USDA .....	6
Table 2: S -1 mission details (Sentinel-1: Mission Details, 2018) .....	11
Table 3: Detailed description of most common soil types in Croatia (IUSS Working Group WRB, 2015). .....	19
Table 4: Used abbreviations for time epochs .....	22
Table 5: Description overview of temporal analysis points of interest. See appendix Table 8 for further average annual rainfall data calculated from the GLDAS rainfall dataset. ....	23
Table 6: Short definitions of TAXNWRB Soil Grids Dataset Soil Types.....	60
Table 7: Correlation coefficient statistics of area of interests ‘north’ and ‘south’ as well as entire Croatia.....	61
Table 8: Annual Rainfall for points of interest defined in Figure 18 calculated from GLDAS ‘Rainf_tavg’ data .....	61



# 12. Appendix

Global Drought Observatory (GDO): Risk of Drought Impact for agriculture in Croatia from July - September 2015

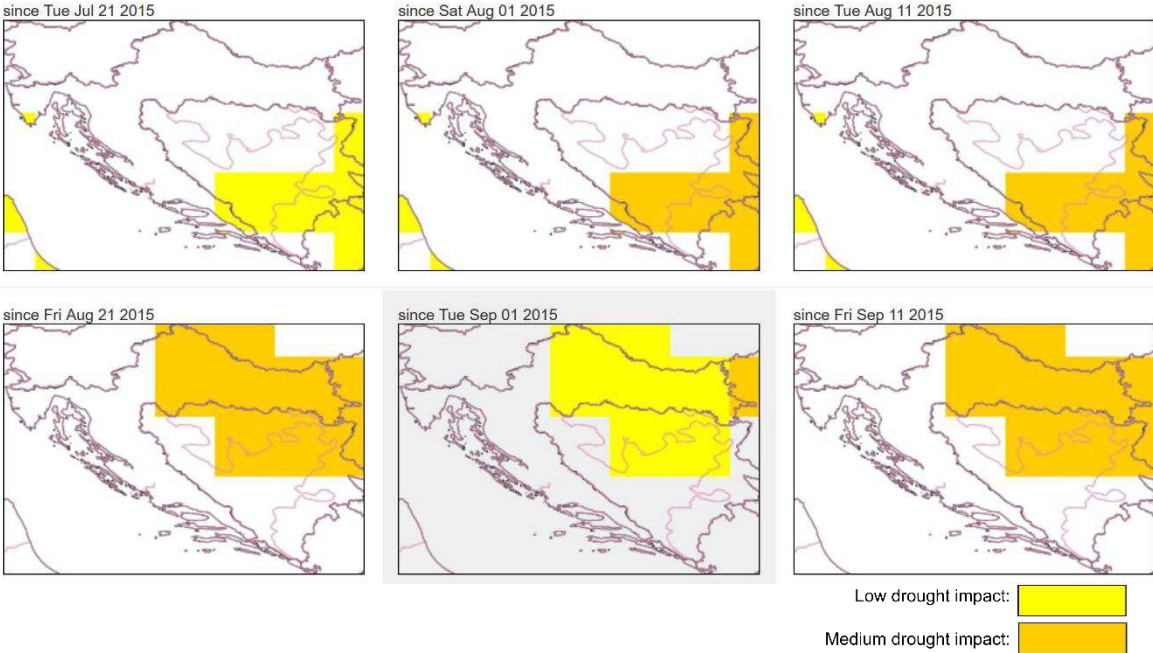


Figure 46: GDO 10-day period maps of risk of drought impact for agriculture in Croatia in the summer of 2015 (Drought Impact Report, n.d)

Die approbierte gedruckte Originalversion dieser Diplomarbeit ist an der TU Wien Bibliothek verfügbar.  
The approved original version of this thesis is available in print at TU Wien Bibliothek.

## Global Drought Observatory (GDO): Risk of Drought Impact for agriculture in Croatia in 2017

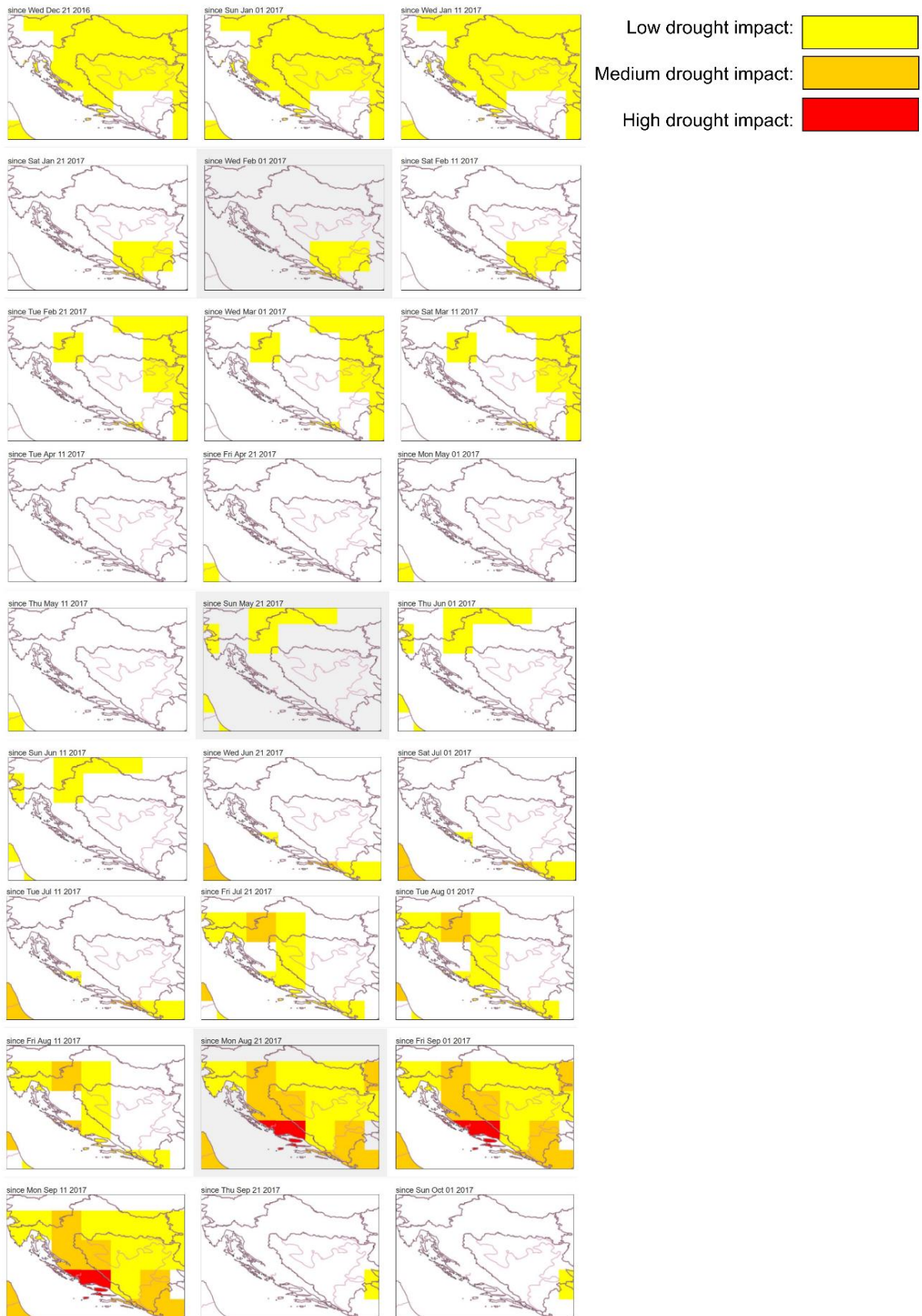


Figure 47: GDO 10-day period maps of risk of drought impact for agriculture in Croatia in 2017 (Drought Impact Report, n.d)

<b>Soil Types:</b>	<b>Definition:</b>
<b>Acrisols</b>	Strongly leached, red and yellow soils of wet (sub-)tropical regions on acid parent rock, with a clay accumulation horizon, low cation exchange capacity and low base saturation
<b>AlbeLuvisols</b>	Base-poor soils of humid temperate regions with a bleached eluviation horizon tonguing into a clay-enriched subsurface horizon.
<b>Alisols</b>	Soils of wet (sub-)tropical regions with high cation exchange capacity and much exchangeable aluminum.
<b>Andosols</b>	Soil developed from volcanic material, are young immature soils, characteristics depend on type of volcanic material.
<b>Calcisols</b>	Soils of (semi-)arid regions with enrichment of secondary carbonates.
<b>Cambisols</b>	Soils that show "signs of beginning soil formation", i.e. that are only moderately developed on account of their limited pedogenetic age or because of rejuvenation of the soil material. Moderately developed soils occur in all environments, from sea level to the highlands, from the equator to the boreal regions, and under all kinds of vegetation.
<b>Chernozems</b>	Soils with deep, very dark surface soils and carbonate enrichment in the subsoil that occur in the steppe zone between the dry climates and the humid Temperate Zone. This transition zone has a climax vegetation of ephemeral grasses and dry forest.
<b>Cryosols</b>	Soils of permafrost regions. These soils show signs of 'cryoturbation' (i.e. disturbance by freeze-thaw sequences and ice segregation) such as irregular or broken soil horizons and organic matter in the subsurface soil, often concentrated along the top of the permafrost table.
<b>Durisols</b>	Soils of (semi-)arid regions with a layer or nodules of soil material that is cemented by silica.
<b>Ferralsols</b>	Soils of wet (sub-)tropical regions that have a very low cation exchange capacity and are virtually devoid of weatherable minerals.
<b>Fluvisols</b>	Young alluvial soils mainly found along rivers or other low terrain positions, which show stratification or other evidence of recent sedimentation.
<b>Gleysols</b>	Non-stratified soils in waterlogged areas that do not receive regular additions of sediment. Usually found in low terrain positions
<b>Histosols</b>	Soils consisting primarily of organic materials. They are defined as having 40 centimeters or more of organic soil material in the upper 80 centimeters.
<b>Kastanozems</b>	Soils occurring in the driest parts of the steppe zone. Compared to Kastanozmes they are less deep, brownish surface soils and have carbonate and/or gypsum accumulation at some depth.

<b>Leptosols</b>	Shallow soils in elevated and/or eroding areas over hard rock or highly calcareous material.
<b>Lixisols</b>	Soils of wet (sub-)tropical regions with a low cation exchange capacity but high base saturation percentage.
<b>Luvisols</b>	Brownish and greyish, base-rich soils of humid temperate regions with a distinct clay accumulation horizon.
<b>Nitisols</b>	Deep soils of wet (sub-)tropical regions in relatively rich parent material and marked by shiny, nutty structure elements.
<b>Phaeozems</b>	Dusky red soils of prairie regions with high base saturation but no visible signs of secondary carbonate accumulation.
<b>Planosols</b>	Brownish and greyish soils of humid temperate regions with a bleached topsoil over dense, slowly permeable subsoil.
<b>Plinthosols</b>	Soils of wet (sub-)tropical regions on old weathering surfaces; these soils are marked by the presence of a mixture of clay and quartz ('plinthite') that hardens irreversibly upon exposure to the open air.
<b>Podzols</b>	Soils of humid temperate regions with a bleached eluviation horizon over an accumulation horizon of organic matter with aluminum and/or iron.
<b>Regosols</b>	Relatively deep soils that occur in unconsolidated materials and which have only surficial profile development, e.g. because of low soil temperatures, prolonged dryness or erosion.
<b>Solonchaks</b>	Soils of (semi-)arid regions with a high content of soluble salts.
<b>Solonetz</b>	Soils of (semi-)arid regions with a high percentage of adsorbed sodium (Na+) ions.
<b>Stagnosols</b>	Soils with strong mottling of the soil profile due to redox processes caused by stagnating surface water.
<b>Umbrisols</b>	Soils of humid temperate regions with a thick, dark, acid surface horizon that is rich in organic matter
<b>Vertisols</b>	Swelling and shrinking heavy clayey soils of backswamps, river basins, lake bottoms, and other areas with a high content of expanding 2:1 lattice clays.

Table 6: Short definitions of TAXNWRB Soil Grids Dataset Soil Types

### Total Epoch

Aoi	Mean	Standard Deviation	Min. Value	Max. Value	Range
North	0.079	0.067	-0.178	0.270	0.448
South	-0.043	0.149	-0.415	0.420	0.835
Croatia	0.032	0.118	-0.423	0.420	0.843

### Short Epoch

Aoi	Mean	Standard Deviation	Min. Value	Max. Value	Range
North	0.086	0.096	-0.324	0.421	0.745
South	-0.064	0.154	-0.448	0.380	0.828
Croatia	-0.005	0.144	-0.448	0.445	0.893

Table 7: Correlation coefficient statistics of area of interests 'north' and 'south' as well as entire Croatia.

	Point 1		Point 2		Point 3		Point 4		Point 5	
	Year	Annual Rainfall [mm]	Year	Annual Rainfall [mm]	Year	Annual Rainfall [mm]	Year	Annual Rainfall [mm]	Year	Annual Rainfall [mm]
Sorted from lowest to highest annual rainfall	2003	296,83	2016	229,38	2011	208,57	2011	263,24	2011	231,86
	2001	357,27	2017	246,37	2003	215,68	2003	289,53	2012	279,27
	2011	370,05	2011	270,94	2000	240,77	2012	333,69	2003	321,08
	2006	380,37	2003	278,71	2012	286,19	2006	335,05	2000	332,27
	2007	405,38	2015	334,28	2015	288,96	2000	355,15	2013	354,53
	2000	415,47	2006	338,01	2001	307,73	2016	361,92	2015	359,54
	2002	419,87	2001	347,18	2002	312,28	2007	363,11	2007	372,54
	2015	428,41	2012	348,06	2006	318,38	2017	370,49	2006	374,98
	2004	434,33	2013	355,27	2008	319,74	2008	379,65	2008	382,44
	2012	441,24	2000	364,87	2009	327,31	2015	381,10	2001	407,09
	2008	469,05	2008	377,50	2005	338,83	2001	381,37	2005	440,61
	2005	474,46	2009	386,69	2007	353,43	2002	418,21	2009	441,33
	2009	491,15	2007	386,78	2013	353,80	2013	422,70	2009	452,07
	2013	531,20	2005	409,29	2004	355,51	2009	423,28	2002	453,03
	2009	562,88	2009	415,40	2009	393,15	2005	429,80	2004	481,02
	2014	630,93	2002	422,08	2017	419,67	2004	461,47	2014	536,90
	2016	753,28	2004	434,02	2014	438,57	2009	468,57	2017	660,52
	2017	805,97	2014	491,31	2016	446,25	2014	530,88	2016	764,22
	<b>Average Annual Rainfall [mm]:</b>	<b>462,48</b>	<b>349,70</b>	<b>322,27</b>	<b>378,72</b>	<b>404,77</b>				

Average Annual Rainfall over all 5 points of interest [mm]	
2015	358,46
2016	511,01
2017	500,61

Table 8: Annual Rainfall for points of interest defined in Figure 18 calculated from GLDAS 'Rainf\_tavg' data

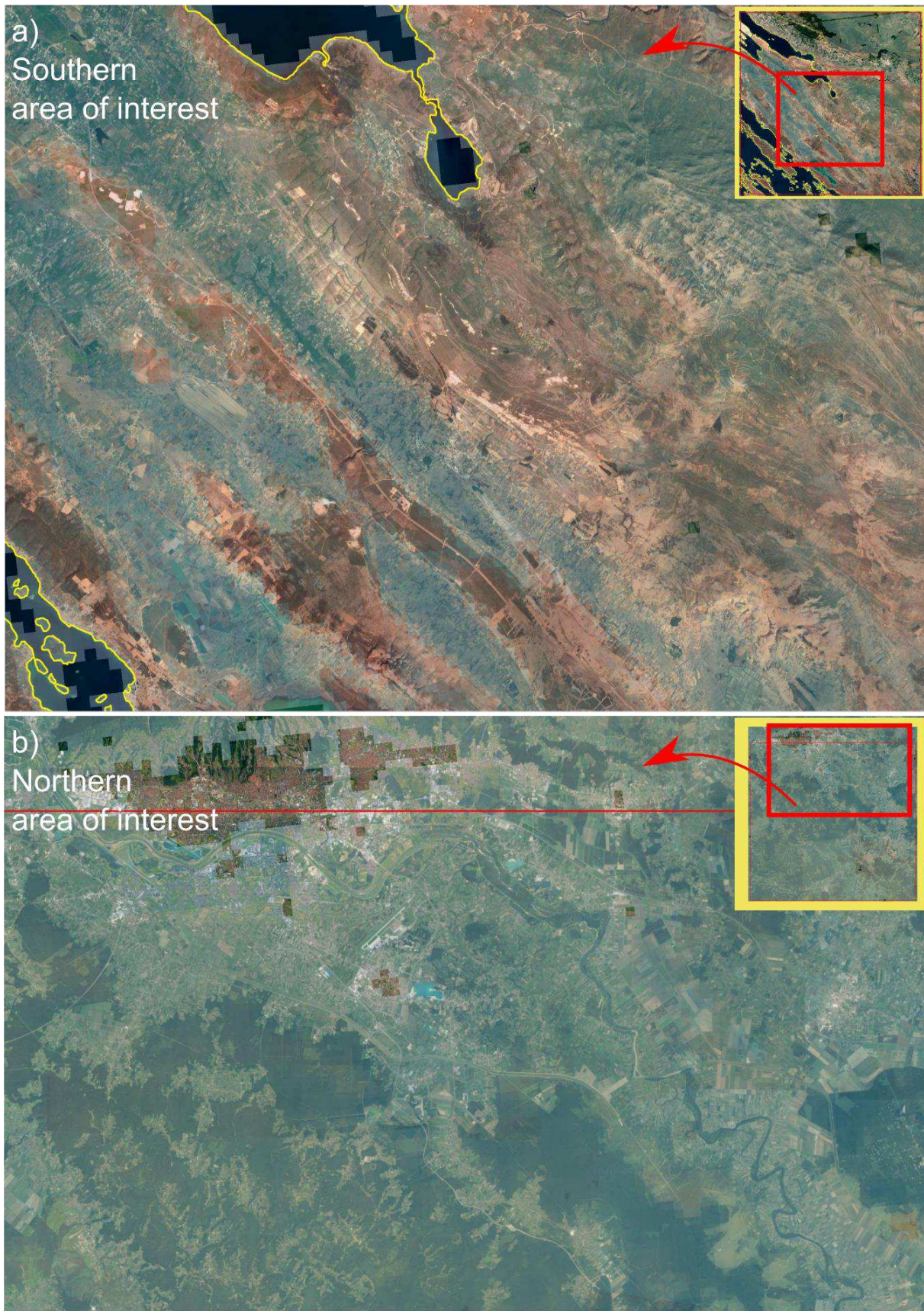
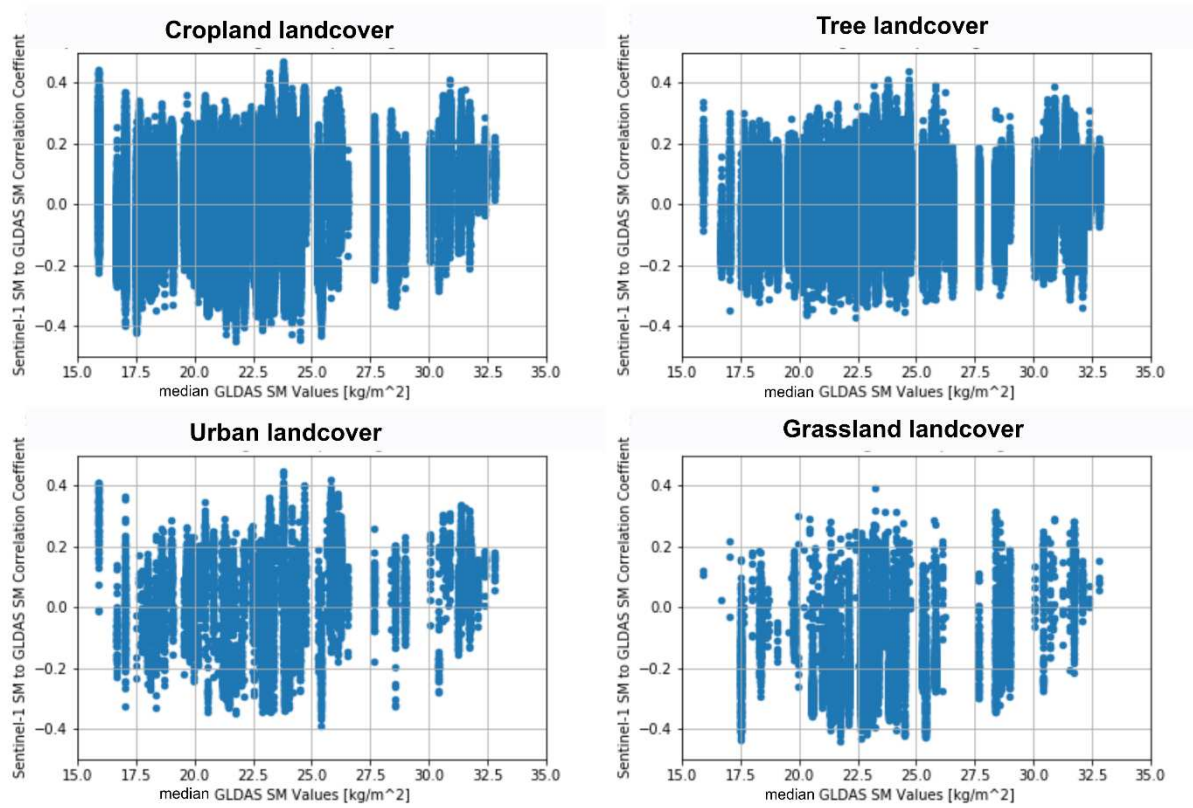


Figure 48: Spatial distribution of correlation coefficients between S-1 and GLDAS SM data for the 'total' epoch superimposed with Google satellite imagery.

**Short epoch: Scatter plot of the correlation coefficients between Sentinel-1 SM and GLDAS SM of ESA CCI landcover types against median GLDAS SM values**



**Total epoch: Scatter plot of the correlation coefficients between Sentinel-1 SM and GLDAS SM of ESA CCI landcover types against median GLDAS SM values**

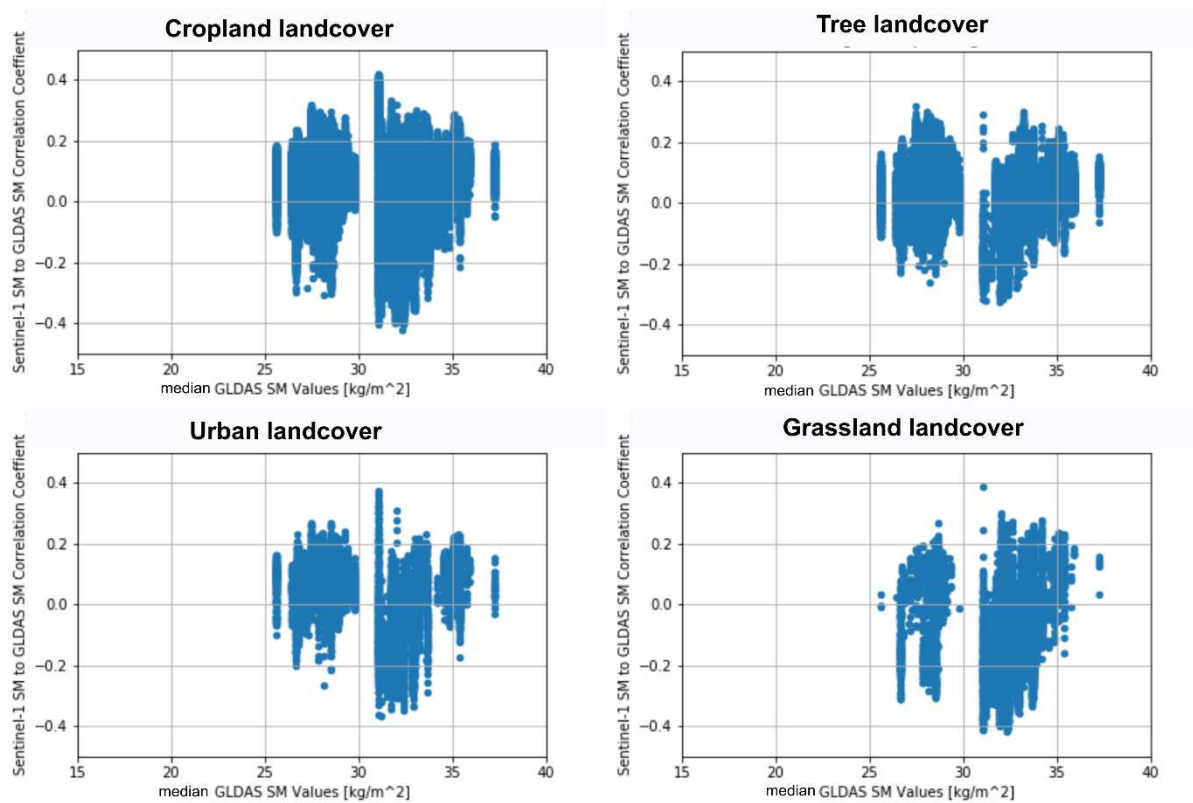
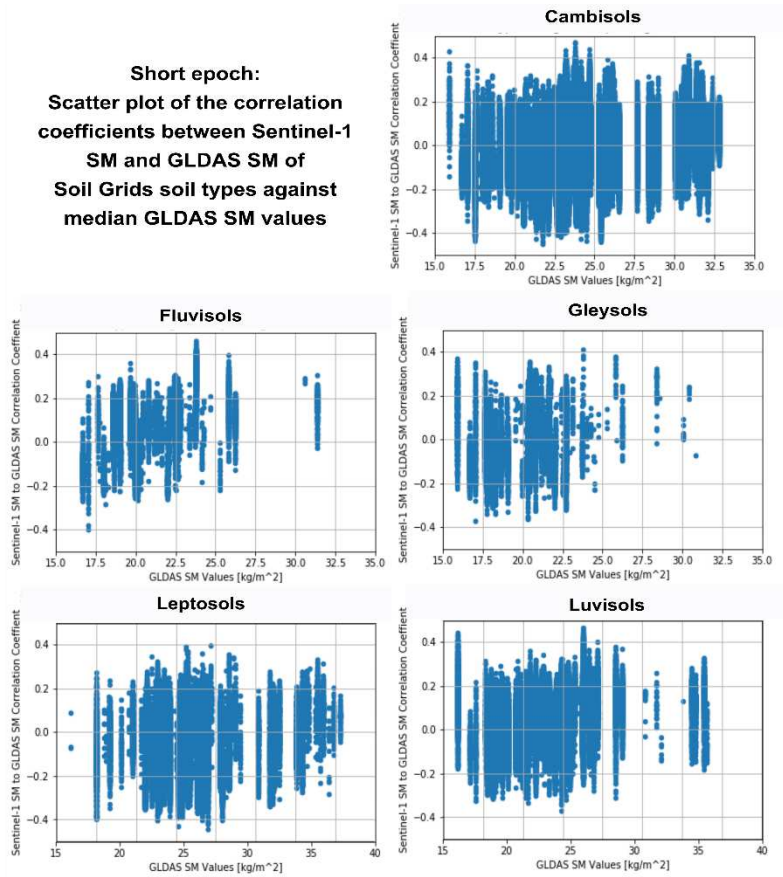


Figure 49: Scatter plots of the correlation coefficients between S-1 SM and GLDAS SM of the ESA CCI landcover types against the median GLDAS SM values of the 'short' and 'total' epoch respectively

**Short epoch:  
Scatter plot of the correlation  
coefficients between Sentinel-1  
SM and GLDAS SM of  
Soil Grids soil types against  
median GLDAS SM values**



**Total epoch:  
Scatter plot of the correlation  
coefficients between Sentinel-1  
SM and GLDAS SM of  
Soil Grids soil types against  
median GLDAS SM values**

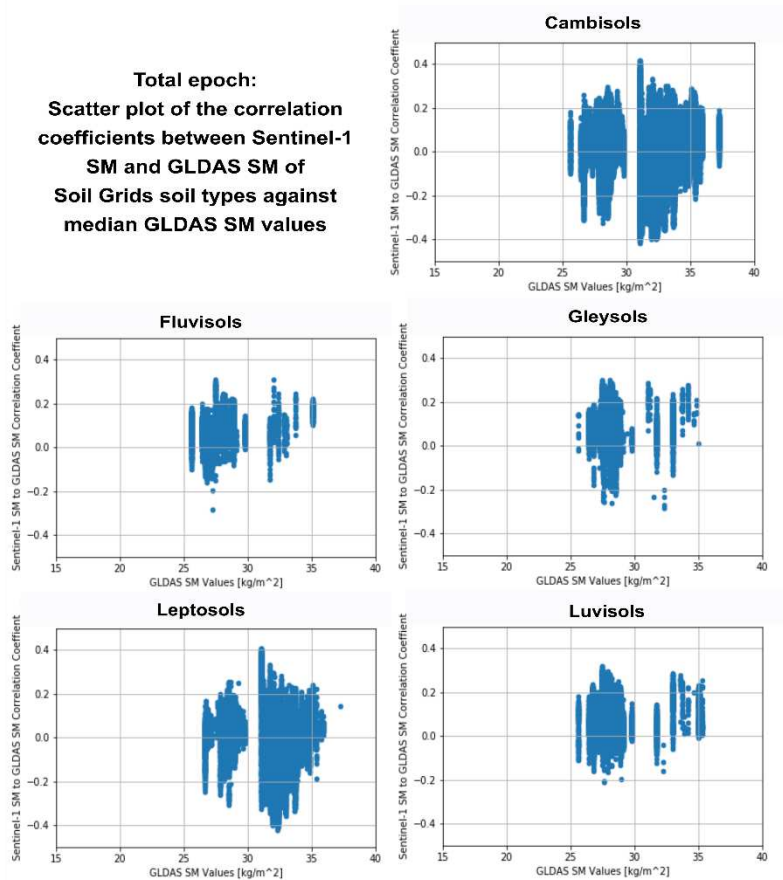
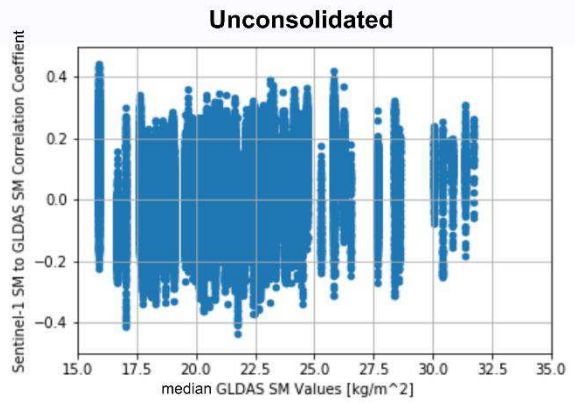
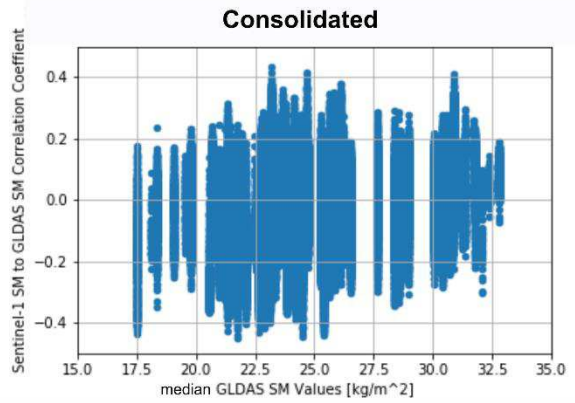
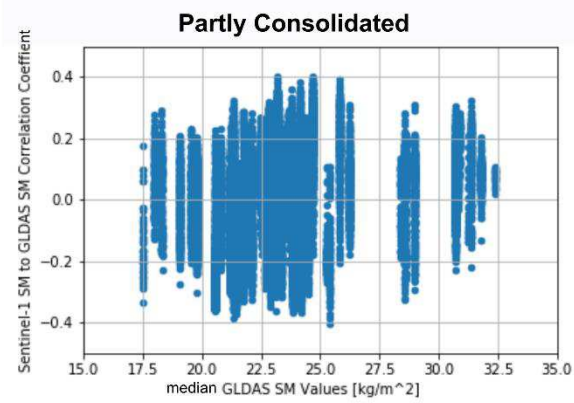


Figure 50: Scatter plots of the correlation coefficients between S-1 SM and GLDAS SM of the SoilGrids soil types against the median GLDAS SM values of the 'short' and 'total' epoch respectively



**Short epoch:**  
Scatter plot of the correlation coefficients  
between Sentinel-1 SM and GLDAS SM  
of lithology types against median GLDAS  
SM values



**Total epoch:**  
Scatter plot of the correlation coefficients  
between Sentinel-1 SM and GLDAS SM  
of lithology types against median GLDAS  
SM values

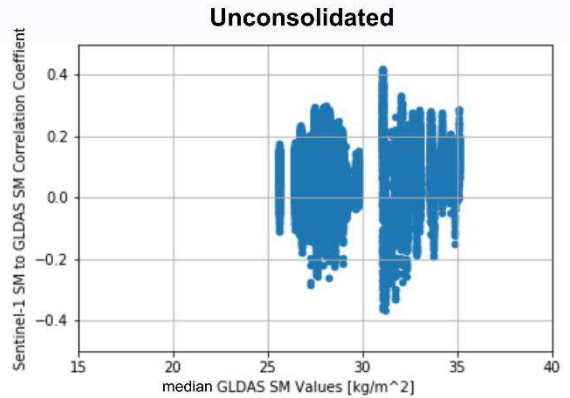
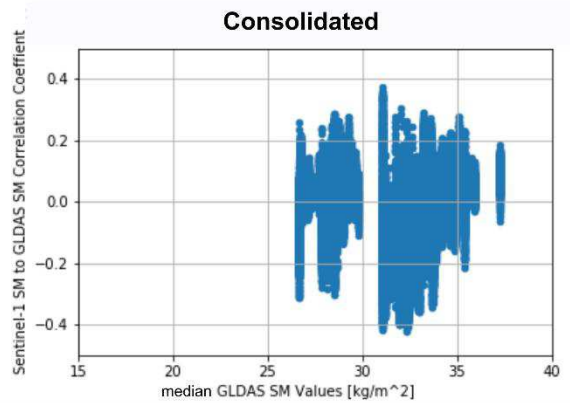
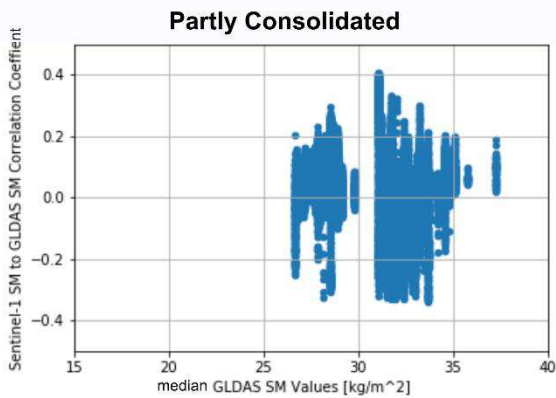


Figure 51: Scatter plots of the correlation coefficients between S-1 SM and GLDAS SM of the lithology types against the median GLDAS SM values of the 'short' and 'total' epoch respectively

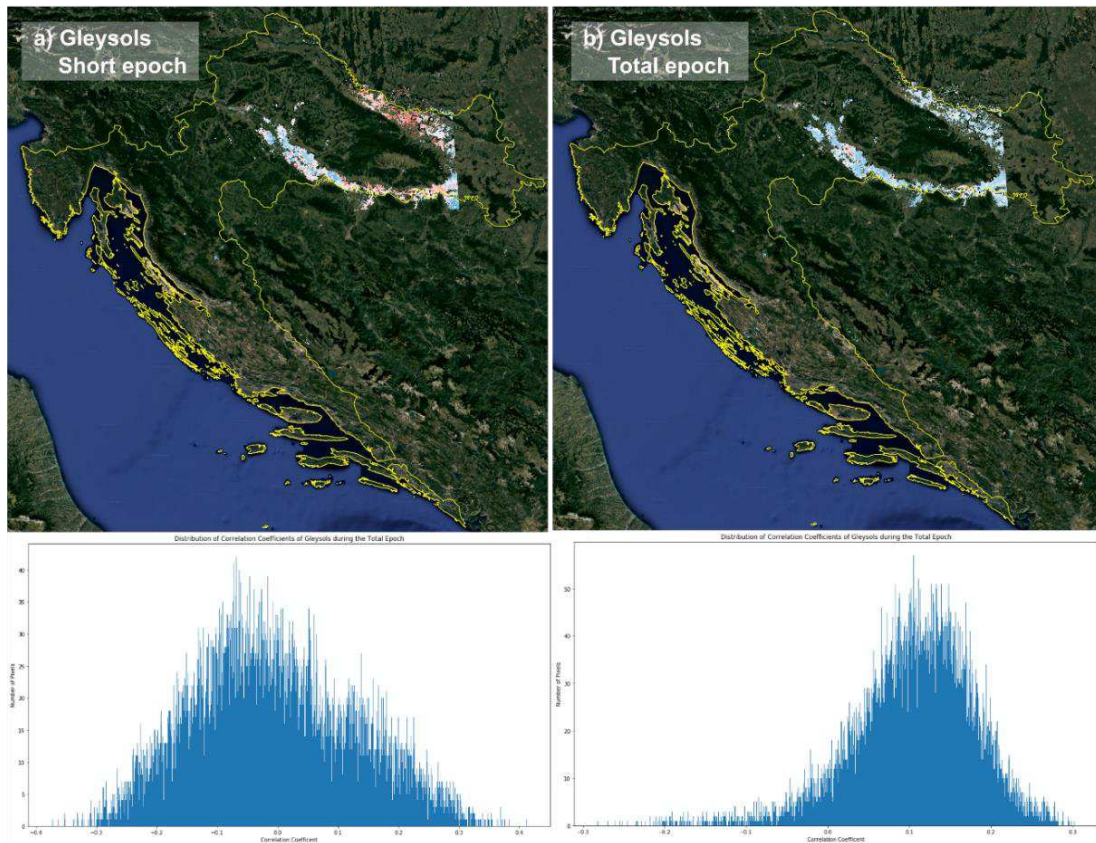


Figure 52: Spearman's rank correlation coefficient for the Gleysols TAXNWRB soil type class during the (a) short and (b) total epoch. Histogram of coefficient distribution and basic statistics of the dataset.

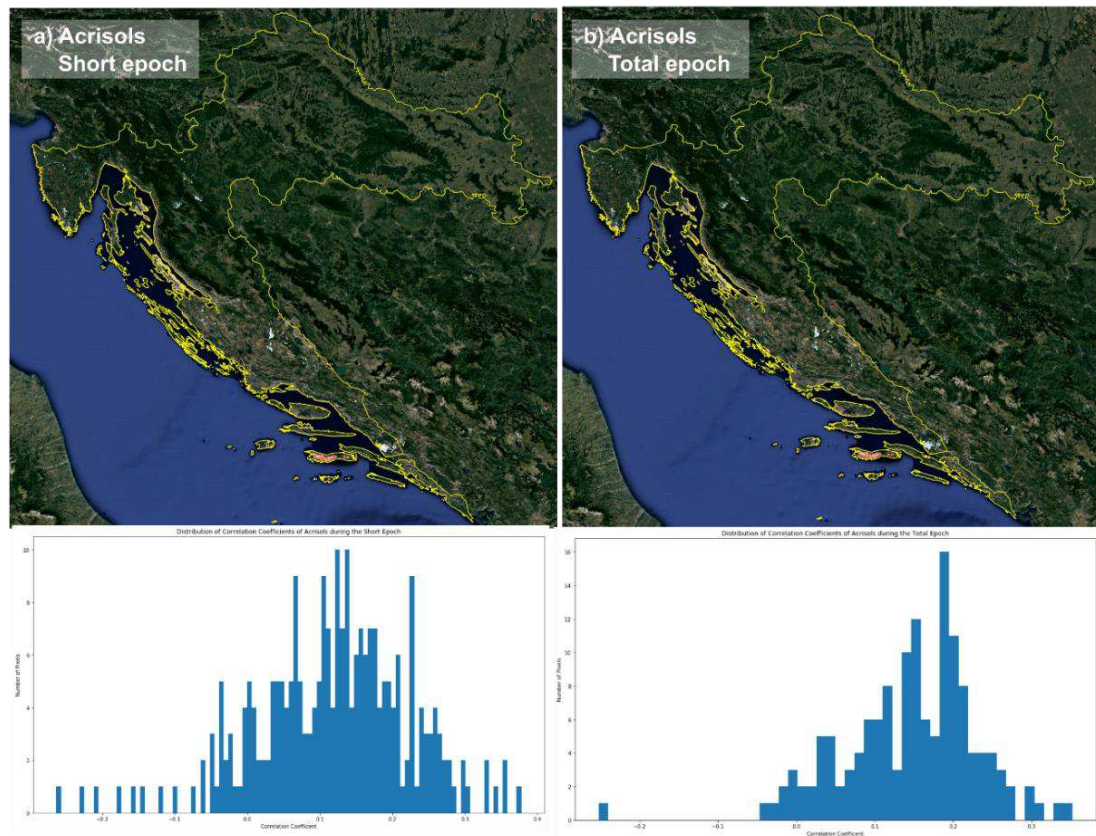


Figure 53: Spearman's rank correlation coefficient for the Acrisols TAXNWRB soil type class during the (a) short and (b) total epoch. Histogram of coefficient distribution and basic statistics of the dataset.

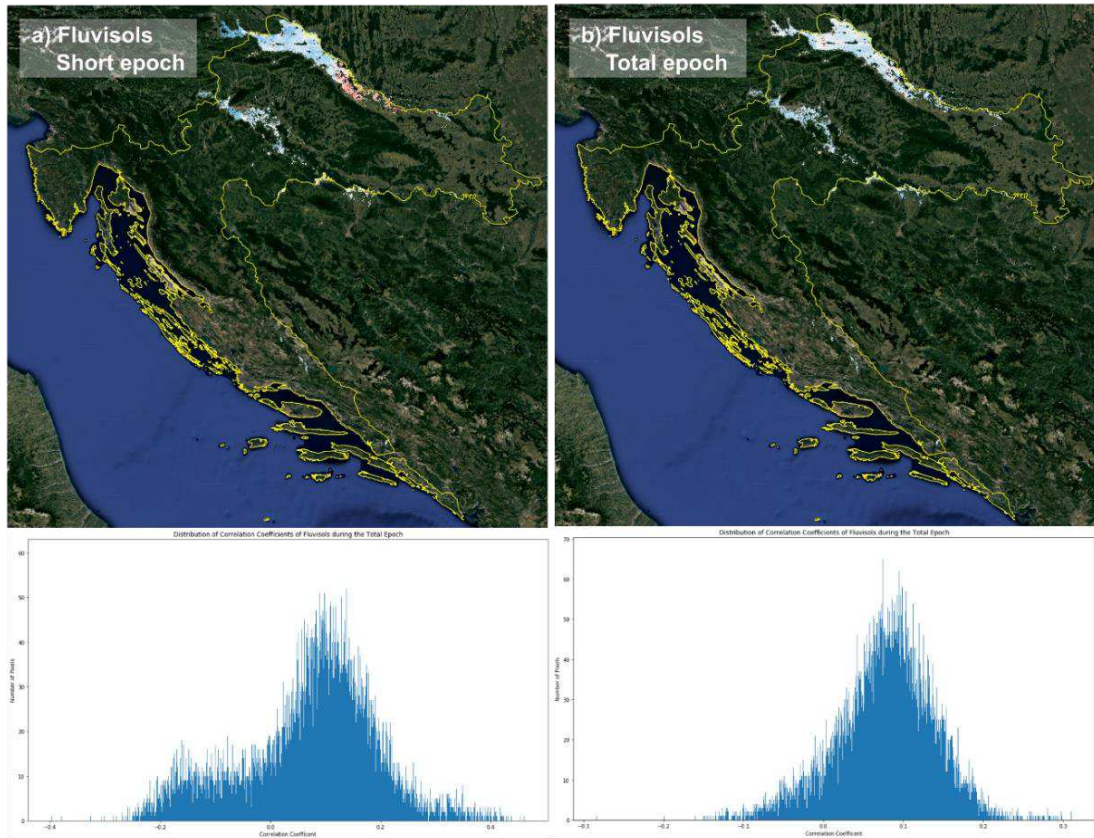


Figure 54: Spearman's rank correlation coefficient for the Fluvisols TAXNWRB soil type class during the (a) short and (b) total epoch. Histogram of coefficient distribution and basic statistics of the dataset.

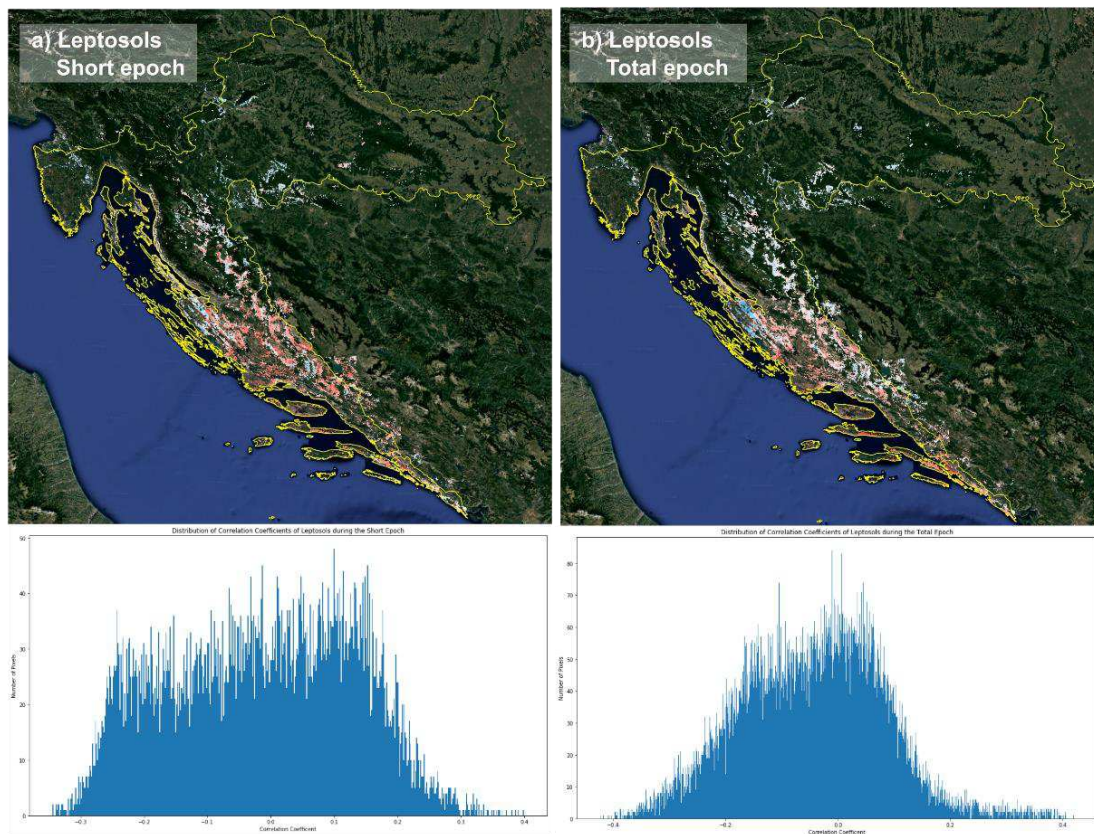


Figure 55: Spearman's rank correlation coefficient for the Leptosols TAXNWRB soil type class during the (a) short and (b) total epoch. Histogram of coefficient distribution.